Title
Development of Novel Energy-based Musculoskeletal Therapies

Permalink
https://escholarship.org/uc/item/4h99g8x9

Author
Horne, Devante Aaron

Publication Date
2020

Peer reviewed|Thesis/dissertation

Development of Novel Energy-based Musculoskeletal Therapies

by

Devante Horne

DISSERTATION
Submitted in partial satisfaction of the requirements for degree of
DOCTOR OF PHILOSOPHY

in

Bioengineering

in the

GRADUATE DIVISION

of the

UNIVERSITY OF CALIFORNIA, SAN FRANCISCO
AND
UNIVERSITY OF CALIFORNIA, BERKELEY

Approved:

_____   Jeffrey Lotz
Jeffrey Lotz
3D96864A89B54C2...   Chair

_____   Grace O'Connell
Grace O'Connell
DocuSigned by: 4FF...

_____   Lionel Metz
Lionel Metz
DocuSigned by: 439...

_____   Diederich, Chris
Diederich, Chris
07F6E887F166488...

_____
                                                    Committee Members

Acknowledgements

This dissertation was made possible by my incredible support network of mentors, lab mates, friends, and family who have contributed to my graduate school and life experience. A sincere thank you to Dr. Jeff Lotz, who is truly a great PhD advisor. I was drawn to the Lotz Lab by the lure of the opportunity to grow my skills as both an engineer and scientist. Over the past few years, Dr. Lotz has provided invaluable advice, ideas, and opportunities for me to connect with academic and industry leaders. Thank you for creating a welcoming lab environment and providing me the encouragement and guidance necessary for success. Your supportive, but hands-off mentorship style is what has shaped me into the confident and independent researcher that I am today and has enabled an incredibly well-rounded graduate education. I am so grateful for your guidance in my development both scientifically and professionally as I continue on to the next stage of my career.

Thank you to the professors on my qualifying exam and dissertation committees: Dr. Grace O'Connell, Dr. Lionel Metz, Dr. Tamara Alliston, Dr. Chris Diederich, and Dr. Kyriakos Komvopoulos. I thank each of you for providing your expertise and feedback toward the development of my dissertation research. I want to give a special thanks to Dr. Diederich, my close collaborator and mentor. I am grateful to have had the opportunity to work in your lab and further develop my hands-on engineering skills. Thank you for your consistent interest in my work and for being willing to come into the lab and get your hands dirty.

Many thanks my co-authors and teammates: Peter Jones, Dr. Matt Adams, and Dr. Mohamed Habib. It has been an honor working with each of you on the LIPUS and PEMF projects. Thank you, Peter and Matt, for sharing all of your valuable hands-on ultrasound and engineering knowledge in the Thermal Therapy Lab. A very special thank you to my good friend, Mohamed.

I have truly enjoyed working next to you over the past couple of years. You are one of the most humble people I know, and I aspire to be more like you.

Thank you to the Orthopaedic Surgery Research Group members, past and present, for creating a research environment that was welcoming, collaborative, and fun. Ellen, I will miss our Monday morning conversations as well as all of your valuable insights on histology. Jeannie, thank you for always keeping the lab interesting. Zuzka, you have been such a great friend and research buddy over the last couple of years. Thank you for your willingness to chat about the challenges of my research – you are an outstanding scientist, and I really appreciated all of your insights. And I would be remiss if I did not give a proper shout out to Lola - may your cells live on forever.

I am thankful for the NSF Graduate Research Fellowship and the UC Berkeley Chancellors Fellowship for their funding which allowed me to focus on research and gave me the opportunity and freedom to follow my own research interests.

I moved across the country to start this PhD journey without knowing anyone, but I leave this stage of my live having gained such an incredible community in the Bay Area. I want to thank everyone in the UC Berkeley – UCSF Bioengineering Program who I have worked with and became friends with over the past 5 years. Thank you to all of my friends outside of the program who have kept me sane and shared so many good memories. Completing a PhD can be very isolating, and it was especially challenging as the only graduate student in my lab. Yet, I succeeded with the support of a lot of people on the outside looking in, and I am so grateful for each of you. Arthur, Evan, Justin, Quincy, Greg, Jermaine, and Tony; you all have been my guys since day 1! You all have seen me through this entire journey, and it would not have been the same without you. Thank God for my Reality SF Community Group – thank you for your endless encouragement and for keeping me grounded in this city.

Contributions

The following chapters in this dissertation consist of work that has been published or submitted for publication in a peer-reviewed journal and may deviate from the final published versions.

Chapter 2 is adapted from "Low Intensity Pulsed Ultrasound (LIPUS) for the treatment of intervertebral disc degeneration," a research article published in the *Proceedings of SPIE* in 2017 and authored by Devante Horne, Peter Jones, Vasant Salgaonkar, Matthew Adams, B. Arda Ozilgen, Peter Zahos, Xinyan Tang, Ellen Liebenburg, Dezba Coughlin, Jeffrey Lotz, and Chris Diederich.

Chapter 3 is adapted from "LIPUS far-field exposimetry system for uniform stimulation of tissues in-vitro: development and validation with bovine intervertebral disc cells," a research article published in *Biomedical Physics and Engineering Express* in 2020 and authored by Devante Horne, Peter Jones, Matthew Adams, Jeffrey Lotz, and Chris Diederich.

Chapter 5 is adapted from "Magnetic nanoparticles synergize with pulsed magnetic fields to stimulate osteogenesis in-vitro," a research article submitted for publication and authored by Mohamed Habib*, Devante Horne*, Khalid Hussein, Dezba Coughlin, Erik I Waldorff, Nianli Zhang, James Ryaby, Jeffrey Lotz (*Equal Contribution).

Abstract

Development of Novel Energy-based Musculoskeletal Therapies

by

Devante Aaron Horne

Back pain is the most common musculoskeletal condition, affecting 80% of Americans at some point in their lifetimes. Intervertebral disc (IVD) pathologies, such as annular tears and herniated discs, are the most common source of low back pain and account for more than 40% of cases. Current treatment options, including discectomy and intradiscal injections, involve invasive procedures and are limited to short-term symptom relief without repairing damaged IVDs. This dissertation explores the stimulatory effects and dose-response relationships of low-intensity pulsed ultrasound (LIPUS) and pulsed electromagnetic fields (PEMF), with the goal of advancing the development of these energy-based therapies for the noninvasive treatment of low back pain. Towards this goal, this dissertation is broken into 4 studies. In the first study, we demonstrate the technical feasibility of targeted, noninvasive delivery of acoustic energy to rat-tail IVDs and evaluate gene expression changes in injured IVDs in response to LIPUS exposure. We found that LIPUS exposure regulates extracellular matrix and inflammatory gene expression in rats with increased pro-inflammatory gene expression. In the second study, we design, fabricate, characterize, and validate an *in-vitro* LIPUS exposimetry system for delivering uniform acoustic energy to cells while removing potentially confounding factors including beam reflections and sample heating. We demonstrate that far-field LIPUS exposure upregulates collagen synthesis in annulus fibrosus cells and is equivalent to growth factor treatment. In the third study, we present the use and validation of design of experiments (DOE) for LIPUS parameter exploration, response

prediction, and optimization. We discovered that pulse repetition frequency is the most significant factor for modulating catabolic and pro-inflammatory gene expression while peak intensity is most significant for modulating anabolic gene expression, and that both factors interact with treatment duration to influence extracellular matrix gene expression in inflammatory annulus fibrosus cells. In the last study, we show that magnetic nano-bone substitutes (MNBS) synergize with PEMF to stimulate *in-vitro* osteogenesis. We found that the combination of PEMF and MNBS accelerates osteogenesis by stimulating early alkaline phosphatase activity and increasing mineralization over time in mesenchymal stem cells. Collectively, the work presented in this dissertation represents significant contributions to the development of two novel energy-based therapies for painful spine conditions. These findings will motivate the use of noninvasive, biologically active treatments for repairing damaged IVDs and alleviating low back pain.

Table of Contents

List of Figures

List of Tables

1 Introduction

1.1 Clinical Motivations

Low back pain (LBP) is one of the most significant non-lethal medical ailments in society, affecting 80% of the population at some point in their lifetime [1]. Intervertebral disc (IVD) pathologies, including tears in the annulus fibrosus and disc herniation, are the most common source of LBP, accounting for more than 40% of cases [2]. Current LBP treatments begin conservatively with pain management through physical therapy and medication and may advance to invasive interventions including surgical removal of the disc and segmental fusion [3]. For less severe herniation cases, the standard treatment is discectomy, or surgical removal of the protruding herniation tissue. Discectomy is an effective therapy for pain relief in patients suffering from sciatica due nerve impingement. However, removing a portion of the protruding nucleus pulposus leaves behind a hole in the annulus which likely contributes to the high re-herniation rates (up to 21%) and persisting post-operative LBP [4, 5]. Oftentimes, surgeons opt to leave the annular defect to heal on its own; however, the IVD has limited healing capacity related to it being sparsely cellularized and having a poor blood supply. Restoration of the damaged annulus fibrosus tissue may prevent further progression of disc herniation; however, there is no effective treatment to repair annulus fibrosus damage that effectively promotes tissue regeneration and restores IVD biomechanics [6]. There is a clinical need for a more effective and noninvasive treatment for annulus fibrosus repair. In particular, mechanical stimulation of IVD cells is a potential therapeutic modality that could be used to stimulate local extracellular matrix synthesis at the injury site. It is well known that IVD cells and tissue respond to mechanical stimulation by increasing proteoglycan and collagen synthesis [7-9]. However, a restorative disc therapy would rely on some remaining viable disc tissue, and therefore may not be effective in cases of severe IVD

degeneration which may ultimately require spinal fusion. The goal of spinal fusion is to stimulate the vertebrae to fuse into a rigid, immovable column of bone; however, in some cases the bones do not properly fuse, allowing for continued joint motion and causing pain, and require a second surgery. Due to high pseudarthrosis rates, there is an increased interest in the development of adjuvant therapies to improve the successful fusion rates. Various techniques, including bone grafts loaded with osteoinductive proteins or stem cells, have shown some success in increasing fusion rates, but with limited efficacy and low efficiency.

The primary focus of this research is the investigation of the targeting ability and dose-response metrics for low-intensity pulsed ultrasound for stimulating annulus fibrosus repair. In addition, we evaluate the synergistic effects of pulsed electromagnetic fields and magnetic nanoparticles for stimulating spinal fusion.

1.2 Intervertebral Disc Structure and Function Overview

The IVD is an articulating, load-bearing structure between the vertebral bodies of the spine. In the center of the disc is the nucleus pulposus (NP); this soft, proteoglycan rich tissue imbibes water and provides compressive resistance. The NP is surrounded the stiffer annulus fibrosus (AF), composed of lamellae of collagen fibers which accounts for its tensile strength. Between the IVD and each vertebral body are the cartilage endplates which serve as barriers for nutrient and waste exchange between the IVD and vertebrae. While the etiology of LBP is not fully understood, IVD-related pathologies account for a significant portion of LBP cases [2, 3, 5].

1.2.1 Tissue Structure and Biomechanics

The intervertebral disc is a ligamentous tissue, connecting adjacent vertebral bodies, and serves to support and dissipate both tensile and compressive loads while concurrently providing

flexibility by allowing multiaxial spinal motion. The structure of the three primary regions of the IVD are closely related to their biomechanical function.

In the center of the IVD is the NP, a gel-like structure with an extracellular matrix similar to cartilage, containing mostly proteoglycans in addition to randomly organized collagens, and radially oriented elastin fibers [10]. The extracellular matrix (ECM) of the NP is rich in proteoglycans containing many sulfated glycosaminoglycan chains that are negatively charged, causing the NP to imbibe water and create a swelling pressure in the disc and allowing the disc to maintain its height and resist compressive loads. The water content of healthy discs is high (80 – 88%), helping to resist compression during physiological loading which ranges from 0.4 – 2.3 MPa [11, 12].

Surrounding the NP is the AF, a lamellar structure comprised of layers of collagen fibers acting as a vessel wall supporting the radial swelling pressure of the NP. The AF consists of 15 - 25 concentric lamellae in which collagen fibers are arranged at alternating angles of $\pm\ 35°$ from the end plate [13], allowing the disc to withstand tensile loads during bending and twisting of the spine. In addition, the inter-lamellae space consists of water-binding proteoglycan aggregates that interact with the collagen fibers and aid the AF in resisting circumferential tension when the NP expands under axial compressive loading [14]. Regions of the AF differ based on structural and cellular variation. The outer layers are composed mostly of highly organized type I collagen fibers, making it more fibrous and resistant to tensile loads. In contrast, the inner AF (or transition zone) is composed mostly of type II collagen and proteoglycans, making it more fibrocartilaginous and resistant to high hydrostatic pressure from the NP.

Between the IVD and each vertebral body is a thin cartilage end plate (CEP) which serve as a barrier through which nutrients and waste are diffused between the vertebral body and the

disc. In addition, the CEP, which boarders the NP and the inner AF, serves to constrain the pressurized NP superiorly and inferiorly as well as to distribute the hydrostatic pressure from the NP into the vertebrae. While the CEP is avascular, its permeability is thought to impact disc cell health as diminished permeability can decrease transport between the NP and vertebral capillaries [15, 16].

1.2.2 Cellular Structure and Function

The ECM network of the IVD, which provides its mechanical characteristics, is synthesized and maintained by a sparse population of cells. The specialized cell types within the disc contribute to the structure and function of the tissue. This dissertation primarily focuses on AF cells.

The AF cell phenotype is fibroblast-like, highlighting the morphology and propensity to synthesize type I collagen. AF cells assume a flattened, spindle-shaped (elongated) morphology, aligning with collagen fibers [17] forming the AF lamellar structure. The AF-cell morphology and phenotype correlates with the structural gradient present in the AF tissue from outer AF to inner AF. The average AF-cell density in human discs is 9×10^6 cells/cm^3, with lowest density near the NP and increasing density towards the outer annulus [18, 19]. Compared to cells of the inner AF, outer-AF cells are more elongated with interconnected processes [20], tend to align more with the lamellae [19], and are more fibroblastic while inner AF cells are more chondrocyte-like [20]. AF cells can be distinguished from NP cells by their higher collagen I: collagen II ratio, higher collagen I: proteoglycan ratio, and expression of collagen V [18].

The NP cell phenotype is chondrocyte-like, assuming a more spherical shape and greater expression of aggrecan than type II collagen. The average NP-cell density in humans is less than half that of the AF at 4×10^6 cells/cm^3 [21].

CEP cells are similar to articular chondrocytes both in their rounded morphologically as well in expression profile for proteoglycans, type II collagen, and type I collagen. The CEP is also sparsely cellular, with an average density of 15 x 10^3 cells/cm^3 [22].

1.2.3   Molecular Structure and Function

The IVD extracellular matrix is a highly specialized framework of macromolecules that attract and contain water. The major macromolecules of the IVD are type I collagen, type II collagen, and proteoglycan [23], and the ratios of their expression vary among the NP, AF, and CEP tissues [24]. The fibular collagens align to form the lamellae in the AF and provide tensile strength while the proteoglycans accumulate primarily in the NP creating a net negative charge that attracts water and provides resistance to compressive loads [25].

Regulation of the healthy IVD involves a balance of the synthesis and degradation of these matrix molecules is vital for the integrity of the IVD [23]. Moreover, repair of damaged IVD is a highly regulated process controlled by a variety of molecules including growth factors, cytokines, and matrix metalloproteinases (MMPs). Among various metabolic enzymes present in the IVD, matrix metalloproteinase -1 (MMP1) and matrix metalloproteinase -13 (MMP13) are the primary enzymes that are capable of cleaving interstitial collagen molecules. Insufficient regulation of these enzymes may lead to excess matrix degradation, offsetting the normal balance and leading to pathological conditions including the initiation and progression of IVD degeneration.

1.3   Intervertebral Disc Damage and Degeneration

Degeneration of the IVD is a cascade of events related to changes in disc cells, the ECM regulation, and the biomechanics of the disc. Each of these degenerative changes are related, creating a degenerative cycle [26]. Disc degeneration begins in early adulthood and has been observed as early as the second decade of life [27]. As degeneration progresses with age, metabolic

balance is disrupted, proteoglycan concentration decreases, and with that, disc height is reduced due to dehydration. Loss in disc height further exacerbates biomechanical changes related to the abnormal loading and depressurization of the NP and increased strain on collagen fibers of the AF, leading to AF tears and fissures and ultimately protrusion (i.e. herniation) of the NP [28]. Age-related degeneration may be accelerated by traumatic failure of the AF due to acute injury caused by overloading, provoking herniation. Additionally, damage and over-mineralization of the CEP is thought to reduce permeability and disrupt nutrient exchange leading to cell death [15]. Moreover, disruptions to the CEP affect loading distributions, further amplifying the magnitude of stress concentrations and local instability [29]. Age-related changes within the disc structure including decreased availability of nutrients, cell senescence, matrix disorganization, accumulation of pro-inflammatory cytokines, and increased catabolism are thought to contribute to complex etiology of pathologic degeneration.

Disc degeneration can be diagnosed via noninvasive imaging methods, with magnetic resonance (MR) imaging being the current gold standard diagnostic method. T1 and T2 weighted MR imaging can clearly show pathological features including disc bulges, herniation, and nerve impingement [30]. In addition, sequences such as T1-ρ [31] have been used to detect advanced degeneration properties including dehydration, decreased disc height, altered fat content, annular defects, Modic changes, and changes in the CEP [32]. Discography is standard diagnostic method for identifying discogenic pain and involves injecting contrast agent into the disc during radiographic imaging. Discography is a controversial technique due to concerns about the sensitivity and subjectivity of the test as well as the possibility of increased degeneration risk due to mechanical disruption of the AF with needle puncture [33].

1.3.1 Structural and Biomechanical Changes

Disc related low back pain may be associated with herniation of the NP due to mechanical failure of the AF [34, 35], typically occurring due to progressive degeneration or acute injury. In the degenerated IVD, mechanical integrity is compromised as proteoglycan content decreases while collagen denaturation increases. These degenerative changes lead to abnormal loading and eventual tearing of the AF, opening the door for mechanical failure of the IVD.

Tissue-level changes during disc degeneration include loss of disc height due to desiccation of the NP, loss of AF layers, tearing and delamination of the AF, and protrusion and herniation of the NP. Loss of disc height is thought to be related to CEP damage and loss of porosity, reducing the exchange of nutrients and leading to cell death or senescence [15] and eventually a reduction in the production of proteoglycan molecules responsible for attracting water into the disc and creating the swelling pressure giving the disc its height [36, 37]. Decreased swelling pressure decreases the weight-bearing capacity of the disc and reduces the disc height, forcing the AF to bear an abnormal load [38].

Along with increased biomechanical stress, changes in ECM metabolism contribute to the loss in the number of distinct AF layers as the distribution of collagen fiber bundles become irregular, with buckling of fibers [39, 40]. With a dehydrated NP and diminished AF lamellar structure, the normal anisotropic characteristics of a healthy disc are reduced, resulting in insufficient load-bearing capacity in response to increased axial compression caused by depressurization of the NP [41], and leading to abnormal deformation and fiber breaks in the AF. The lamellar structure in the healthy AF is an efficient mechanism for arresting crack propagation. However, with depressurization of the NP and increased AF shearing, delamination may occur, resulting in mechanical failure of the AF. The greatest stresses during loading are observed in the

7

posterolateral region of the disc, and consequently, this is the most common location for the development of annular tears, fissures, protrusions, and herniations [20].

1.3.2   Cellular and Molecular Changes

Structural and biomechanical changes in the degenerative disc are likely the result of and may also contribute to cellular and molecular changes in the disc. In addition to the gradual loss of proteoglycans and water content in the ECM of the NP, there are also significant changes in the phenotype of NP cells from a chondrogenic to a more fibrotic phenotype [39]. Degenerated NP cells synthesize less proteoglycans and instead synthesize collagens. Moreover, it is type I collagen that is upregulated in lieu of type II collagen [39]. The degenerative microenvironment including abnormal loading resulting from a CEP damage, depressurization of the NP, and disorganization of the collagen network also affects AF cell phenotype and expression profile.

Changes in cell phenotype in degenerative discs are associated with changes in the disc microenvironment including decreased diffusion of nutrient and waste products, reduced cell viability, accumulation of apoptosis debris, upregulated catabolic enzyme activity, accumulation of degraded matrix macromolecules, mechanical fatigue failure of matrix components, and an imbalance of macromolecule ratios and distribution [42].

The degenerative disc microenvironment is acidic due to lactic acid accumulation. Decreased permeability associated with damage to the CEP and other disc tissues may increase hypoxia and reduce glucose availability in the disc to $0.5 - 5.0\%$ oxygen and < 5 mmol/L glucose, respectively [43]. This subsequently leads to the production of lactic acid due to an increase in anaerobic glycolysis in this hypoxic environment [44]. The lactic acid accumulates due to limited transport, lowering disc pH to < 6.8 or as low as 5.7 in severe cases [45]. This cyclic response

gradually worsens and leads to reduced cell viability, increased matrix degradation, and contributes to the development of a pro-inflammatory environment.

While a comprehensive understanding of the mechanisms underlying chronic low back pain remain unclear, many symptoms are attributed to chronic inflammation, supported by several inflammatory mediators [46, 47]. Cells from painful and degenerated discs have been shown to produce pro-inflammatory cytokines including tumor necrosis factor α (TNFα), Interleukin-1 (IL1), and Interleukin-6 (IL6), stimulating disc cells to release additional inflammatory and catabolic molecules [48]. The accumulation of inflammatory cytokines can increase pain and downregulate ECM synthesis slowing, or even inhibiting, regeneration in the disc [23]. In particular, IL-1α and IL-1β are thought to play a major role in the recruitment of other inflammatory mediators like TNFα and IL6 [49]. These cytokines activate NF-κβ signaling, which further promotes IL6 and IL17 expression within the disc [48]. Moreover, this pro-inflammatory feedback loop stimulates the catabolic degradation of the collagen matrix via the upregulation of proteases including MMP2, MMP13, and A Disintegrin And Metalloproteinase with Thrombospondin Motifs (ADAMTs), leading to an imbalance in matrix metabolism towards a degenerative phenotype [23, 48].

This imbalance in matrix metabolism is a key hallmark of disc degeneration, where overexpression of these proteases leads to degradation of the ECM, compromising the mechanical integrity of the disc and exacerbating the degeneration cycle. Therefore, it is imperative that matrix metabolic balance is restored to stop or slow progressive disc degermation and subsequent mechanical failure of the AF which may lead to herniation, or displacement of disc material beyond the normal perimeter of the IVD [50].

1.4   Treatment of Damaged Intervertebral Discs

1.4.1   Surgical Intervention

The standard treatment for IVD herniation is discectomy, or surgical removal of the protruding herniation tissue. Discectomy is an effective therapy for pain relief in patients suffering from sciatica due to nerve impingement. However, removing portion of the protruding NP leaves behind a hole that is classified as an annular defect, which likely contributes to the high re-herniation rates (up to 21%) and persisting postoperative LBP [4, 5]. Options for closing AF defects include suturing and insertion of tissue engineered scaffolds or an annular prosthesis. These therapies are limited in clinical evidence of long-term safety and efficacy [4] and have been suggested to further aggravate existing AF damage due to their invasive nature [40].

Oftentimes, surgeons opt to leave the annular defect to heal on its own; however, the AF has limited healing capacity related to it being sparsely cellularized and having a poor blood supply [44, 51]. Due to characteristically low cell density and limited exchange, it is difficult for even healthy discs to repair damage without intervention. Several animal studies have demonstrated that this results in partial healing of annular defects occurring only in the outer annulus, forming a granulation tissue plug and promoting neovascularization and nerve ingrowth [4, 34, 52-54]. AF healing structure varied dramatically depending on the technique used to induce injury, oftentimes resulting in a thin layer of tissue with significantly reduced strength [55].

Lumbar fusion is indicated in severe cases of degenerative instability where there is no pain relief with aggressive conservative treatment [56]. Fusion is usually achieved by the removal of disc tissue and the insertion of an autogenous bone graft or other osteoinductive material over the decorticated vertebral surfaces [57]. However, fusion procedures are not always effective, with pseudarthrosis rates increasing over time (41 - 81%), likely due to poor patient selection [58-62].

Moreover, there are many risks associated with spinal fusion, including the high likelihood of upper level degeneration and postoperative instability due to increases in stress on adjacent intact segments [63].

Many surgical interventions, including discectomy and spinal fusion, address immediate symptoms but fall short of solving fundamental causes of degeneration and pain. Currently, there is no effective treatment to repair AF damage that effectively promotes tissue regeneration and restores IVD biomechanics to provide a clinically significant therapeutic benefit [6].

1.4.2   Tissue Engineering

The primary aim of IVD tissue engineering is to restore the structure and function of the disc. Emerging biologic therapies include the delivery of some combination of biomaterials [6, 64], cells [65], growth factors [66], or other stimuli - including the delivery high frequency mechanical stimulus - to replace or regenerate the ECM [67]. Therapies that are condition- and patient-specific may produce more favorable outcomes. Discs with mild-to-moderate degeneration with a sufficient viable cell density and nutrient flux may be candidates for treatment with molecular therapies such as growth factor injections, gene therapy, or stem cell injections [65, 68]. On the other hand, more severely degenerated discs may be too damaged to respond to biological therapies and may require complete removal and replacement of the disc or fusion of the segment. While there have been many recent advances made in biomaterials, growth factors, and gene therapy [69], the primary limitation of these therapies are sustainability and biological safety concerns associated with ischemic and pro-inflammatory conditions in the IVD [23, 68]. Many of these therapeutic mechanisms are based on increasing the metabolic demand of the resident cells, which may be insurmountable in a damaged disc with diminished nutrient supply [68].

Specifically, while growth factors have been shown in several studies to upregulate matrix synthesis [70-72], nutrient demand is also increased at a rate that cannot be sustained.

1.4.3 Therapeutic Ultrasound for Stimulating Intervertebral Disc Repair

Discogenic back pain presents a major public health issue, with current therapeutic interventions limited to short term symptom relief without providing regenerative remedies for diseased IVDs. Further, many of these interventions, including discectomy and intradiscal injections, are invasive and can diminish the biomechanical integrity of the IVD [5, 73]. This has created a significant unmet clinical need for a noninvasive and biologically active treatment for IVD damage and back pain.

Recently, the potential of therapeutic ultrasound (US) for stimulating tissue regeneration has been evaluated. It is possible to deliver focused ultrasound energy to deep tissues, such as the IVD, while sparing skin, fat, and muscle tissues along the way [74]. In particular, low-intensity pulsed ultrasound (LIPUS), offers a potential treatment option, where ultrasound mechanical energy targeted to a damaged IVD may produce favorable biological response to enhance IVD repair and stall or even reverse IVD degeneration in a completely noninvasive manner.

LIPUS is a low energy, pulsed pressure waveform that primarily delivers mechanical energy, rather than thermal energy, to target tissues. LIPUS systems remove the thermal component, which is the primary mechanism of high intensity, continuous wave systems commonly used in tissue ablation and hyperthermia applications [75]. LIPUS mechanical energy in the kilopascal (kPa) range [76, 77] is transmitted into tissues as acoustic pressure waves. The mechanical signal is detected by integrin mechanoreceptors on the surface of the resident cells and is transduced into a biochemical response, ultimately triggering downstream effects, such as alterations in gene and protein expression [121]. Mechanical stimulation of the IVD cells may be

a nontoxic alternative that could be used alone or in conjunction with other forms of biochemical treatment. It is well known that IVD cells respond to mechanical stimulation by increasing proteoglycan and collagen synthesis [7-9].

There are five primary parameters commonly defined in LIPUS systems: transducer operating frequency (MHz), average acoustic intensity (mW/cm^2), duty (%), pulse repetition frequency (kHz), and treatment duration (min). LIPUS technology typically operates at low acoustic intensity values ($\leq$ 100 mW/cm^2) and transmits from low-frequency acoustic sources ($\leq$ 1.5 MHz) using short duty cycles ($\leq$ 20 %) and a pulse repetition rate around 1 kHz. These sonication parameters are significantly different from those applied in thermal therapy applications, which rely on acoustic intensities that are 1 - 4 orders of magnitude greater than LIPUS.

The majority of LIPUS studies have focused on bone regeneration [78-81], and have shown accelerated healing of bone fractures, including non-union fractures, possibly due to stimulating neovascularization at the fracture site and promoting enhanced endochondral ossification [78, 82, 83]. Interest in LIPUS has expanded in recent years with evidence that LIPUS may also stimulate repair of soft tissues.

LIPUS is a widely used and accepted modality in physiotherapy for the treatment of soft tissue injuries, likely stimulating increased perfusion to the injury site [84]. In addition, it is a good candidate for IVD tissue repair as it is capable of selectively targeting the human IVD tissue while sparing superficial tissues. It has been established that LIPUS stimulates cell proliferation and matrix synthesis in various cell types inclusive of human IVD cells [40, 85]. LIPUS has been shown to enhance the mechanical properties of acutely injured collagenous tissues including tendon, ligament, and cartilage likely due to upregulation of collagen synthesis and enhanced

alignment of collagen fibers [86-90]. Several studies provide insight into signaling pathways that mediate LIPUS-induced effects in IVD cells. LIPUS mechanical stimulus is detected by integrins on the cell surface which cluster to form focal adhesions, and in NP cells, this activates the FAK/PI3K/Akt pathway and leads to downstream gene expression of important matrix proteins such as aggrecan, and type II collagen [121]. LIPUS exposure stimulates the matrix metabolism of AF cells through the upregulate of TGF-β1 and ERK pathways [40]. In addition to promoting anabolic expression, downregulation of TNFα and other pro-inflammatory factors demonstrates that LIPUS may affect inflammatory pathways as well [91, 92].

Although LIPUS has been shown to have beneficial therapeutic effects in IVD cells, the are several limitations and challenges. Many experimental devices have been developed and used to for preclinical assessment of therapeutic US [93-97]. These typically include US transducers directed at cells cultured in a polystyrene cell culture plate in the acoustic near-field. This and similar configurations exhibit major limitations due to the presence of several acoustic phenomena related to the interaction between the acoustic wave and the plastic cell culture plate and lead to near field interference, standing wave formation, and uncontrolled temperature elevation [98]. An additional limitation is the lack of knowledge about dose-response relationships. Although researchers have demonstrated various LIPUS-induced effects, the efficacy of LIPUS is debated [99] and the mechanism of LIPUS modification of cell behavior is not well understood. While the majority of published work has focused on the established exposure settings for bone healing, there is currently no clear understanding of which LIPUS parameters cells are most sensitive to nor which parameter combination is most effective for maximizing desirable effects. However, there are limited parametric studies that have shown dose dependent LIPUS effects including increased proteoglycan synthesis in AF cells treated at higher intensities and for more days [67, 85, 100].

The principal goal of LIPUS therapy is to modulate changes in IVD matrix metabolism that in a way that alters the degeneration-synthesis balance in favor of synthesis. Additional preclinical investigations are necessary for identifying an optimal dose for patient selection as researchers seek to advance this technology into the clinic. However, the advancement of LIPUS technology to the clinic has been limited thus far, likely due to the lack of reproducibility in *in-vitro* studies, limiting the transferability into *in-vivo* models. To overcome this challenge, there is a need for a reliable *in-vitro* LIPUS exposimetry system that delivers uniform acoustic energy while eliminating standing wave formation and allowing accurate temperature control. In addition, a comprehensive exploration of LIPUS parameters is required to identify optimal dosing and therapeutic delivery protocols to generate favorable bioactivity within the IVD that can increase matrix production, stimulate remodeling, and ultimately stop or reverse the pain cascade.

It can be expected that the success of a LIPUS therapeutic may depend on the extent of degeneration in a particular disc. While mildly degenerated discs that still contain viable cells may be salvageable, discs with severely damaged tissues or unhealthy cells may not respond to any therapeutic. Ultimately, the most severely degenerated and painful discs may have lost much of their basic structure and need to be surgically removed to make way for vertebral fusion.

1.4.4 Pulsed Electromagnetic Fields for Stimulating Spinal Fusion

Spinal fusion is recommended for the restoration of mechanical stability in the spine in cases of degenerative disease that are associated with severe pain by the removal of disc tissue and the formation of a bone bridge in the intervertebral space. The process of spinal fusion is mechanistically similar to bone fracture regeneration as it includes an inflammatory stage, callus formation stage, and a bone remodeling phase [101]. Bone grafts are widely used to promote vertebral fusion, and the gold standard procedure involves the placement of an autogenous bone

graft between the vertebrae. However, autogenous grafts are limited by increased surgical time, significant donor-site morbidity, and high rates of pseudarthrosis [60]. High rates of pseudarthrosis have be addressed by the use of bone graft substitutes including collagen, calcium phosphate, tricalcium phosphate, and demineralized bone that are engineered to be highly osteoinductive, osteoconductive, and osteogenetic [102, 103]. Other techniques that have shown some success in increasing fusion rates include the use of bone grafts loaded with osteoinductive proteins such as recombinant human bone morphogenetic protein-2, bone marrow aspirates, mesenchymal stem cells, or platelet-rich plasma [104, 105]. Recently, novel technologies such as gene therapy and tissue engineered biomaterials have shown promising results in animal studies [106]. While many of these methods have shown to accelerate fusion, many are plagued by lack of clinical outcomes data, high cost of procedure, and low efficiency [60, 107].

Pulsed Electromagnetic Field (PEMF) stimulation therapies have shown success in the clinic as a noninvasive treatment modality for promoting bone healing [108, 109], including increased fusion rates for cervical and lumbar fusions in high-risk patients [110]. PEMF devices such as the SpinalSTEM™ device (Orthofix Medical Inc., Lewisville, TX, USA) have shown high clinical success rates and is FDA approved for cervical and lumbar spinal fusion.

PEMF signals are commonly defined by four main parameters: waveform type, frequency, intensity, and pulsing scheme. Most PEMF systems produce low frequency a sine or square waves in the range of 1 Hz to 10 kHz and relatively low magnetic field intensities on the order of 0.2 – 0.4 T. For example, the Physio-Stem waveform (Orthofix Medical Inc.) consists of a square wave with a 25% duty cycle, 3.85 kHz frequency, 15 Hz burst frequency, and slew rate of 10 T/s [111]. Clinical studies utilizing comparable PEMF signals have validated the effectiveness of PEMF

devices, showing these signals to be safe and effective in improving fusion rates as an adjective treatment [110] as well as promoting fusion in patients with established pseudarthrosis [112].

Considering the strong evidence for the osteoinductive properties of bone graft substitutes such as tricalcium phosphate [113-115] as well as PEMF signals, there is increasing interest in the investigation of their potential to synergize to enhance bone healing.

1.5   Overview of Chapters

The central objective of this dissertation is to contribute to the development of two novel energy-based therapeutic modalities for treating IVD pathologies and alleviating low back pain. Towards this goal, the following chapters are broken down as follows:

While there are promising *in-vitro* studies demonstrating the effects of LIPUS stimulation on cultured IVD cells, there is a lack of published work demonstrating the effects of LIPUS in an *in-vivo* model of IVD degeneration. **Chapter 2** demonstrates the technical feasibility of delivering targeted LIPUS energy to a rat-tail IVD and evaluates LIPUS-induced effects on gene expression in rat-tail IVDs with acute injury. A LIPUS exposimetry system was fabricated and characterized to verify the delivery of acoustic energy to the center of the rat-tail IVD. Discs were injured using an established stab-incision model for disc degeneration then treated with LIPUS for 20 minutes daily for five days. IVDs treated with LIPUS demonstrated significant upregulation of type II collagen and downregulation of TNFα gene expression. The results of this study indicate technical feasibility of targeted delivery of ultrasound to a rat-tail IVD for studies of LIPUS biological effects and also suggest that LIPUS may modulate gene expression of cells in inflammatory conditions.

The results of this *in-vivo* work lead to increased interest in understanding dose-response relationships between LIPUS and IVD cells. In preparation for a comprehensive parametric

analysis, we identified a need for a fully characterized and validated *in-vitro* LIPUS system that mitigates the confounding factors often observed in conventional *in-vitro* LIPUS configurations. This need inspired the work presented in **Chapter 3**, which describes the development and validation of a far-field LIPUS exposimetry system for stimulating matrix synthesis in bovine AF cells. We designed and fabricated a LIPUS exposimetry system that mitigated previously found problems with nonuniform near-field exposure, beam reflections, and temperature elevation within target samples. When bovine AF cells were exposed to far-field LIPUS, sample heating was minimal and collagen content was increased by 2.6-fold compared to the control and was equivalent to BMP-7 growth factor treatment. The results of this study support the gene expression results in **Chapter 2** and suggest that LIPUS is a potential noninvasive therapeutic for stimulating IVD repair.

Motivated by the LIPUS-induced effects observed in Chapter 2 and following the successful development and validation of a relevant preclinical LIPUS system as described in Chapter 3, **Chapter 4** explores the dose-response relationships between LIPUS and ECM gene expression in inflammatory AF cells. In this chapter, we present the use and validation of Design of Experiments (DOE) for LIPUS parameter exploration, response prediction, and dose optimization. We modeled the effects of LIPUS peak intensity, pulse repetition frequency (PRF), and treatment duration, simultaneously, on ECM gene expression in inflammatory AF cells using a screening DOE. We found that LIPUS exposure significantly downregulated MMP1, MMP13, and IL6 gene expression but did not significantly affect COL1 gene expression, and that PRF was the most significant factor for modulating MMP1, MMP13, and IL6 expression, while peak intensity was most significant for modulating COL1 expression. Validation experiments demonstrated that DOE-predicted responses were 12 - 86% different from actual responses. The results of this study demonstrate

LIPUS-induced anti-catabolic and anti-inflammatory activity in AF cells and illustrate the capability and benefits of implementing DOE in the context of therapeutic ultrasound optimization.

Chapters 2 – 4 explore the use of LIPUS for stimulating IVD repair; however, in severe cases where IVD degeneration has progressed beyond repair, spinal fusion may be necessary. Due to high pseudarthrosis rates, there is increased interest in the development of adjuvant therapies for improve the rate of successful bone fusion. **Chapter 5** describes a study exploring how magnetic nanoparticles synergize with pulsed magnetic fields to stimulate osteogenesis *in-vitro*. Intrinsically magnetic nano-bone substitutes (MNBS) were added to human mesenchymal stem cell culture and cell viability, alkaline phosphatase activity, mineralization, and osteogenic gene expression in the presence and absence of PEMF were quantified for up to 10 days. MNBS attached to the surface of and were internalized by human mesenchymal stem cells without impacting cell viability. PEMF combined with MNBS accelerated the induction of osteogenesis demonstrated by an early peak in ALP activity compared to all other treatment groups. Moreover, PEMF combined with MNBS demonstrated continuously increasing mineralization over time. The results of this study demonstrate the synergistic effects of PEMF and MNBS on osteogenesis and highlight a potential combination therapy for improving spinal fusion success rates.

Chapter 6 summarizes the conclusions of this dissertation and suggests areas for future work. In particular, this chapter discusses the use of response surface methodology to expand upon the DOE models generated in Chapter 4, and also discusses the development of an animal model to further explore whether the findings in Chapter 5 translate to an *in-vivo* model of spinal fusion.

Chapter 2 is a published conference proceedings article in the *Proceedings of SPIE*, and Chapter 3 is a published research article in *Biomedical Physics and Engineering Express.* Chapter 4 represents a body of work that is currently being expanded upon and will be submitted

as a manuscript to *Ultrasound in Medicine and Biology* in June 2020. Chapter 5 is a manuscript that was recently submitted and is currently in review for publication in *Tissue Engineering, Part A.*

2   LIPUS Regulates Type II Collagen and TNFα Expression in Injured Rat-tail Discs

The content of this chapter is published as a conference proceedings article in the Proceedings of SPIE with the following citation: *Horne D, Jones P, Salgaonkar V, et al (2017) Low Intensity Pulsed Ultrasound (LIPUS) for the treatment of intervertebral disc degeneration. SPIE BiOS. SPIE, pp 1006609–7. doi: 10.1117/12.2255761*

2.1   Introduction

Discogenic back pain (DBP) is one of the most significant non-lethal medical ailments in society. The American Academy of Orthopaedic Surgeons estimates that more than 6 million people are diagnosed with DBP annually, with 80% of the US population experiencing DBP sometime in their lives. The treatment costs of lower back pain exceed $27 billion annually, but the societal cost of the disease exceeds $86 billion [3, 116-118]. The intervertebral disc (IVD) is an articulating, load-bearing structure between the vertebral bodies of the spine. In the center of the disc is the nucleus pulposus (NP); this proteoglycan-rich structure imbibes water and provides compressive resistance. Surrounding the NP are lamellae of collagen fibers called the annulus fibrosis (AF) which accounts for tensile strength. Between the IVD and each vertebral body is the cartilage end-plate which serves as a barrier for nutrient and waste exchange between the IVD and vertebra. Intervertebral disc degeneration is associated with the loss of extracellular matrix (ECM) molecules, resulting in modification in biochemical and biomechanical tissue properties. While the etiology of IVD degeneration is unclear, it is suspected that it is the result of metabolic imbalance within the tissue [119]. This imbalance may cause a gradual loss of important matrix proteins such as aggrecan and type II collagen, which may lead to depressurization of NP and breakdown of the AF. Another factor likely related to disc degeneration is cartilage end-plate damage which may impair proper nutrient and waste exchange, leading to a loss of cells due to

apoptosis. Current therapeutic options for treating discogenic back pain include procedures such as discectomy (removing part of most of the disc nucleus) and laminectomy (removing part of the bone anatomy), which are largely focused on addressing manifested symptoms (i.e. pain) rather than functional causes. The major limitations of these procedures are that they are invasive and may actually lead to biomechanical failure and further degeneration. Incidence rates and costs associated with biomechanical damage from these interventions are significant, creating a significant need for noninvasive alternatives. Recently emerging alternative strategies for treating IVD degeneration including cell transplantation, gene therapy, and growth factor injection are under investigation. While these options have advantages over invasive surgeries, their primary limitations include concerns about sustainability and biological safety. Mechanical stimulation of the IVD cells may be a nontoxic alternative that could be used alone or in conjunction with other forms of biochemical treatment.

Low intensity pulsed ultrasound (LIPUS) is a mechanical treatment option that is potentially both noninvasive and regenerative. LIPUS is a low energy, pulsed waveform, removing the thermal component found at higher intensity, continuous wave systems. LIPUS technology typically operates at low acoustic intensity values (30 mW/cm^2) and transmits from low-frequency acoustic sources (1.5 MHz) using short duty cycles (20%) and a pulse repetition rate around 1 kHz. These sonication parameters are significantly different from those applied for heat-induced interventions, which rely on acoustic intensities that are $1 - 4$ orders of magnitude larger than LIPUS. LIPUS has been shown to accelerate healing of cortical and cancellous bone fractures [120], including non-union fractures, possibly due to enhanced callus formation and angiogenesis near the fracture site [81]. LIPUS is widely used in physiotherapy for the treatment of soft tissue injuries, likely stimulating increased perfusion to the injury site [84].

IVD degeneration is known to result from alteration in biosynthesis of proteoglycan (PG) and pro-inflammatory cytokines in the disc [119]. It has been established that LIPUS stimulates PG and collagen synthesis, and induces an anti-inflammatory and anti-catabolic responses in human IVD cells [121]. These LIPUS effects have been shown to be mechanically regulated through the FAK/PI3K/Akt pathway [121]. Promoting the synthesis of major ECM proteins and reducing inflammatory factors may stall or even reverse the degenerative cascade. While findings support the application of LIPUS for repair of IVD damage and degeneration, it is unclear whether these LIPUS effects are translatable to an *in vivo* IVD degeneration model. We hypothesize that LIPUS can be applied noninvasively to stimulate favorable biological activity within the acutely damaged rat tail IVD. The objective of this research project was to demonstrate the technical feasibility of building a LIPUS system that can target the rat tail IVD and apply this setup to a model for acute IVD degeneration.

2.2   Methodology

2.2.1   Ultrasound exposimetry system

Ultrasound exposimetry systems were devised and fabricated, following our generalized schema **(Figure 2.1 a)**, specific to delivering calibrated and characterized LIPUS to rat tail intervertebral discs. Three configurations considered consisted of 2.5 cm diameter PZT4 transducers (1.0 MHz, f=1; 1.6 MHz, f=3.8; 1.0 MHz planar), mounted water-tight with air-backing on a 3D-printed assembly, and integrated within a degassed water-filled plastic housing with a thin Mylar window marked with central cross-hairs **(Figure 2.1 b)**. The housing is designed as an acoustic standoff to place the distal focus, or uniform far-field zone, within the targeted rat tail disc and to prevent the influence of transducer heating. The acoustic energy is isolated to a single targeted disc and portions of the adjacent vertebral body by selection of a standoff distance

which gives an appropriate beam cross-section. Additional isolation was achieved by use of peripheral brass reflectors and a custom acoustic absorber placed beyond the target **(Figure 2.1 a)**.
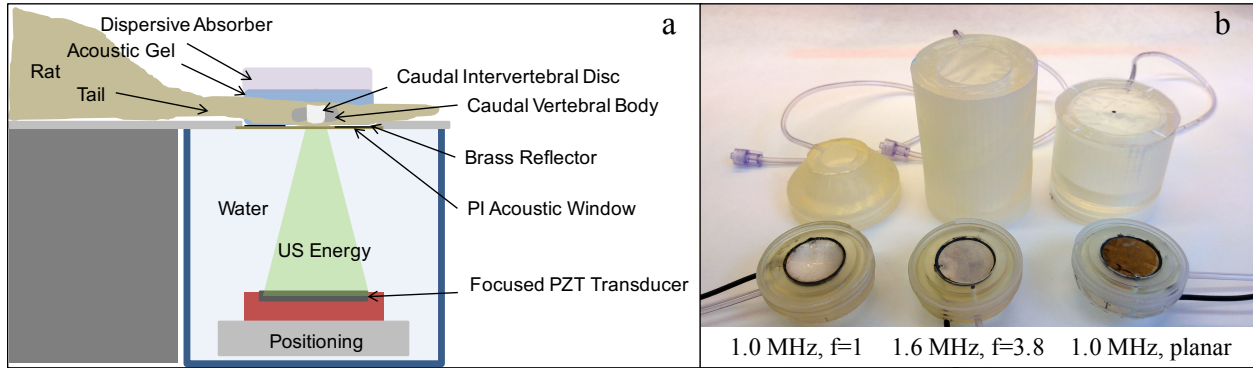
Figure 2.1 Generalized schematic representing the *in-vivo* LIPUS exposimetry system
The system was designed for LIPUS delivery with calibrated intensity to rat-tail IVDs (a). LIPUS applicators were constructed with various frequencies and focusing (b).

2.2.2   Acoustic characterizations

LIPUS applicators were evaluated with comparative beam plot measurements to assess whether the systems can deliver LIPUS to the narrow (~1.5 mm x 5 mm) rat tail disc. The planar device with a 5 cm standoff provided a more uniform beam of appropriate width (~8 mm) for easier alignment and full exposure of the disc **(Figure 2.2 a)**. Partial disc exposure may be achievable with focused devices (< 3 mm) **(Figure 2.2 b, c)**. Radiation force observations and intensity measurements, with and without insertion of sectioned rat tails *ex vivo,* were made to evaluate whether sufficient intensity could reach the center of the rat tail disc **(Figure 2.3)**. It was confirmed that approximately 45% incident energy was delivered to central disc while reducing

exposure to significant portions of the adjacent bone and with negligible (< 1°C) temperature elevation measured.
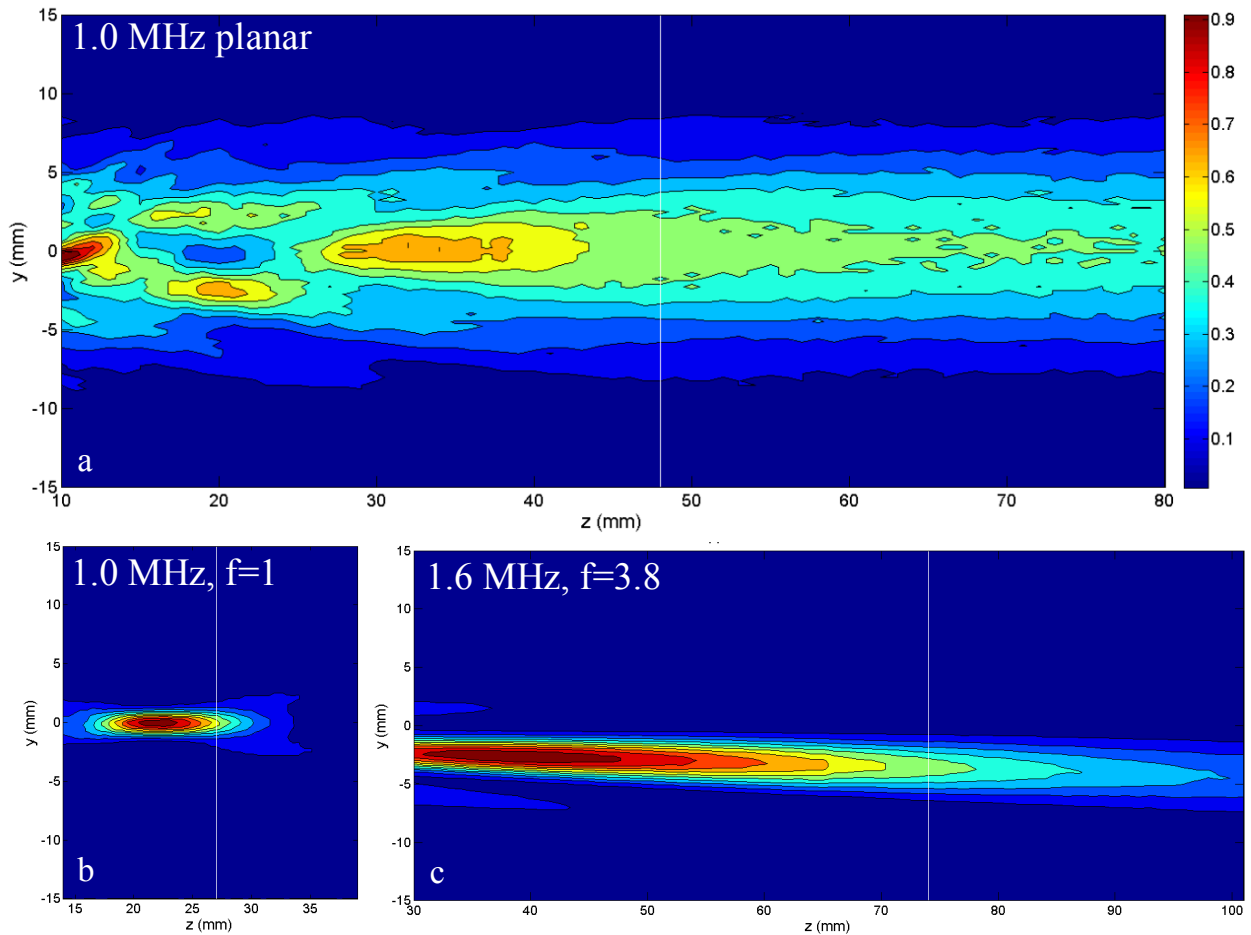
Figure 2.2 Axial beam plots with selected standoff distance marked by vertical line
Plots are representative of a planar transducer (a) and transducers of different focusing (b and c).

2.2.3 Rat tail stab model

A well-characterized and established protocol demonstrates that a single stab incision through the rat tail intervertebral disc induces inflammation that mirrors the early stages of IVD degeneration [122]. Five three-month-old female Sprague-Dawley rats were used in this study. All procedures were approved by the Institutional Animal Care and Use Committee of the University of California, San Francisco. Rats were anesthetized and an analgesic (Buprenorphine,

0.01 mg/kg) was delivered before stab-incisions were administered. Rat tails were sanitized with alcohol wipes and betadine topical antiseptic solution. The 3 most proximal discs were selected; two to be stabbed and the remaining disc as a control. Under fluoroscopic guidance, a 20-guage, short-bevel needle (Fisher Scientific, Cat. No. 305179) was laterally inserted through the disc and stopped just before penetrating the outer annulus on the opposite side. The needle was turned 180° before fully retracting the needle. Injury to multiple discs does not result in systemic inflammation in rats nor does it affect healthy adjacent discs. Female rats were chosen over male rats since previous studies have suggested that male rats are more aggressive and may bite the injury site of other rats in the cage, potentially affecting results. Relative disc location was marked with a tissue pen and verified daily with fluoroscopy prior to LIPUS treatment.
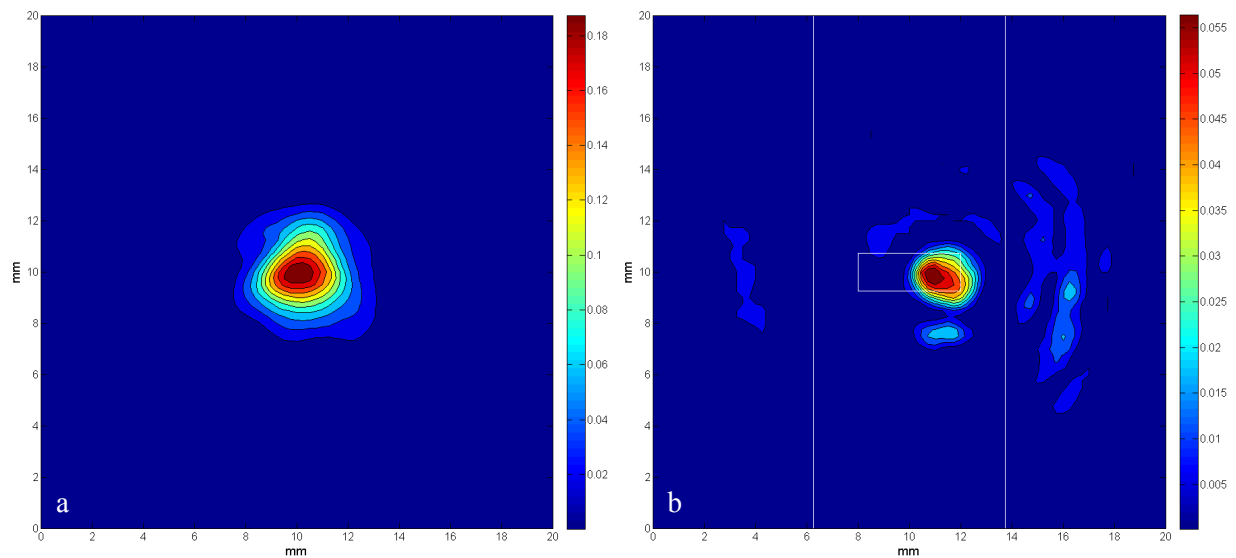
Figure 2.3 Transverse beam plots of acoustic energy passing through rat-tail disc tissue
Intensity distributions of a 1.6 MHz, focused transducer; without sectioned tail (a) and with sectioned tail in beam path (b).

2.2.4 LIPUS delivery

LIPUS was delivered shortly following the completion of stab incisions. Five daily LIPUS exposures (I_{SPTA} 60 mW/cm^2, 200 µs burst, 1 kHz repetition frequency, 20 min duration) were

applied to one disc and compared to stab only and normal controls. Acoustic coupling gel was applied between the applicator and tail, and a silicone absorber coupled with gel was mounted on tail **(Figure 2.4)** to best reduce standing waves and reflections off of the dorsal surface. Day 1 exposure was 30 min after injury, and Day 5 sacrifice was 2-3 hours post-LIPUS.
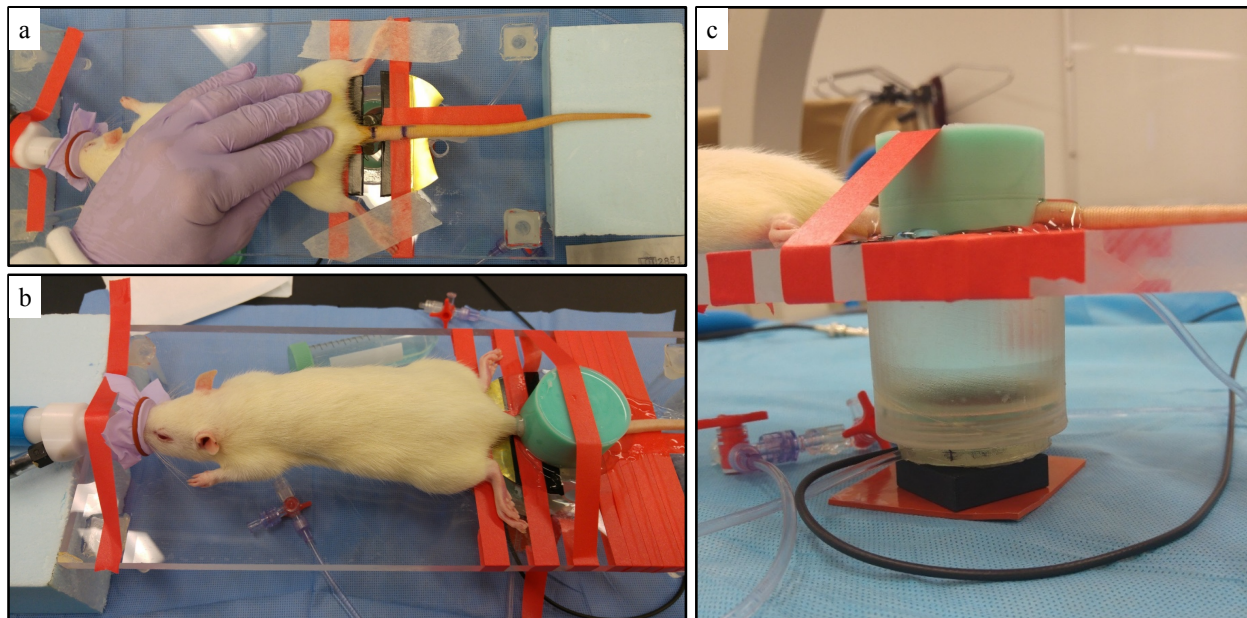
Figure 2.4 Rodent positioning and LIPUS delivery system during treatment
Caudal vertebral segment of anesthetized rat positioned over center of aperture (a). Ultrasound gel and apical absorber secured prior to treatment (b). Assembly uses a 1.0 MHz planar transducer with a 5-cm standoff, delivering an 8-mm diameter beam (i.e. FWHM = 8 mm) to the surface of the tail (c).

2.2.5 Histology

After day 5 treatment, a cohort of rats was euthanized, and motion segments were harvested. Discs and adjacent vertebrae were harvested, fixed in formalin, decalcified in formic acid, dehydrated, and embedded in paraffin. Sagittal sections were cut through the motion segments, perpendicular to the direction of the stab. Sections were stained with Heidenhain's stain. Disc and vertebral morphology were examined at 2X magnification.

2.2.6   Measurement of gene expression

The remaining cohorts of rats were euthanized following day 5 treatment and complete discs were harvested and snap frozen in liquid nitrogen. Disc tissue was homogenized, and total RNA was extracted using the using Trizol reagent (Life Technologies, Cat. No. 15596026) and the RNeasy mini kit (Qiagen, Cat. No. 74104); cDNA was synthesized using iScript reverse transcriptase (BioRad, Cat. No. 1708840). The mRNA expression of matrix related (ACAN, Col2a1, Sox9) and pro-inflammatory cytokines (TNFα, IL-1β, IL6) were measured by RT-qPCR with TaqMan Fast Advance Master Mix (Life Technologies, Cat. No. 4444557) using the BioRad CFX96 RealTime Thermal Cycler. Relative gene expression was calculated using the ΔΔCt method and normalized to B2M and the control group. Results were compared using *t-tests*. *P* values < 0.05 were considered significant.

2.3   Results

2.3.1   Stab-induced Morphological Changes

All control discs appeared to have a rounded nucleus and well-organized collagen lamellae in the annulus **(Figure 2.5)**. Stab incisions resulted in depressurization of the disc and reduced disc height **(Figure 2.5)**. Stabbed discs displayed an irregularly shaped nucleus and denatured collagen fibers that appear lax in the inner annulus. These are all positive signs of acute disc injury and precursors to further degeneration.
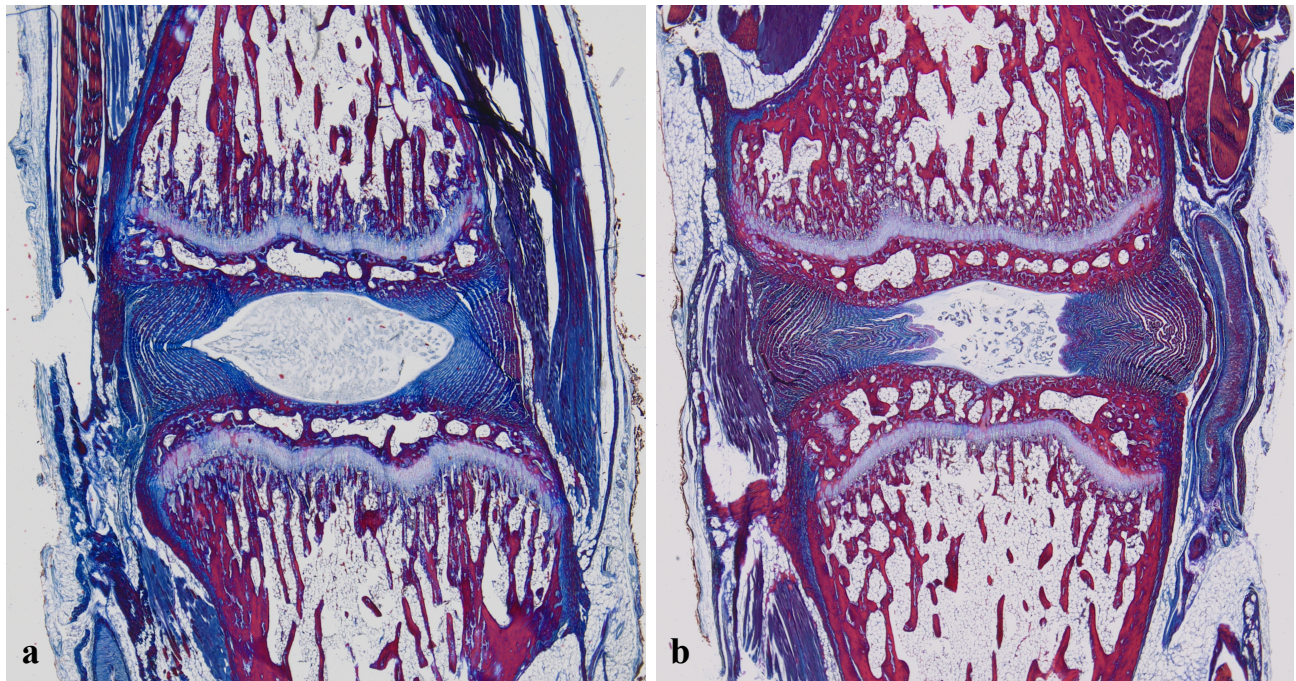
Figure 2.5 Mid-sagittal histology sections of rat-tail motion segments
Control discs (a) display a rounded nucleus and lamellae of collagen in the annulus, while stabbed discs (b) are depressurized and have lax collagen fibers in the annulus. Note that stab orientation was into the page.

2.3.2 LIPUS Effect on Gene Expression

Real-time quantitative PCR analysis was performed at 5 days after injury to assess the impact of LIPUS stimulation on extracellular matrix and inflammatory gene expression. Previous *in vitro* studies suggest that LIPUS treatment stimulates proteoglycan and collagen synthesis in IVD cells while inhibiting pro-inflammatory cytokine expression [67, 85, 121, 123]. Results indicated favorable trends but exhibited large variation when gene expression was averaged over all animals (n = 5), showing no statistical significance between stab only and stab plus LIPUS groups. However, as typically applied with the stab-injury model, when selecting the subset (n = 2) of animals that had successful stabs which produced a significant injury response, LIPUS treatment had an anti-inflammatory effect and anabolic response **(Table 2.1)**: Col2a1 expression was significantly upregulated (p = 0.03) and TNFα expression was significantly downregulated

(p = 0.05). Expression of pro-inflammatory cytokines IL–1β and IL6 was not significant affected, but results suggest a trend towards downregulation. Unexpectedly, LIPUS appears to downregulate Aggrecan and Sox9 gene expression.

Table 2.1 Gene expression after 5 days of LIPUS treatment
Data have been normalized by their respective control group. Fold change is reported as an average among animals with an injury response (n = 2).

| Gene | Gene Name | Description | Fold Change | | |
			Stab Only	Stab + LIPUS	*p* - value
IL-1β	Interleukin – 1β	Pro-inflammatory Cytokine	5.54	1.00	0.25
IL6	Interleukin – 6	Pro-inflammatory Cytokine	3.57	0.20	0.42
TNFα	Tumor Necrosis Factor – α	Pro-inflammatory Cytokine	1.29	0.02	0.05*
ACAN	Aggrecan	ECM Protein	2.48	1.61	0.74
Col2a1	Collagen type 2a1	ECM Protein	1.56	16.31	0.03*
Sox9	Sox9	Transcription factor for Collagen II synthesis	2.61	1.65	0.62

2.4   Conclusions

This preliminary study demonstrates technical feasibility of delivering LIPUS isolated to a targeted rat tail IVD for the study of LIPUS exposure and biological effects. Our analyses indicate that previously observed *in vitro* effects seem to carry over to our *in vivo* model. While several favorable trends were observed, statistical significance was only achieved in two genes of interest, likely due to large animal to animal variation. One of the major limitations of the rat tail stab model is that minute variations between individual's stabbing technique may significantly affect the

animal's injury response. Future studies will include additional animals to improve statistical power as well as implementation of a refined stab technique to ensure more a consistent injury response. Subsequent studies will evaluate a wider variety of genes to determine the healing mechanism by which LIPUS most significantly acts (e.g. anti-inflammatory, anti-catabolic, anabolic). Additional end points (14 and 28 days) will be included to assess the healing response over time. Successful completion of these studies can lead to similar evaluations in larger IVD degeneration models (e.g. ovine, bovine), to more closely replicate the dimensions of the human IVD and lead to development of delivery strategies for treating discogenic back pain in humans.

2.5   Acknowledgements

3   LIPUS Far-field Exposimetry System for Uniform Stimulation of Tissues *in-vitro*: Development and Validation with Bovine Intervertebral Disc Cells

The content of this chapter is published as a research article in *Biomedical Physics and Engineering Express* with the following citation: *Horne DA, Jones PD, Adams MS, et al (2020) LIPUS far-field exposimetry system for uniform stimulation of tissues in-vitro: development and validation with bovine intervertebral disc cells. Biomed Phys Eng Express 6:035033–13. doi: 10.1088/2057-1976/ab8b26*

3.1   Introduction

Ultrasound (US) can deliver mechanical or thermal energy to induce therapeutic effects including hyperthermia, ablation, regeneration or remodeling, enhanced local drug delivery, and immunotherapy [77, 124-127]. Devices for these purposes can be distinguished by their dimensions and position relative to the body, driving frequency and acoustic waveforms, as well as spatial-temporal intensity and pressure profiles, all of which largely dictate the distribution of the acoustic energy delivered and the effects on tissue. Low-intensity pulsed ultrasound (LIPUS) is one therapeutic US approach that is applied in pulsed wave modes with relatively low average intensities, thereby generating little to negligible heating and primarily delivering mechanical energy [125]. Therapeutic LIPUS has been shown to have significant regenerative capabilities in numerous tissue types through stimulation of cellular proliferation and matrix metabolism [78, 82, 88, 128-135]. Recently, with U.S. Food and Drug Administration approval for bone fracture healing, LIPUS has advanced into the clinic as a noninvasive and regenerative therapy.

Interest in therapeutic LIPUS has expanded in recent years with evidence that LIPUS may also stimulate repair of injuries in soft tissues including cartilage, ligament, tendon, and intervertebral disc (IVD). Several *in-vivo* studies have demonstrated LIPUS-induced enhancement

of wound healing by stimulating increased collagen synthesis and alignment, tissue integration, and improved biomechanical function including enhanced stiffness and failure strength [87, 89, 136-138]. Additionally, LIPUS has been shown to promote matrix anabolism in IVD cells by increasing collagen and glycosaminoglycan synthesis while simultaneously decreasing matrix metalloproteinase expression [40]. Yet, there is little known about the mechanism of its effects at the cellular level, nor which other cell or tissue types may respond to LIPUS exposure. The Exogen® clinical system, and other experimental devices, have been used to evaluate LIPUS bioeffects [67, 139-144], with the majority of published work focused on the established exposure settings for bone healing (1.5 MHz; 200µs pulse; delivered at 20% duty cycle (1kHz); ISATA 30 mW/cm^2; 20 minutes daily). Investigations of LIPUS bioeffects at other exposure settings, such as at frequencies below 1.0 MHz and acoustic intensity profiles representative of far-field (FF) delivery, are limited and may be required for acoustic energy to penetrate to deep tissues such as the human IVD.

In-vitro testing systems have been developed for preclinical assessment of therapeutic US under controlled experimental conditions. In the most common LIPUS configuration, cells are exposed by placing a commercial polystyrene cell culture plate (CCP) containing cellular material in the acoustic near-field (NF), directly on top of the US transducer with acoustic coupling gel. While a simple and straightforward approach, this configuration is vulnerable to several undesirable acoustic artifacts including NF interference, standing wave formation, and uncontrolled temperature elevation [98]. These phenomena represent significant confounding factors when attempting to establish dose-response relationships [145]. Many groups have studied US fields in CCPs [93, 94, 96, 98, 145, 146]. Hensel et al. (2011) investigated the wave propagation characteristics of several typical *in-vitro* configurations. They reported that reproducibility was

negatively affected by reflecting surfaces (i.e. allowing standing wave formation), and that small differences in system configuration, such as well size, media volume, and alignment with beam axis can significantly affect the acoustic field distribution and ultimately the biological response. Further, the effect of uncontrolled temperature fluctuations due to direct heating from contact with the US transducer as well as absorption of US-energy and heating within the plastic well-bottom and sidewalls can be particularly problematic. LIPUS systems have previously been developed to address these confounding factors. Fung et al. (2014) varied the acoustic standoff distance of their *in-vitro* LIPUS system and found that osteocytes were sensitive to the axial distance of LIPUS, suggesting that FF US exposure could enhance osteogenic activities. In the system developed by Marvel et al. (2010), BioFlex CCPs with flexible well-bottoms were used and found to be more acoustically transparent than typical polystyrene CCPs. In the 2014 study by Leskinen et al., the authors found that there was substantial temperature variation among different wells within a CCP, and that this variation correlated with variations in cell behavior. They found that temperature elevations were minimal when using a CCP well area larger than the width of the US beam [147]. Additionally, several LIPUS studies have implemented the use of an acoustic absorber placed above the CCP well to attenuate standing wave formation [94, 96, 98, 148]. These results highlight the importance of characterizing parameter- and configuration-specific acoustic field distributions and temperature fluctuations during *in-vitro* LIPUS exposure.

In consideration of investigating extracorporeal delivery of LIPUS to deep tissue targets such as IVDs, lower than typical transducer operating frequencies and focused or uniform FF exposure are assumed technical requirements. The objective of this study was to design and characterize an *in-vitro* LIPUS system that mimics attributes of a deep delivery system, and as such delivers uniform, FF acoustic energy profiles while minimizing reflections and standing waves within

target wells and unwanted temperature elevation within target samples. Further, the system was validated by exposing IVD cells and assessing LIPUS-induced biological effects.

3.2 Methods

3.2.1 System Design and Characterization

To meet the primary objective of maximizing FF acoustic dose uniformity at the location of the target sample in the *in-vitro* setup, CCP dimensions, transducer dimensions, and offset distance between the transducer surface and the CCP-well were determined. Two CCP setups were evaluated, each with an effective cell culture area of 1.91 cm^2. One setup included a narrow 24-well plate (15.6 mm diameter), and the other a wider 6-well plate (34.8 mm diameter) with a custom toroidal spacer (15.6 mm inner diameter). This spacer serves to constrain the cells within the CCP-well center while limiting exposure to sidewall acoustic reflections and maintaining a small volume similar to the 24-well plate. To identify the ideal separation distance from the transducer to the CCP-well (acoustic standoff) for specific CCP well coverage, several constraints were imposed: (i) the acoustic standoff must place the target sample beyond the heterogeneous NF; (ii) the full width at half maximum (FWHM), or 50% contour of beam maximum, must cover at least 80% of the effective cell culture area (1.91 cm^2); and (iii) the acoustic standoff distance and minimum transducer size must be constrained to avoid an excessively divergent field and potential well-wall absorption and reflections.

3.2.1.1 Specification and Characterization of Transducers

Transducer specifications were identified by investigating a range of transducer diameter (20 – 35 mm), frequency (0.5, 1.0, and 1.5 MHz), and acoustic standoff distance within the FF (120 – 400 mm) on corresponding US intensity distributions, uniformity, and coverage area based upon acoustic field simulations. Full-field acoustic intensity distributions were calculated using

the rectangular radiator method [149] for numerical approximation to the Raleigh-Sommerfield diffraction integral, applying methods previously described by our group [150], and assuming uniform velocity across the transducer surface.

Planar disc PZT US transducers of 25 mm diameter (EBL #1, EBL Products, Inc., East Hartford, CT, USA), with a resonant frequency of approximately 0.5, 1.0, or 1.5 MHz, were selected. Transducer assemblies were fabricated separately with water-tight air-backing on custom 3D-printed housing fixtures, as designed in Solidworks (Dassault Systemes, Waltham, Massachusetts, USA) and printed using the Clear resin material with a Form 2 3D-printer (Formlabs Inc., Somerville, MA, USA). Black silicone adhesive sealant (Permatex 81158, Solon, OH, USA) was applied along the edge of the transducer to secure it to the fixture and ensure air-backing. Peak electrical impedance, zero phase cross-over, and resonance frequency for each transducer were measured using a Network Analyzer (E5070B ENA RF, Agilent). Acoustic beam plots of the intensity patterns for each transducer were acquired in the transverse plane using a custom 3D computer-controlled scanning system (Velmex, Bloomfield, NY, USA) with a calibrated hydrophone (HNP-0400, Onda Corp, Sunnyvale, CA, USA). Transducers were placed in a tank lined with an acoustic absorber to reduce reflections and filled with deionized, degassed water. A function generator (HP 33120A, Agilent, Santa Clara, CA, USA) and RF amplifier (ENI 240L) were used to drive transducers with a power meter (N1914A EPM, Keysight Technologies, Inc., Santa Rosa, CA, USA) and power sensor modules (N8482A, Keysight Technologies, Inc., Santa Rosa, CA, USA) in-line for monitoring forward and reflected power. For hydrophone measurements, a standard burst mode signal at the primary resonant frequency was used (1kHz pulse repetition, 100-200 cycle burst). Hydrophone scanning step sizes were 0.2 mm x 0.5 mm across transverse and axial axes, respectively. The peak-to-peak voltage (Vpp) signal from the

hydrophone was measured using a digital oscilloscope (DSOX2024A 200 MHz, Keysight Technologies, Santa Rosa, CA, USA) and converted to absolute intensity maps. Beam intensity distributions were calculated, normalizing the maximum intensity value to one in each case to provide a simplified comparison of distributions.

3.2.1.2 Assembly of LIPUS in-vitro System

Informed by the simulations and measurements described above, exposimetry systems were devised and fabricated in-house following the schema **(Figure 3.1)**. The LIPUS system consists of two independently driven, planar transducers mounted separately and affixed to an acrylic base. In order to operate with a single amplifier and function generator, paired transducers for each test system were individually impedance matched to a 100Ω load using an LC matching network and connected in parallel to achieve $50\ \Omega$ resultant impedance. The matching network capacitance was adjusted slightly for final matching to equalize peak output intensities as measured by needle hydrophone. The CCP-platform was fixed at the identified acoustic standoff for each frequency, as described above, and the transducer position was adjusted to direct acoustic energy towards the center of two opposing corner wells of the CCP. In order to further reduce well-wall reflections and US beam refocusing as observed when using narrow-diameter 24-well plates, a wide-diameter 6-well CCP (Costar 3471, Corning Incorporated, NY, USA) was used. An alginate disk (34.8 mm diameter; 10 mm height) was formed by mixing equal volumes of 1.2wt% sodium alginate (FMC BioPolymer, San Jose, CA) and 102 mM $CaCl_2$ crosslinking solution inside each test well. Following 10 min incubation and removal of the crosslinking solution, a 3D-printed boring tool (15.6 mm outer diameter) was used to remove the center portion of the disk, creating an alginate ring. The acoustically transparent alginate rings (measured attenuation coefficient = 0 dB/cm) were used to constrain target samples within the FWHM of the diverging US beam and

maintain a sample volume comparable to the 24-well plates without introducing reflective surfaces. Two custom silicone absorbers (described in detail below) were positioned apically and coupled on the distal surface of the media-filled target wells. During exposures, the entire setup was placed in a deionized, degassed, and temperature-controlled water bath, with the water level reaching one-half the height of the CCP.
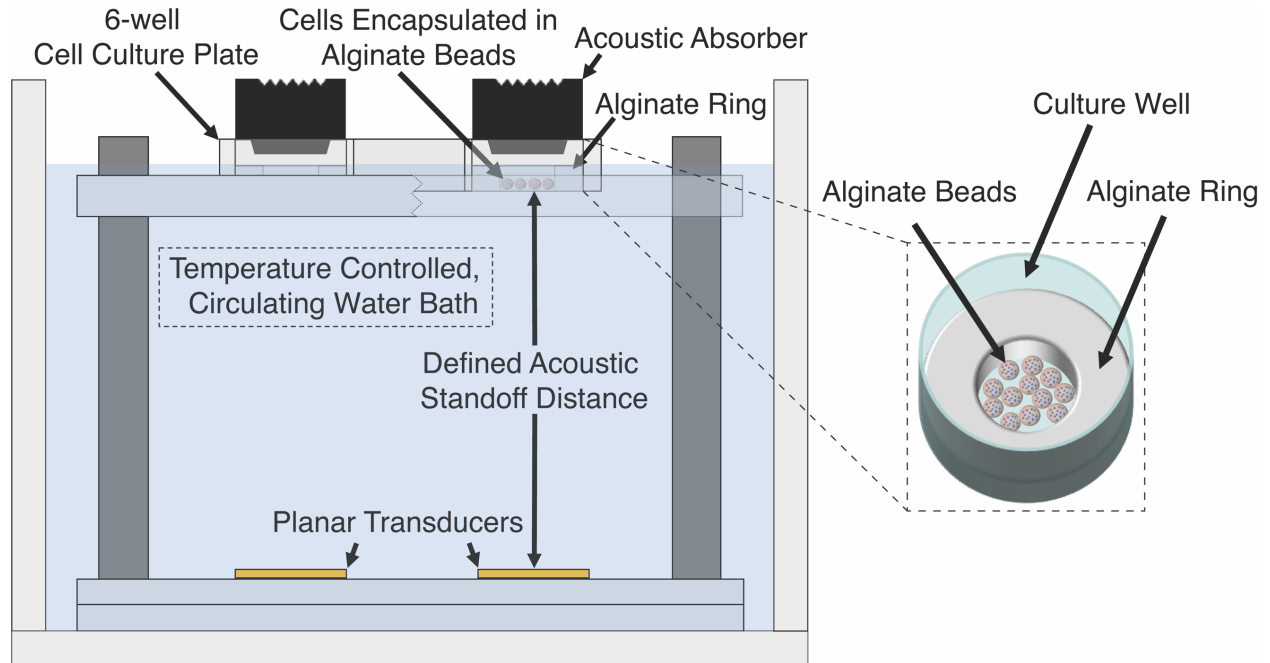
Figure 3.1 Generalized schematic representing the *in-vitro* LIPUS exposimetry system
The system was designed to deliver uniform acoustic energy to cells cultured in monolayer or 3D scaffolds and to adapt to a frequency range from 0.5 to 1.5 MHz. Two planar, PZT transducers were directed toward the center of two opposing corner wells of a standard cell culture plate. Cell culture targets were placed at a defined acoustic standoff distance and within an acoustically transparent alginate ring spacer to center the cells and reduce exposure to sidewall acoustic reflections. Wells were sealed distally with an acoustic absorber coupled to the media. The system was placed in a degassed, temperature-controlled water bath during exposures.

3.2.1.3 Design of Acoustic Absorber

Acoustic absorbers were designed to be in direct contact with the top surface of the media as a means to absorb acoustic energy transmitted through the target and eliminate reflections and standing wave formation within the well. Six biocompatible silicone materials were evaluated based on measurements of acoustic attenuation and reflection due to acoustic impedance mismatch

from water **(Table 3.1)**. Each material was prepared according to manufacturer's instructions, degassed, poured into cylindrical molds (4.2 cm diameter) to create two samples of different thicknesses (1.32 ± 0.10 cm and 2.55 ± 0.07 cm), and allowed to cure at room temperature overnight. Density was determined by using mass measurements and volume calculations. A pulse-echo transmit and receive US transmission system was used to determine the attenuation coefficient, reflection amplitude, and speed of sound through each material [151]. The test system consisted of an ultrasonic pulser-receiver (500PR, Panametrics, Inc., Waltham, MA, USA), two opposed 5 MHz immersion transducers (U8517054, Olympus NDT Instruments, Milwaukie, OR, USA) for transmit and receive, respectively, separated by 10 cm. The received amplitude waveform was measured using an oscilloscope (AFG3022C, Tektronix, Inc., Beaverton, OR, USA). Samples of various thickness were placed on a thin mylar stage between the two transducers and positioned perpendicularly to the US beam. The speed of sound through each sample C_S [m/s] was calculated as:

$$C_S = \frac{Z_1 - Z_2}{\left(t_{s,1} - t_{s,2} - \frac{Z_2 - Z_1}{Cw}\right)}$$

where Z_1 and Z_2 are the respective sample thicknesses [m] of sample 1 and sample 2, $t_{s,1}$ and $t_{s,2}$ are the respective times [s] for the US signal to travel from the emitting transducer to receiving transducer, and C_w is the speed of sound [m/s] through water (1484 m/s at 22°C). The attenuation coefficient of each sample μ [dB/m] was calculated as:

$$\mu = \frac{\ln\left(\frac{A_{o,1}}{A_{o,2}}\right)}{Z_2 - Z_1}$$

where $A_{o,1}$ and $A_{o,2}$, are the respective peak-to-peak voltage amplitudes [V] measured from the pulse waveform, and Z_1 and Z_2 are the respective sample thicknesses [m]. Reflection amplitude was assessed by measuring the amplitude of the signal reflected back toward the emitting

transducer. For each parameter assessed, measurements were taken four times in various positions throughout the sample and are reported as average values **(Table 3.1)**.

A custom mold was designed to create an absorber with the following characteristics: (i) a truncated-cone geometry (35.5 mm diameter x 8 mm depth; 25.4 mm total thickness) to allow direct coupling with media as well as air flow and media escape when placed in a media-filled well; and (ii) a ridged distal surface to baffle reflected waves, further increase absorption, and reduce re-transmission into the media. Mixed and degassed Sylgard 170 silicone (1696157, Dow Corning, Midland, MI, USA) was poured into a 3D-printed mold and cured by manufacturer's instruction. Pulse-echo measurements, similar to above, were performed to characterize the reflection amplitude of the final absorber design.

Table 3.1 Candidate absorber materials and associated acoustical properties.

Product Name	Density (g/cm^3)	Speed of Sound (m/s)	Attenuation Coefficient (dB/cm)	Reflection Amplitude (mVpp)
Smooth-On Mold Star[TM] 15 SLOW	12.36	1425.30	7.50	789.05
Smooth-On Mold Star[TM] 30	13.00	1428.60	6.70	859.40
Smooth-On Dragon Skin[TM]	6.71	1436.55	7.50	892.60
Smooth-On Ecoflex[TM]	10.78	1444.38	1.77	1038.95
Dow Sylgard® 170	8.27	1433.70	18.44	253.90
Momentive[TM] RTV60	8.47	1439.94	16.39	324.23

3.2.1.4 Characterization of US Beam Uniformity at Cell Culture Position

US intensity distributions directly inside CCP-wells was characterized for various configurations. The full LIPUS assembly was placed in a scan tank and hydrophone measurements were performed inside the well at 2 mm above the bottom of the CCP, representing the location of

the center of a 3D cell culture material. Six configurations were assessed, representing those commonly used for *in-vitro* LIPUS exposures [67, 85, 93, 96, 98, 100, 146, 152]: in the NF (no plate, 24-well CCP, and 6-well CCP) and in the FF (no plate, 24-well CCP, and 6-well CCP + alginate ring insert). Scan dimensions in the x-y plane were limited for some configurations due to narrow well diameter. As a quantitative measure of acoustic uniformity across the well area, the mean gradient magnitude was calculated using the numerical gradient function in the MATLAB Image Processing Toolbox (MATLAB Release 2016b, The MathWorks, Inc., Natick, Massachusetts, USA). The gradient vector magnitude was computed by the summation of the absolute value of the gradient vectors in the x and y dimensions.

3.2.1.5 Measurement of Temperature Elevation

Temperature elevation within the well and absorber was evaluated during LIPUS exposure. Copper-constantan thermocouples (Size 0.002in, California Fine Wire Company, Grover Beach, CA, USA) were fabricated and calibrated in-house and connected to a Data Acquisition/Switch Unit and Thermometry Modules (Model HP34970A, Keysight Technologies, Santa Rosa, CA, USA) set to one reading per second. Target wells contained a custom alginate ring and 10 alginate beads (3D cell culture scaffold material), all submerged in cell culture media (Dulbecco's modified Eagle's medium, Gibco; Invitrogen Inc., Carlsbad, CA, USA) which formed a liquid column inside the well. The acoustic absorber was partially submerged in the well as designed, coupling directly with the media while avoiding bubble formation. Multiple thermocouple probes were passed through the absorber and positioned parallel to the direction of US propagation in three different locations: centered and in contact with the well bottom, inside an alginate bead, and inside (2 mm from the bottom surface) the acoustic absorber. The full LIPUS assembly was submerged in a tank with water conditioned as described above and maintained at 37°C. The top of the exposure system

was covered with plastic sheeting to minimize heat and water vapor escape and to maintain temperature uniformity throughout the apparatus. LIPUS sonication was performed using the following parameters: 1.5 MHz operating frequency, 200 µs pulse, 1 kHz pulse repetition frequency, and I_{SPTA}=120 mW/cm^2. After a short baseline measurement, the LIPUS was switched on for 20-minute sonication followed by a cooldown back to steady-state. Measurements of temperature rise were repeated three times for each setup.

3.2.2 Biological Validation of LIPUS System

The FF LIPUS system described above, operating at 1.5 MHz, was used to apply pulsed US *in-vitro* to IVD cells which were then assessed for induced biological response. Bovine IVD cells were encapsulated in 3D alginate scaffolds and cultured in 6-well CCPs. Samples were randomly assigned to the nontreated control, growth factor treatment (BMP-7) as a positive control, or LIPUS treatment group. After 14 days in culture, extracellular matrix accumulation within the alginate scaffold was evaluated by hydroxyproline assay for total collagen content.

3.2.2.1 Cell Culture

IVDs were harvested from 18 to 24-month old bovine tails (Marin Sun Farms Inc., Petaluma, CA, USA) and annulus fibrosus (AF) cells were extracted and expanded as previously described [153], then encapsulated in alginate beads. Alginate hydrogels are widely used as an encapsulation method in a variety of *in-vitro* applications, including chondrocyte [154, 155], fibroblast [156], and IVD [85, 111, 157-159] cell culture, and have been used in several LIPUS studies involving IVD cells [67, 85, 121, 123]. The alginate bead culture system has many advantages over other hydrogel systems for IVD cell culture. AF cells cultured in alginate have been shown to maintain phenotypic stability [20, 160]. An additional advantage is that unlike many other hydrogels, alginate can be rapidly solubilized by calcium-chelating agents, allowing retrieval

of viable cells while removing trace elements of the hydrogel material [160, 161]. Further, culturing samples in several beads rather than a single disc is advantageous as it facilitates the randomization of samples for various outcome assays following treatment. Extracted AF cells were suspended in 1.2 wt% sodium alginate (FMC BioPolymer) in D-PBS at a density of $4x10^6$ cells/mL. Beads of approximately 25 µL in volume were formed by dispensing the solution dropwise through a 22-gauge needle into a reservoir of 102 mM $CaCl_2$ crosslinking solution. The beads were allowed to crosslink at room temperature for 10 minutes before washing with PBS and cell culture media. Twelve alginate beads (one sample) were cultured in two opposing corner wells of a CCP with 3 mL of Standard Disc Media (low-glucose DMEM with 5% FBS, 1% antibiotic/antimycotic, 1% nonessential amino acids, and 1.5% osmolarity salt solution containing 5 M NaCl and 0.4 M KCl). To avoid US exposure in neighboring, non-sonicated wells [98], each sample was cultured in opposing corner-wells, and control samples were not cultured in the same plate. Cells were kept in a 37°C, 5% CO_2 incubator and allowed to acclimate for 24-hours before initial treatment.

3.2.2.2 Evaluation of LIPUS Exposure

Twelve samples were divided among three groups: (1) nontreated control, (2) BMP-7 treatment, and (3) LIPUS treatment. The BMP-7 treatment group received Standard Disc Media supplemented with 200 ng/mL of Human Bone Morphogenetic Protein-7 (BMP-7) (Z02751, GenScript, Piscataway, NJ, USA). BMP-7 solution was exchanged on each treatment day. The LIPUS group was exposed to an US waveform (1.5 MHz operating frequency, 200 µs pulse, 1kHz pulse repetition frequency, I_{SPTA}=120 mW/cm^2) for 20 minutes each treatment day. When the CCP was placed on its platform, care was taken to remove air bubbles from and allow water to fill the crevices in the corners of the plate to allow proper coupling. To simulate environmental conditions

without LIPUS, control and BMP-7-treated samples were placed in the LIPUS exposimetry system for 20 minutes with the US turned off. All samples were cultured for 14 total days, with LIPUS exposure taking place on 8 of the 14 days. Media was changed on each day of treatment or every other day.

3.2.2.3 Quantification of Collagen Concentration

After 14 days of culture, the alginate beads were dissolved in 55 mM sodium citrate. Samples were concentrated by lyophilization for 2 total hours at a minimum of 75°C. Concentrated pellets were then dissolved in 40 µL of 6 N HCl for 16 hours at 110°C. The solution was centrifuged, and the supernatant was collected and neutralized. Total collagen content was quantified using acid hydrolysis followed by addition of p-dimethylaminobenzaldehyde and chloramine T (Sigma). DNA content was assayed with the Quant-iT PicoGreen dsDNA Assay Kit (P11496, Thermo Fisher, Waltham, MA, USA) and measured on a microplate reader (Spectramax M5, Molecular Devices, Sunnyvale, CA, USA) with 488 nm excitation and 525 nm absorption. Total collagen levels were normalized by the amount of total DNA to accommodate for differences in proliferation among treated and control samples.

3.2.2.4 Quantification of Glycosaminoglycan Concentration

After alginate beads were dissolved in 55 mM sodium citrate, the supernatant was digested in papain (P3125, Sigma-Aldrich, St. Louis, MO, USA) at 60°C overnight. Sulfated glycosaminoglycan (sGAG) content was quantified using the dimethylmethylene blue (DMMB) assay, with modifications for measuring alginate encapsulated samples [162], and normalized by DNA content as measured by PicoGreen assay.

3.2.2.5 Statistical Analysis

Statistical significance of differences in intensity gradient was evaluated using a one-way analysis of variance (ANOVA) test, followed by multiple t-tests with a Tukey HSD correction. Statistical significance of differences in collagen concentration was evaluated using the Kruskal-Wallis ANOVA test, followed by nonparametric comparisons for each pair using the Wilcoxon method. P-values < 0.05 were considered significant.

3.3 Results

3.3.1 Transducer and Acoustic Field Characterization

Analysis of acoustic field simulations suggested that 25 mm-diameter transducers would provide a practical selection for 0.5, 1.0, and 1.5 MHz operating frequencies. Predicted acoustic standoff distances of 125, 250, and 350 mm would yield 107.3%, 97.5%, and 82.9% coverage of the effective cell culture area within the FWHM for 0.5, 1.0, and 1.5 MHz operating frequencies, respectively **(Table 3.2 and Figure 3.2)**. Hydrophone measurements of the acoustic field distributions from fabricated transducers at these standoff distances **(Figure 3.2 B, E, H)** yielded 133.23%, 104.7%, and 98.7% coverage, respectively over 1.91 cm^2 area, demonstrating the feasibility of delivering broad, FF acoustic energy covering greater than 80% of the effective cell culture area.

Table 3.2 Summary of acoustic field metrics from simulations of various configurations
FWHM and % Area Covered was calculated for each offset distance. Only configurations that covered greater than 80% of a 24-well plate well bottom were considered to meet the design criteria; therefore, 25 mm diameter transducers and offset distances of 350, 250, and 125 mm were chosen for 1.5, 1.0, and 0.5 MHz frequency configurations, respectively. [a] Distance from the center of the transducer face to the center of the measurement plane. [b] Percentage of the surface area of a 24-well cell culture plate well bottom covered by the FWHM ultrasound beam (surface area of 24-well plate well bottom = 1.91 cm^2).

Operating Frequency (MHz)	Transducer Diameter [a] (mm)	Offset Distance (mm)	FWHM at Offset (mm)	%Area Covered [b]
1.5	20	225	14.0	80.5
	25	300	12.2	61.2
	25	350	14.2	82.9
	30	300	10.3	43.6
	35	300	9.3	35.5
1.0	20	175	14.0	80.5
	20	200	16.0	105.2
	25	225	14.0	80.5
	25	250	15.4	97.5
	20	300	19.2	75.5
	30	275	15.0	92.5
	30	400	20.0	81.9
	35	375	16.0	105.2
0.5	25	120	14.6	87.8
	25	125	16.2	107.3

1.5MHz **1.0MHz**

0.5MHz
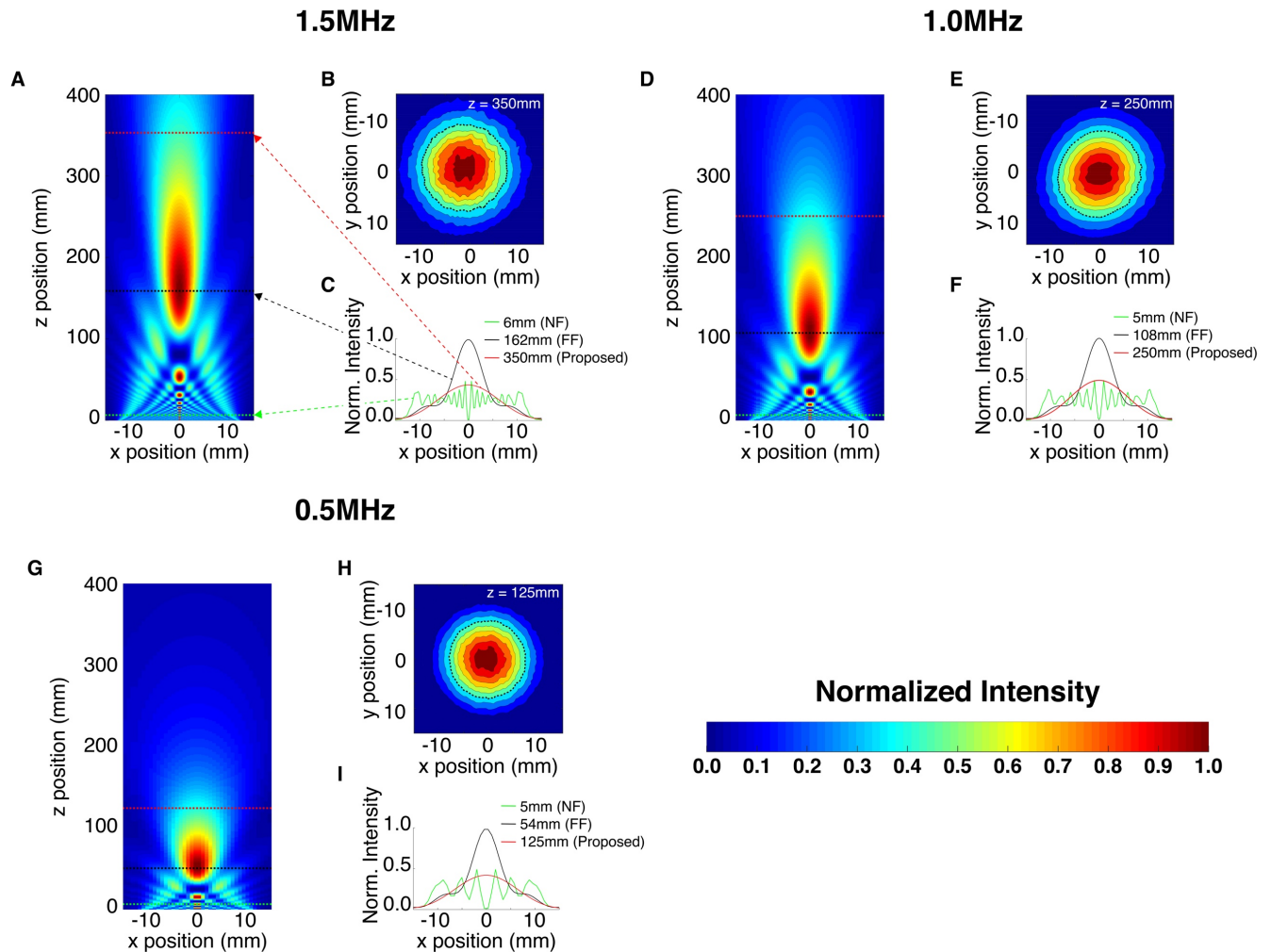
Figure 3.2 Simulated and measured acoustic fields
Axial simulations (A, D, G) demonstrated a heterogeneous near-field and a more uniform far-field region for each frequency as well as an expected reduction in focal depth with reduced frequency. Transverse line traces of these simulations (C, F, I) further highlighted differences in intensity distribution with depth in the acoustic field. Arrows indicate the location at which each line trace was taken within the simulated acoustic field. Multiple peaks were observed in the near-field, a uniform but narrow distribution at the focus, and a uniform and broad distribution past the focus. The latter was chosen for the LIPUS configuration and cross-sectional intensity measurements (B, E, H) were taken at the proposed depth via hydrophone scanning. The region within the dotted line is ≥ 50% of the maximum intensity and represents the location where the cellular target was placed.

3.3.2 Evaluation of Acoustic Absorber

Sylgard 170, a biocompatible silicone [163], demonstrated the greatest attenuation coefficient (18.4 dB/cm) with minimal reflection from the surface at less than 5% **(Table 3.1)**. Absorber efficacy, as evaluated by pulse-echo measurements, demonstrated the elimination of

reflections back toward the well-bottom, thereby minimizing the generation of standing waves within CCP wells. The reflection amplitude was reduced by 99.1% with the absorber in position (3.375 Vpp vs 0.031 Vpp).

3.3.3 US-beam Uniformity at Cell Culture Position

Surface plots of normalized intensity **(Figure 3.3)** qualitatively demonstrate the heterogeneity of the beam profile in the NF compared to the more uniform profile in the FF. In addition, it is apparent that the introduction of a narrow-diameter 24-well CCP in the beam path increases the heterogeneity in both the NF and FF configurations. When replaced with a wide-diameter 6-well CCP, the intensity distribution is less uniform than with no plate, but more uniform than with the narrow-diameter 24-well CCP.

Quantitative measurements of uniformity for the FF configurations, as shown in **Figure 3.4**, demonstrated an 80.3 – 86.4% reduction in mean gradient magnitude and reduced standard deviation in gradient magnitude by 78.9 – 93.7% when compared to corresponding NF configurations. The FF configuration including an alginate ring placed within a 6-well CCP **(Figure 3.3F)** demonstrated a 60.1% reduction in mean gradient magnitude compared to the configuration with a 24-well CCP in at the same position **(Figure 3.3E)** (0.10 ± 0.06 W/cm^2/mm vs 0.26 ± 0.16 W/cm^2/mm) and is similar to the no-plate configuration **(Figure 3.3D)** (0.08 ± 0.02 W/cm^2/mm vs 0.10 ± 0.06 W/cm^2/mm).
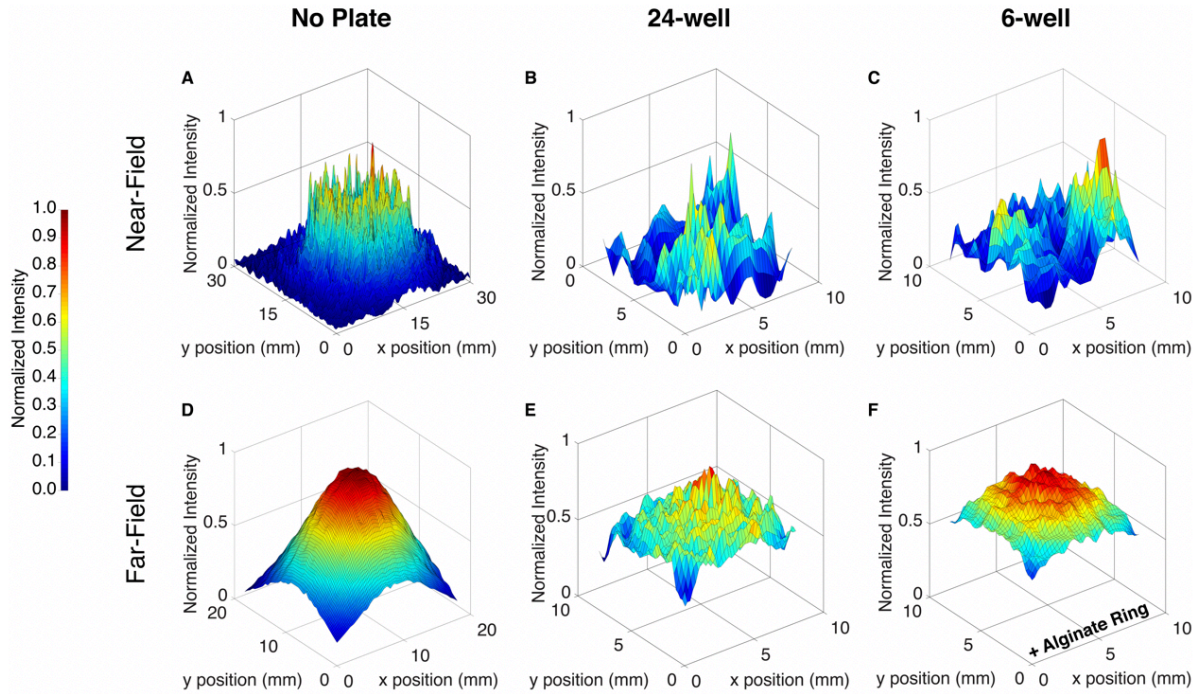
Figure 3.3 Surface plots depicting normalized intensity distributions
Intensity distributions were measured via hydrophone scanning at the sample location (2 mm above the well bottom) in various commonly used *in-vitro* LIPUS configurations (A-E) and the custom configuration (F). Overall, the intensity distribution within the near-field (5 mm offset) (A-C) was extremely heterogeneous compared to the far-field (350 mm offset) (D-F). For both regions, there was more heterogeneity with a narrow-diameter 24-well plate compared to a wide-diameter 6-well plate. The custom configuration (F), which included an alginate ring inserted in a 6-well plate, had the most uniform intensity distribution compared to all other configurations that included a well-plate. Note that the plot for the far-field, 24-well plate setup has a single narrow peak in intensity gradient due to well-wall reflections, increasing the heterogeneity of its intensity field.
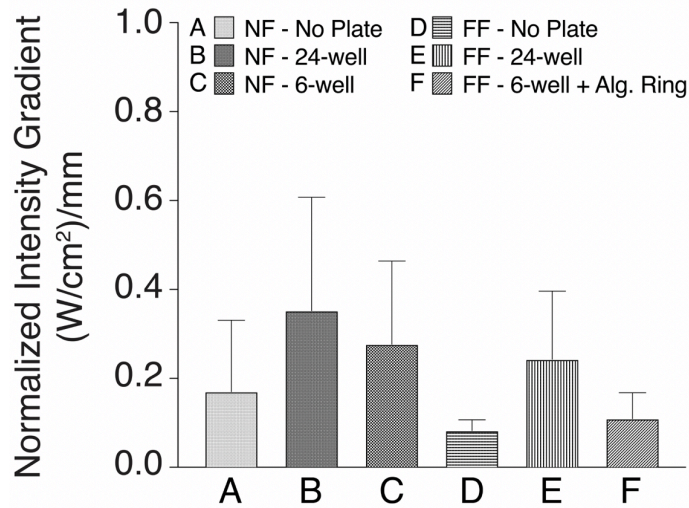
Figure 3.4 Quantification of acoustic field uniformity
Acoustic field uniformity was quantified by measuring the intensity gradient and normalizing by the maximum value for each group. The intensity gradient of the custom *in-vitro* LIPUS configuration (F) was significantly less than all other configurations that included a well-plate (B, C, E). The normalized intensity gradient of each group was significantly different from all other groups ($p < 0.05$). Error bars represent standard deviation of the intensity gradient.

3.3.4 Temperature Measurements

Temperature elevation measured within the well and absorber material during sonication at 1.5 MHz, demonstrated low temperature elevations within alginate beads of 0.81 ± 0.15°C, and 0.61 ± 0.31°C for the CCP-well bottom. Temperature rise was greatest within the acoustic absorber, with a temperature elevation of 2.32 ± 0.27°C.

3.3.5 Extracellular Matrix Deposition

LIPUS-induced bioactivity was evaluated and compared to BMP-7 exposure (as a positive control) by hydroxyproline assay for quantification of total collagen content and by DMMB assay for quantification of sGAG content. Exposure to both treatments had a profound effect on collagen concentration compared to nontreated controls **(Figure 3.5A),** with a 3.3-fold increase in the BMP-7 group (1.12 ± 0.55 µg/µg DNA vs 0.34 ± 0.07 µg/µg DNA, p = 0.03), and a 2.6-fold increase in the LIPUS group (0.89 ± 0.42 µg/µg DNA vs 0.34 ± 0.07 µg/µg DNA, p = 0.03). There was no

significant difference in collagen concentration between the BMP-7 and LIPUS treatment groups, (p = 0.47). sGAG concentration was increased, but there was no significant difference between the BMP-7 and control groups (7.91 ± 4.23 µg/µg DNA vs 5.03 ± 1.26 µg/µg DNA, p = 0.77) nor the LIPUS and control groups (8.60 ± 9.41 µg/µg DNA vs 5.03 ± 1.26 µg/µg DNA, p = 0.68) **(Figure 3.5B)**.
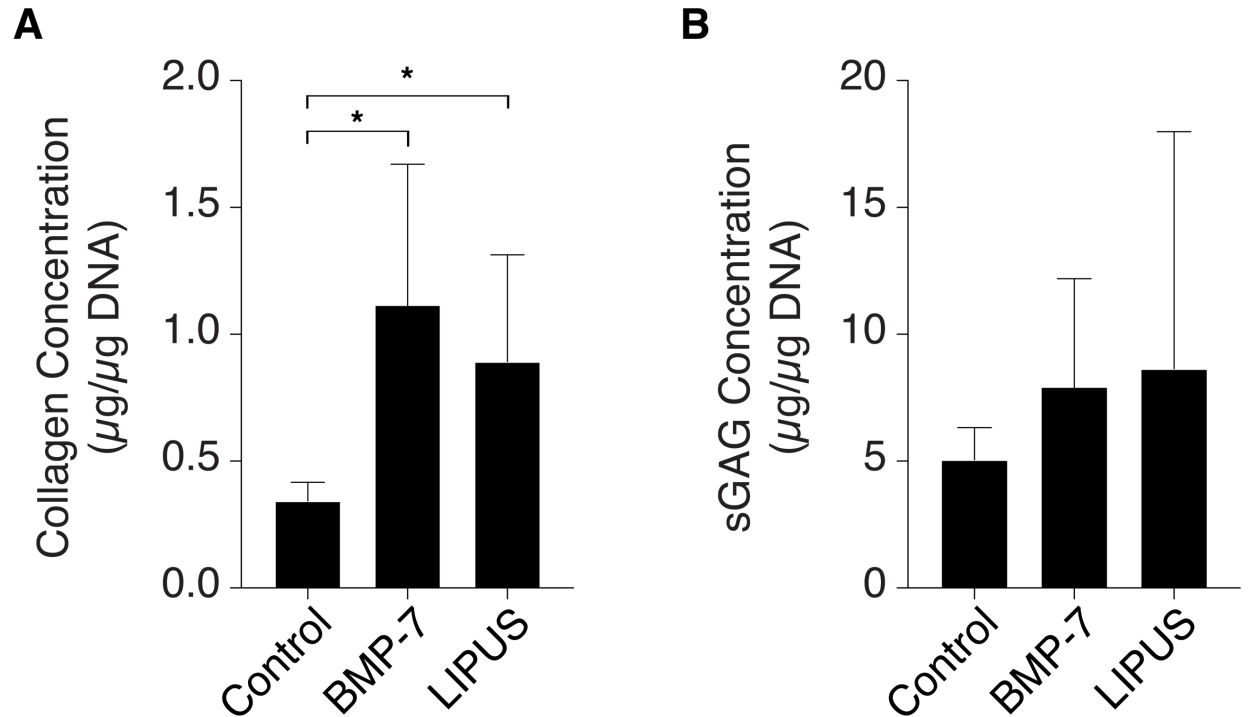
Figure 3.5 Quantification of extracellular matrix deposition
LIPUS and BMP-7 growth factor treatment upregulated collagen concentration by a similar magnitude and were both significantly greater than the nontreated control group (* $p < 0.05$) (A). sGAG concentration was increased, but not significantly upregulated by LIPUS nor BMP-7 treatment (B). Both collagen and sGAG concentration were calculated as the sum of total collagen or sGAG content normalized by total DNA content in alginate beads. Error bars represent standard deviation of the collagen and sGAG concentration.

3.4 Discussion

In this study, we investigated design parameters for an *in-vitro* LIPUS exposimetry system to deliver uniform FF acoustic energy to a distal target while mitigating several common acoustic artifacts. We identified the proper combination of transducer dimensions, and acoustic standoff

distance for various low frequency (0.5 – 1.5 MHz) sources to deliver broad, uniform US energy to a target sample area within a CCP well. This configuration, combined with an optimized absorber and alginate ring design, enabled delivery of 50% prescribed I_{SATA} across the target region within the CCP well. Using the final design, we treated bovine IVD cells over the course of several days then measured collagen content and found that FF LIPUS exposure upregulates collagen production in IVD cells comparable to BMP-7 growth factor treatment.

Typically, *in-vitro* LIPUS systems include cells cultured in polystyrene CCPs placed directly above a planar transducer [67, 85]. When comparing intensity distributions at various axial distances, we observed extremely heterogeneous intensity fields directly above the transducer and a more uniform field at the transducer's natural focus (i.e. FF transition). However, the intensity distribution at this location manifests as a narrow peak with a FWHM intensity of < 8.5 mm for each transducer frequency considered. At further distances within the FF, the intensity field demonstrated broader peaks, with a 2-fold increase in FWHM intensity. These data suggested that uniform, broad exposure can be achieved at positions past the focus, within the diverging FF.

The presence of standing waves originating at the liquid-air interface of *in-vitro* US exposure systems can increase the pressure amplitude at the cell culture position by up to 2-fold, or decrease by up to 50%, which leads to uncertainty in the exposure conditions and could either significantly reduce cell viability or considerably reduce the expected therapeutic dose, resulting in a less predictable therapeutic effect [94, 164]. By addition of the custom absorber, the formation of standing waves within the CCP well would be negligible. Since the total energy delivered to the target can vary widely due to standing waves, eliminating them is essential for the success of future parametric studies.

Initial acoustic field simulations and hydrophone measurements gave insight into the acoustic intensity field devoid of obstruction; however, as previously mentioned, cells are typically cultured within the confinement of a CCP well. Therefore, a more relevant analysis requires assessing the intensity field just beyond CCP-well bottom where the cells are located. By calculating the intensity gradient within this region, we have quantified the uniformity of the acoustic intensity field at the cell culture position within various common *in-vitro* configurations and demonstrated that adaptations to these configurations can greatly reduce beam heterogeneity in terms of intensity gradient magnitude. We found that the configuration with a 24-well CCP placed in the NF had the greatest intensity gradient, suggesting that cells treated using this configuration are particularly susceptible to heterogeneous mechanical stimulation and heating throughout the sample. Previous studies have suggested that differences in bioeffects may be explained by the local heterogeneity in the intensity distribution when exposing cells within the transducer's NF [146]. The FF configuration with an alginate ring inside a 6-well CCP had the lowest intensity gradient. This finding aligns with previous literature which hypothesized that the use of a well larger than the diameter of the transducer would reduce heterogeneity by minimizing reflections from well-walls [94]. The addition of an acoustically transparent alginate ring constrains the cells within a region outside the influence of the well-wall reflections believed to contribute the heterogeneity in narrow-welled configurations.

It is well accepted that exposure to US-energy has a therapeutic effect on several musculoskeletal tissues; however, the common presence of uncontrolled, US-induced heating of the CCP-plastic (by attenuation as well as heat transfer through direct contact with the transducer), and subsequently the sample, suggests that the mechanism of these effects may not be exclusively due to mechanical effects. Previous studies have shown that temperature elevation greater than

3°C is enough to induce bioeffects on cell cultures and can be reached even when delivering low intensities (e.g. $I_{SATA} = 32$ mW/cm^2) [98, 145, 165]. US-induced temperature elevation within the cell culture media as well as the well-walls and bottom of a CCP has been investigated for monolayer cultures [98, 166]; however, those observations may not be relevant for understanding heating effects on cells encapsulated in 3D-constructs such as sodium alginate beads. In the LIPUS system developed herein, which included a circulating water bath and acoustic absorber, we observed negligible average temperature elevations of < 1.0 °C within the alginate beads and CCP-well bottom, which is appreciably less than the temperature elevations previously reported in direct-contact systems [98] and demonstrates the ability to remove confounding temperature effects in LIPUS *in-vitro* studies.

For validation, bovine AF cells were exposed to LIPUS using the FF exposimetry system. Results demonstrated that collagen production was significantly greater than the control group when treated with BMP-7 (3.3-fold) or LIPUS (2.6-fold); however, there was no significant difference between LIPUS treatment and BMP-7 treatment. The findings demonstrate that uniform, FF LIPUS exposure, while eliminating significant temperature elevation and standing waves, can promote increased extracellular matrix production in bovine IVD cells *in-vitro* at a magnitude similar to that of growth factor treatment. This increase in collagen content with LIPUS treatment aligns with previous studies which have demonstrated a 1.3-fold increase in total collagen in human annulus fibrosus cells [40] and fibroblast cells treated with LIPUS in the NF [156]. Our preliminary gene expression data suggest that both LIPUS and BMP-7 treatment regulate collagen I and II expression in AF cells at similar magnitudes. These results align with previous work [40, 167] and suggest that LIPUS may stimulate the production of major fibrillar collagens of the IVD, which are important for maintaining its structural integrity. Although this

study has not differentiated between ratios of collagen I and collagen II levels for LIPUS and BMP-7, this could be further investigated in future studies to optimize LIPUS exposure levels by immunohistostaining or western blot analysis.

Overall, the results indicate that uniform, FF acoustic energy fields can be delivered to 3D cellular constructs cultured in standard CCP-wells and enclosed by an alginate ring spacer at frequencies at and below 1.5 MHz with negligible heating. Additionally, we demonstrate that FF LIPUS exposure increases collagen content in IVD cells, suggesting that LIPUS may be a potential therapeutic for stimulating repair of tissues deep within the body such as the IVD. Further investigations are needed to elucidate the effect of varying LIPUS dose parameters on the cell response and to optimize the benefits of LIPUS treatment in an IVD-tissue repair context.

3.5 Acknowledgments

4 Design of Experiments Screening of Low-intensity Pulsed Ultrasound Parameters for Modulating Matrix Gene Expression in Annulus Fibrosus Cells

The content of this chapter will be included as part of a research article that will be submitted to *Ultrasound in Medicine and Biology* in June 2020 by the following authors:

Devante A. Horne, Chris J. Diederich, Jeffrey C. Lotz

4.1 Introduction

Damage and tears in the intervertebral disc (IVD) are associated with pain and disability and are related to risk of disc herniation and degeneration [168]. Current therapies for stimulating healing, such as intradiscal growth factor and stem cell injections are invasive, are invasive and have shown limited success rates [65]. New technologies for treating damaged discs are increasingly focused on the regeneration and repair of the annulus fibrosus (AF) [40].

Among the various therapeutic modalities being explored, low-intensity pulsed ultrasound (LIPUS) has been shown to stimulate several musculoskeletal cell types to increase proliferation and extracellular matrix (ECM) synthesis [169]. LIPUS is well known for its use in stimulating bone healing and has shown bioeffects in soft tissues as well, including the nucleus pulposus [121, 123] and AF [40, 170]. LIPUS has advantages over other potential therapies including the capability of delivering acoustic energy extracorporeally to target tissues of interest while sparing healthy tissues along the way. Our group has recently shown that LIPUS energy in the far-field can significantly upregulate collagen accumulation in AF cell cultures [170].

While LIPUS has been established as a promising therapeutic for bone repair, progress has been limited for other tissues such as the IVD, likely due to a lack of an established dose-response relationships. Many previous studies have focused on established LIPUS parameters: 1.5 MHz operating frequency, 1 kHz pulse repetition frequency (PRF), 30 mW/cm^2 spatial and temporal

averaged intensity, and 20 min treatment duration. These settings have been proven effective for bone healing [78, 81, 171]; however, LIPUS parameters have not been fully optimized for soft tissues such as the IVD. Limited parametric studies have suggested significant dose-dependent LIPUS effects, including increased proteoglycan synthesis in AF cells treated with higher intensities and for more days [67, 85, 100, 123], increased calcium accretion in stem cells with increasing pulse repetition frequency [93], and increased proteoglycan and collagen synthesis in stem cells treated for longer durations [100]. Nonetheless, with the lack of a comprehensive evaluation of LIPUS parameters, there is no clear understanding of which parameters are most important for stimulating extracellular matrix (ECM) synthesis in AF cells, nor which parameter combination is most effective for stimulating a desired therapeutic effect. A better understanding of the effect of varying LIPUS parameters on cell phenotypes may allow patient and condition-specific dosing.

LIPUS parameter effects have generally been studied *in-vitro* by varying only one factor at a time (OFAT). The comprehensive application of this approach would require the evaluation of all possible combinations to achieve an optimal response. However, independent variables do not always act in isolation, and interaction effects can significantly influence the response; therefore, it can be difficult to make an informed decision on the best factor settings when evaluated OFAT as this method is incapable of identifying interactions between factors and moreover, it is very costly in terms of time and resources.

Design of Experiments (DOE) is a statistical technique used to plan experiments and analyze data. The DOE method involves the design and use of a controlled set of tests to model and examine the relationships between factors and responses and is a tool for optimizing responses in a small number of experiments while also identifying any interactions among factors. DOE can

significantly improve the efficiency of factor screening and optimization and has been used successfully in various industries including biotherapeutics [172-175]. There are many advantages of the DOE method over the more traditional OFAT approach to factor exploration and optimization. With DOE, experimental factors are varied simultaneously, allowing the identification of factors affecting the response with the minimum number of experiments through nonlinear multivariate data analysis and prediction modeling. With a significantly reduced experimental matrix, factor optimization can be achieved while conserving time and cost.

The DOE workflow is typically comprised of multiple phases including identification, screening, model validation, and optimization. The initial identification phase involves the collation of a list of factors expected to influence the response of interest. The screening phase involves experimentation to identify the main effect of the factors on the response as well as significant interaction effects of a factor on other factors, with the primary aim of reducing the number of factors to a smaller subset of those that have the most significantly impact on the response metric. In the screening phase, a DOE matrix is designed that ideally covers the entire experimental range by applying each factor at their maximum and minimum levels. DOE screening experiments typically use a Full-Factorial design, or Plackett-Burman design to build a first-order model of the response [174] and to generate a polynomial prediction formula. The accuracy of model predictions is evaluated by comparing model-predicted values to actual experimental responses. Optimal conditions for individual responses are determined by the construction and numerical optimization of a desirability function to find a factor settings that maximize desirability. When multiple responses are to be optimized, all goals can be combined into an overall desirability function.

While LIPUS has been shown to stimulate ECM expression in AF cells, the relative significance and optimal combination of LIPUS factors on ECM gene expression in AF cells is largely unknown. Consequently, we sought to investigate the effects of LIPUS parameters on ECM gene expression in AF cells to improve our understanding of the underlying dose-response relationships. We hypothesized that the ECM gene expression in AF cells can be regulated by varying LIPUS parameter settings.

4.2   Methods

4.2.1   DOE Matrix

An experimental matrix was generated using the DOE Screening Design platform of JMP (JMP® Pro 14.3.0). Three factors of interest were identified, including peak intensity (mW), PRF (kHz), and treatment duration (min), along with their corresponding value at each level **(Table 4.1).** Four responses were specified, including gene expression of Matrix Metalloproteinase-1 (MMP1), Matrix Metalloproteinase-13 (MMP13), Interleukin-6 (IL6), and Collagen Type I Alpha I (COL1), along with their corresponding goal **(Table 4.2)**. A 2^k full-factorial experimental design was constructed where all factors were held at one of two discrete levels (high or low) during each run of the experiment. The experimental design included all possible combinations of factor settings and allowed for modeling all 2-factor interactions with only 8 runs for 3 factors identified **(Table 4.3).**

Table 4.1 LIPUS factors and levels for DOE
The full-factorial design space was defined by 3 LIPUS parameters varied at 2 levels. Samples were treated once using a LIPUS system operating at 1.5 MHz. The waveform duty cycle was maintained at 20% during application of both low and high PRF levels by adjusting the burst count proportionally.

Factors	Low	High
Peak Intensity (mW)	300	1200
PRF (kHz)	0.1	1.0
Treatment Duration (min)	5	20
Operating Frequency (MHz)	Fixed at 1.5	
Number of Treatments	Fixed at 1	

Table 4.2 Gene expression responses for DOE
Relative expression levels of 4 ECM genes were assessed for each sample. The desired goal for each response was indicated for optimization.

Response (FC Gene Expression)	Goal
MMP1	Minimize
MMP13	Minimize
IL6	Minimize
COL1	Maximize

Table 4.3 Experimental matrix for screening design
The 3-factor, full-factorial design consisted of 8 total experimental conditions with 3 replicates each.

LIPUS ID	Peak Intensity (mW)	PRF (kHz)	Duration (min)
1	1200	1	20
2	300	1	20
3	1200	1	5
4	300	1	5
5	1200	0.1	20
6	300	0.1	20
7	1200	0.1	5
8	300	0.1	5

4.2.2 Cell Culture

IVDs were harvested from 18 to 24-month old bovine tails (Marin Sun Farms Inc., Petaluma, CA, USA) and AF cells were extracted and expanded as previously described [153]. AF cells (passage 3) were seeded in two opposing corner wells of each tissue culture treated 6-well microplate (353046, Corning Incorporated, NY, USA) at a density of $0.5x10^6$ cells/well. Cells were pre-cultured with 3 mL of standard disc media (low-glucose, phenol-free DMEM with 5% FBS, 1% antibiotic/antimycotic, 1% nonessential amino acids, and 1.5% osmolarity salt solution containing 5 M NaCl and 0.4 M KCl) in a 37°C, 5% CO_2 incubator for 24 hours before treatment.

4.2.3 LIPUS Exposure

Samples were divided into 10 groups with 3 replicates each (n = 30): (1) nontreated control, (2) IL-1α treatment, and (3 - 10) IL-1α + LIPUS treatment at 8 different parameter settings **(Table 4.3)**. At least two hours prior to LIPUS exposure, medium was exchanged for either fresh standard disc media or inflammatory media (standard disc media with 10ng/mL of IL-1α (12778,

Sigma-Aldrich, St. Louis, MO, USA)) to simulate normal and inflammatory disc environments. Samples were placed in a far-field LIPUS exposimetry system **(Figure 4.1)**, as described previously [170], and exposed to LIPUS at settings defined by the DOE matrix **(Table 4.3)**. To simulate environmental conditions without LIPUS, nontreated control and IL-1α-treated samples were placed in the LIPUS exposimetry system with the ultrasound turned off.
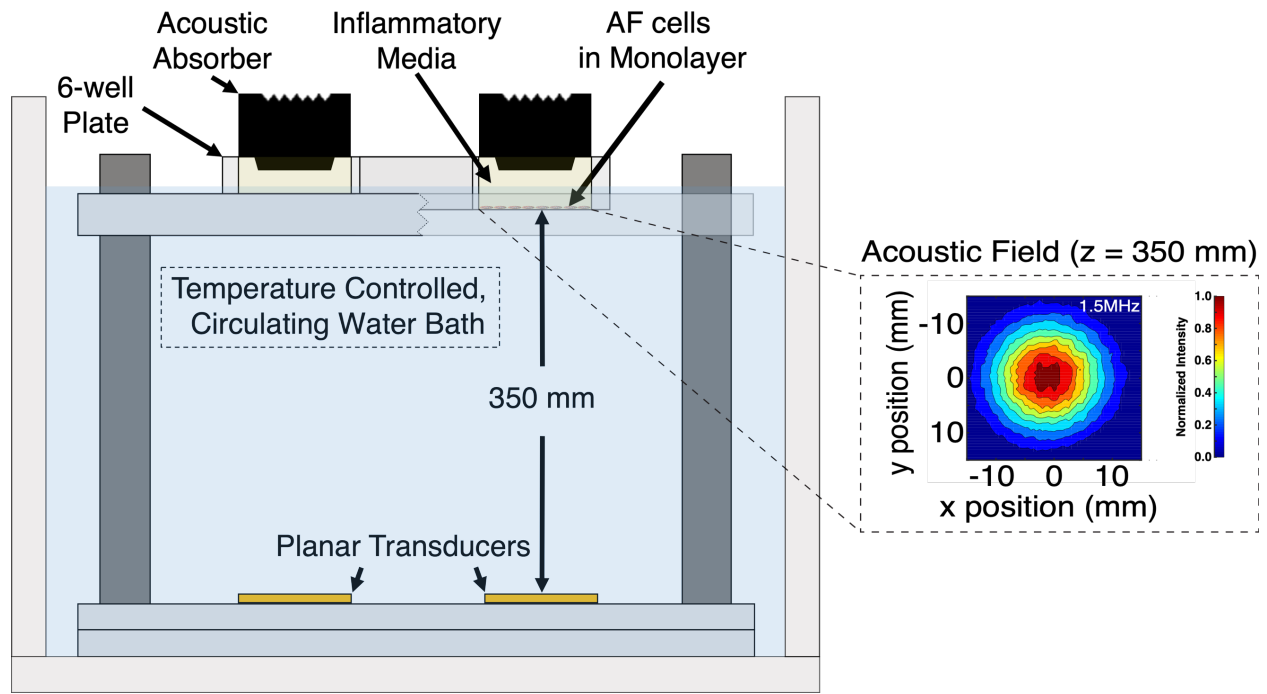
Figure 4.1 Schematic representing the *in-vitro* LIPUS far-field exposimetry system
Two planar transducers operating at 1.5 MHz delivered acoustic energy to cells cultured in monolayer at a 350 mm standoff placing samples in the uniform acoustic far-field. Target wells were sealed with an acoustic absorber coupled to the cell culture medium. The system was placed in a degassed, temperature-controlled water bath during exposure. A representative plot of the normalized acoustic intensity field at the cell location (inset) demonstrates uniform intensity distribution.

4.2.4   Gene Expression Analysis

ECM gene expression was assessed one day after LIPUS exposure. AF cells were lysed directly in the cell culture well using 150 µL of PicoPure RNA extraction buffer. Then, total RNA was isolated and purified using the PicoPure RNA Isolation Kit (Arcturus, Mountain View, CA,

USA) according to manufacturer's instructions. cDNA was transcribed using the iScript™ Reverse Transcription Supermix (1708841, Bio-Rad Laboratories, Hercules, CA, USA). RT-qPCR was performed using TaqMan Universal PCR Master Mix (4444557, Applied Biosystems, Foster City, CA, USA) and TaqMan primers and probe sets for MMP1, MMP13, IL6, and COL1. The B2M mRNA gene was co-amplified as an internal standard. Relative expression levels were calculated using the ΔΔCt method [176], normalizing first to B2M then to the expression level measured in the IL-1α treatment group, and expressed as fold-change (FC) values. The FC data were then compiled and recorded in the respective response column of the DOE worksheet for analysis. Statistical differences in FC gene expression among the LIPUS conditions was evaluated using a one-way analysis of variance (ANOVA) test, followed by multiple t-tests with a Tukey HSD correction for differences between conditions. P-values < 0.05 were considered significant.

4.2.5   DOE Analysis

4.2.5.1   Two-level Screening and Model Reduction

DOE screening analysis to investigate the main effects and interactions among LIPUS parameters (factors) and FC gene expression (responses) was performed in JMP. Two-level effect screening was performed for model reduction and to make inferences about factor effects by identifying factors which have the largest effect on each response. The Fit Two-level Screening platform in JMP takes the variation across the response values and evaluates the relationship with the effects in the factor space. The significance of factor effects, or the difference in the mean response between two levels of a factor, were evaluated by an F-test. Statistically significant ($p < 0.10$) factors and interactions were identified for each response, and a final model was generated with the exclusion of non-significant factors.

4.2.5.2 Fitting and Evaluating Linear Regression Models

A standard least squares fit was used to construct the final model, with model effects designated as first- and second-degree (interaction) effects only. A model was generated for each of the 4 responses. Each model was evaluated for goodness-of-fit by ANOVA, and a Whole Model Actual by Predicted Plot was generated.

Estimated coefficients of the regression equation were generated for each response, and the significance of each model term were evaluated by t-test; p-values < 0.05 were considered significant. To reduce collinearity in the model, interaction terms were centered by subtracting the mean of each value in the corresponding column of the DOE matrix. Matrices of interaction plots were created to visualize the interaction effects in the model of each response.

4.2.5.3 Validation of DOE-predicted Responses

Validation experiments were preformed using identical cell-culture and LIPUS-exposure methods as those described herein. Inflammatory AF-cell samples (n = 3) were treated once with LIPUS at parameter settings previously used by our group: 600 mW peak intensity, 1 kHz PRF, and 20 min duration [170]. Gene expression was analyzed by qPCR, and mean FC values were computed using the same methods described herein. DOE models were used to predict mean FC values and 95% confidence intervals for each response at these factor settings. To test the validity of model predictions, DOE-predicted FC values were compared against the actual FC values and the percentage difference was calculated.

4.2.6 Response Optimization

Optimization was performed in JMP using desirability functions, where desirability was defined according to the corresponding goal of each response **(Table 4.2)**. The optimum factor settings within the design space and corresponding response value were predicted for each

individual response. The overall optimum factor settings (i.e. maximum desirability for all genes) were predicted using an overall desirability function, defined as the geometric mean of the desirability function of the individual responses [177].

4.3   Results

4.3.1   Gene Expression Analysis

The effect of LIPUS exposure on AF cells cultured in an inflammatory environment was evaluated by measuring the FC expression of catabolic genes (MMP1 and MMP13), a pro-inflammatory gene (IL6), and an ECM synthesis gene (COL1). The addition of 10 ng/mL IL-1α to the cell culture media significantly upregulated MMP1 ($p < 0.0001$), MMP13 ($p < 0.0001$), and IL6 ($p < 0.0001$) expression compared to the control **(Figure 4.2)**. However, IL-1α treatment did not significantly affect COL1 expression compared to the control ($p = 0.9996$).

MMP1 expression was significantly downregulated compared to the IL-1α treatment group when exposed to LIPUS ID 1-5 ($p < 0.05$) but not 6-8 ($p = 0.0509$, 0.6970, and 0.0878, respectively). MMP13 expression was significantly downregulated when exposed to LIPUS ID 1-6 ($p < 0.05$) but not 7 nor 8 ($p = 0.6654$ and 0.5480, respectively). IL6 gene expression was significantly downregulated when exposed to LIPUS ID 1-5 and 8 ($p < 0.05$), but not 6 nor 7 ($p = 0.1258$ and 0.5855, respectively). For COL1 expression, there were no significant differences among groups ($p = 0.9305$).
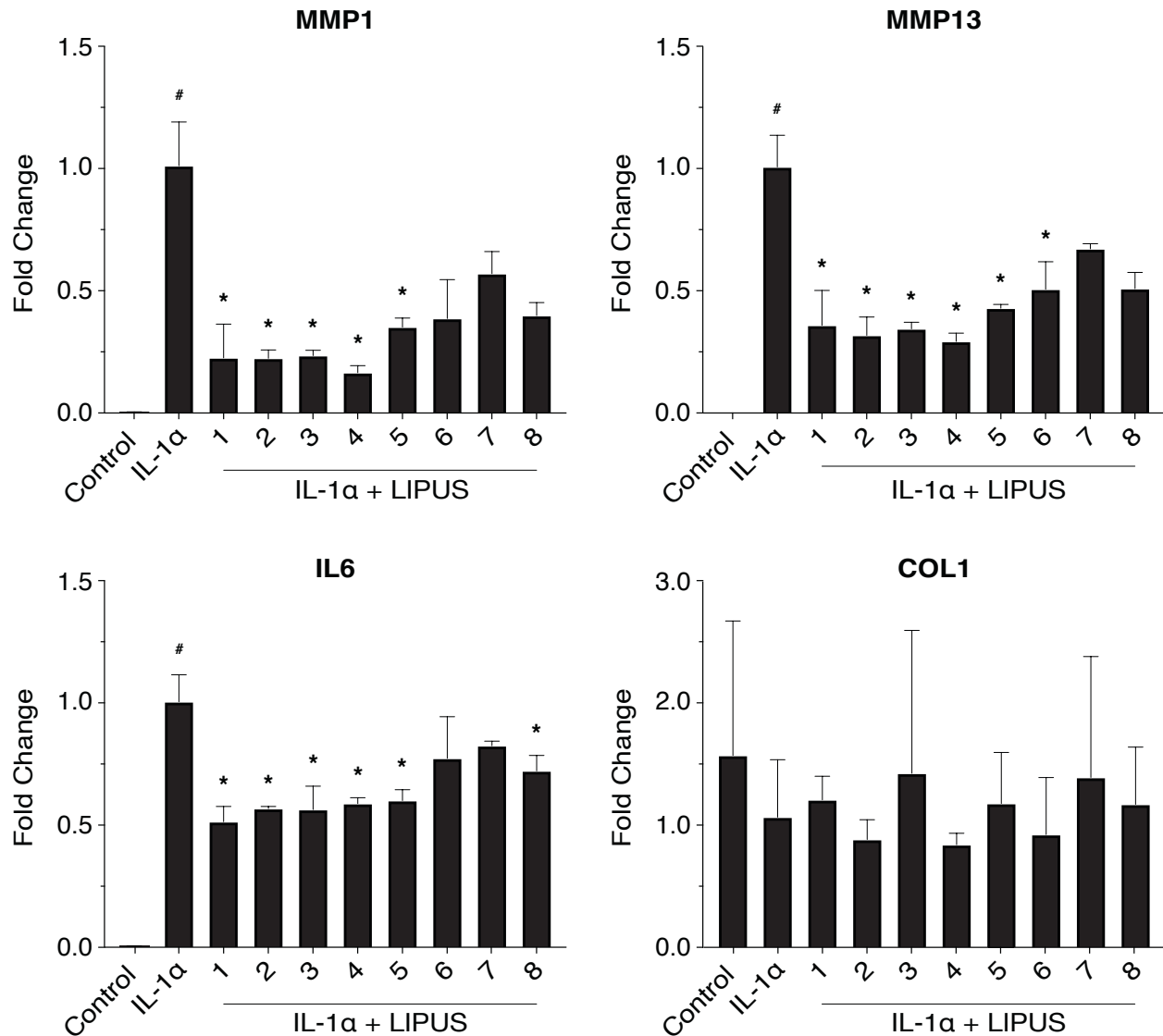
Figure 4.2 Gene expression results demonstrate range of responses within design space
IL-1α treatment upregulated catabolic and pro-inflammatory gene expression (# $p < 0.0001$). LIPUS exposure at several parameter settings downregulated catabolic and pro-inflammatory gene expression in cells cultured in inflammatory medium (* $p < 0.05$). Neither IL-1α nor LIPUS exposure significantly regulated COL1 expression.

4.3.2 Effect Screening

Two-level screening was used for model reduction by identifying about main effects and interaction effects for each response. The effect chart **(Figure 4.3)** shows the relative effect magnitude and direction for each response; effects extending beyond the reference line were considered significant ($p < 0.10$). Three factors significantly affected MMP1 expression: the main

effect of PRF ($p = 0.0010$), and the interaction effects of PRF*Duration ($p = 0.0873$) and Peak Intensity*Duration ($p = 0.0917$). A single factor significantly affected MMP13 expression: the main effect of PRF ($p = 0.0020$). Two factors significantly affected IL6 expression: the main effect of PRF ($p = 0.0036$), and the interaction effect of Duration*Peak Intensity ($p = 0.0761$). Peak intensity was the only factor that significantly affected COL1 expression ($p = 0.0647$).

Gene	Factor	Effect	Relative Effect	p-value
MMP1	PRF (kHz)	-0.107		0.0010
	PRF (kHz)*Duration (min)	0.035		0.0873
	Peak Intensity (mW)*Duration (min)	-0.034		0.0917
	Peak Intensity (mW)	0.026		0.1863
	Duration (min)	-0.023		0.2451
	PRF (kHz)*Peak Intensity (mW)	-0.008		0.6969
MMP13	PRF (kHz)	-0.100		0.0020
	PRF (kHz)*Duration (min)	0.036		0.1203
	Duration (min)*Peak Intensity (mW)	-0.031		0.1653
	Duration (min)	-0.026		0.2423
	Peak Intensity (mW)	0.022		0.3088
	PRF (kHz)*Peak Intensity (mW)	0.001		0.9722
IL6	PRF (kHz)	-0.086		0.0036
	Duration (min)*Peak Intensity (mW)	-0.038		0.0761
	Duration (min)	-0.030		0.1428
	Peak Intensity (mW)	-0.019		0.3532
	PRF (kHz)*Duration (min)	0.013		0.5494
	PRF (kHz)*Peak Intensity (mW)	-0.001		0.9568
COL1	Peak Intensity (mW)	0.173		0.0647
	Duration (min)	-0.079		0.3559
	Peak Intensity (mW)*PRF (kHz)	0.054		0.5626
	PRF (kHz)	-0.038		0.6786
	Duration (min)*PRF (kHz)	0.036		0.6981
	Peak Intensity (mW)*Duration (min)	-0.028		0.7606

Figure 4.3 Two-level screening effect chart
Main and interaction effects for each response were identified by two-level screening analysis for subsequent model reduction. Effect values were on the same scale as the corresponding response. Horizontal bars indicate relative effect, where effects extending beyond the red vertical lines indicate a significant effect ($p < 0.10$). Shaded rows indicate significant factors that were included in the final models.

4.3.3 Evaluation of Prediction Models

4.3.3.1 Goodness-of-fit

Linear least squares regression models were generated for each response, excluding non-significant factors identified by two-level effect screening **(Figure 4.3)**. Goodness-of-fit was evaluated by ANOVA and visualized by plotting actual experimental results against model predicted values for each response **(Figure 4.4)**. The model-predicted values were significantly correlated with experimental values for MMP1 ($R^2 = 0.68$, $p < 0.0001$), MMP13 ($R^2 = 0.56$, $p < 0.0001$), and IL6 ($R^2 = 0.58$, $p = 0.0001$); however, COL1 model-predicted values were not significantly correlated with experimental values ($R^2 = 0.10$, $p = 0.1309$).
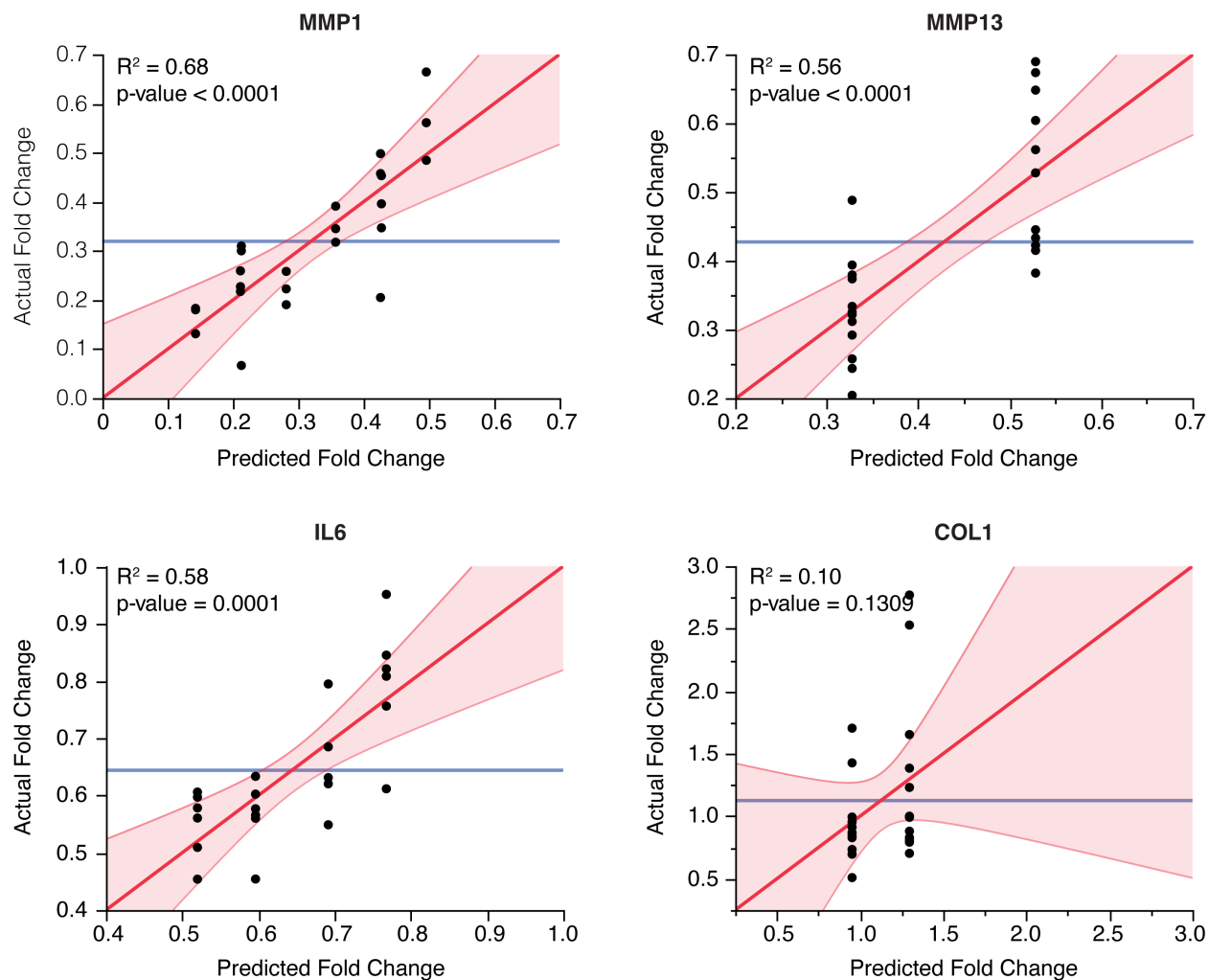
Figure 4.4 Whole model actual by predicted leverage plots
Goodness-of-fit for the final model of each response was evaluated to determine significance. Shaded region indicates 95% confidence interval. Confidence curves which cross the blue horizontal line (mean response) were considered significant. Models for MMP1, MMP13, and IL6 were significant ($p < 0.05$). The model of COL1 was not significant.

4.3.3.2 Regression Equations

The reduced models were used to generate a regression equation for each response. Estimates of term coefficients inform the relative magnitude and direction of term effects **(Table 4.4)**. The main effect of PRF was significant, and negatively correlated with MMP1, MMP13, and IL6 expression ($p < 0.0001$), indicating that higher PRF is better for decreasing MMP1, MMP13, and IL6 expression compared to lower PRF. The main effect of Peak Intensity was positively correlated with COL1 expression but was not significant ($p = 0.1309$).

Table 4.4 Tabulated regression equations
Significant effects and interactions were included as terms in the final model of each response. Estimated regression coefficients indicate the relative effect size and direction. Model terms with p-values < 0.05 were considered significant.

Gene	Term	Coefficient	t Ratio	Prob>|t|
MMP1	Intercept	0.450	15.867	<0.0001*
	PRF	-0.238	-5.966	<0.0001*
	(PRF-0.55)*(Duration-12.5)	0.010	1.950	0.0654
	(Peak Intensity-750)*(Duration-12.5)	-0.001e-2	-1.911	0.0704
MMP13	Intercept	0.550	18.20	<0.0001*
	PRF	-0.223	-5.24	<0.0001*
IL6	Intercept	0.750	27.01	<0.0001*
	PRF	-0.191	-4.89	<0.0001*
	(Duration-12.5)*(Peak Intensity-750)	-1.13e-5	-2.17	0.0415*
COL1	Intercept	0.838	3.92	0.0007*
	Peak Intensity	0.038e-2	1.57	0.1309

4.3.3.3 Interactions Between Factors

However, for MMP1 and IL6, main effects do not fully describe the relationship between factor and response due to the presence of factor interactions. Interaction plots **(Figure 4.5)** show the two-factor interaction profiles for MMP1 and IL6 expression, where parallel lines indicate no interaction and intersecting lines indicate factor interactions. Two interaction terms were identified in the model of MMP1 expression: PRF*Duration and Peak Intensity*Duration. Interaction plots indicate that the effect of PRF was sensitive to treatment duration: high PRF with low duration demonstrated reduced MMP1 expression compared to the same PRF with high duration. Moreover, the steeper slope of the line for low duration suggests that PRF had a greater effect on MMP1 expression when duration was low; however, this interaction was not statistically significant ($p = 0.0654$). The effect of peak intensity was also sensitive to treatment duration, where high peak intensity with high duration further reduced MMP1 expression compared to the same peak intensity with low duration. Additionally, the peak intensity was negatively correlated with MMP1 expression when duration was high but was positively correlated when duration was

low; however, this interaction was also not statistically significant ($p = 0.0704$). In the model of

IL6 expression, duration significantly interacted with peak intensity ($p = 0.0415$). Low treatment

duration with high peak intensity demonstrated reduced IL6 expression compared to the same

duration with low peak intensity. Furthermore, treatment duration was negatively correlated with

IL6 expression when peak intensity was high but was positively correlated when peak intensity

was low.
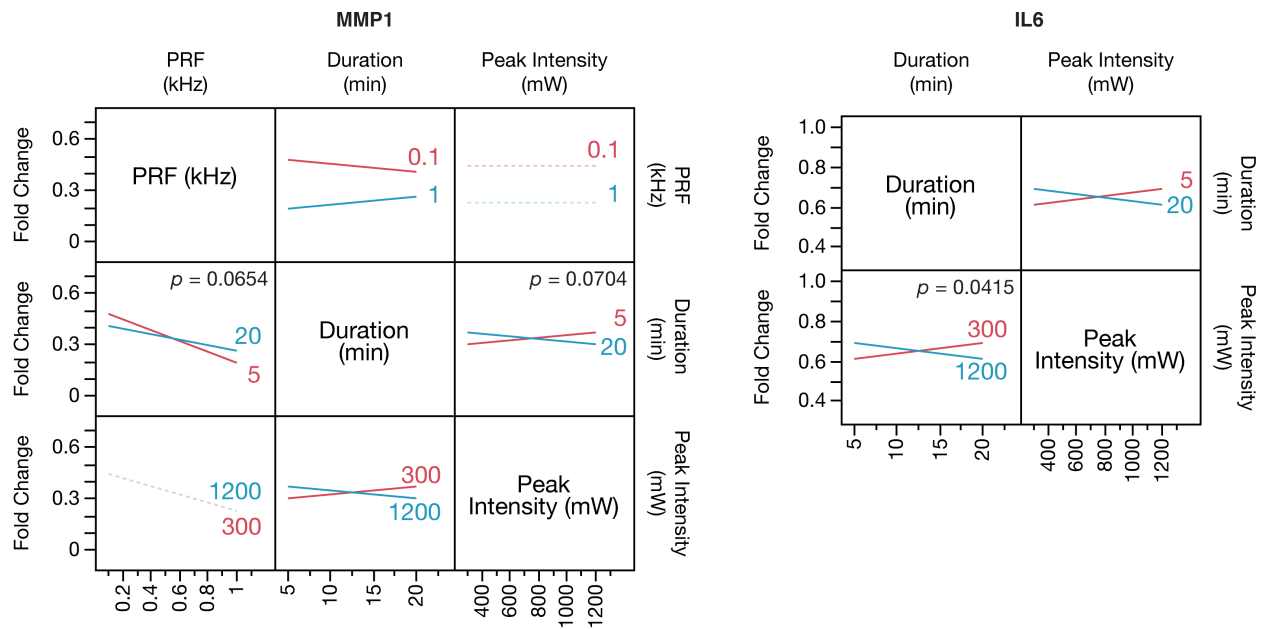
Figure 4.5 Factor interaction profiles
Interaction plots show the interaction of the row effect with the column effect. Non-parallel lines suggest possible interactions, and the slope magnitude of the line segment indicates the effect size of the interaction. Interactions with *p*-values < 0.05 were considered significant in the final model. Dashed line segments are alias terms which were not included in the model.

4.3.4   Validation of DOE-predicted Responses

Validation experiments used LIPUS parameter settings that lay within the design space:

600 mW peak intensity, 1 kHz PRF, and 20 min duration. Response values from these experiments

were compared to DOE-predicted responses **(Figure 4.6)**. The DOE-predicted mean and 95%

confidence limits for MMP1 were 0.259 ± 0.066. The predicted mean was 86% different the actual

mean FC of 0.647 ± 0.269. The DOE-predicted MMP13 expression was 0.327 ± 0.056, which was

66% different from the actual mean FC of 0.647 ± 0.308. The DOE-predicted IL6 expression was 0.571 ± 0.053, which was 12% different from the actual mean FC of 0.647 ± 0.269. The DOE-predicted COL1 expression was 1.068 ± 0.240, which was 17% different from the actual mean FC of 0.894 ± 0.438.
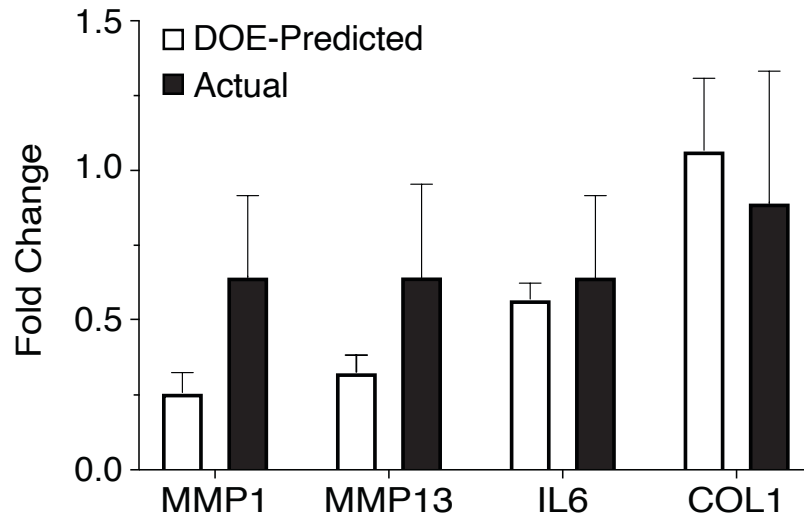
Figure 4.6 DOE-predicted and actual gene expression responses
DOE models were used to predict changes in ECM gene expression in response to LIPUS exposure at 600 mW peak intensity, 1 kHz PRF, and 20 min duration. To test the validity of DOE predictions, they were compared to actual experimental data. Bars represent mean FC and error bars represent the 95% confidence interval.

4.3.5 Response Optimization

Optimum LIPUS parameters were identified for each response individually **(Table 4.5)** using desirability functions and overall **(Table 4.6)** by the geometric mean of the individual desirability functions. The predicted optimal LIPUS parameter settings for minimizing MMP1 and IL6 expression were identical: 300 mW peak intensity, 1 kHz PRF, and 5 min treatment duration. The estimated mean reduction in MMP1 and IL6 expression compared to the IL-1α treatment group was 86% and 48%, respectively. The optimal setting for minimizing MMP13 expression was predicted to include 1 kHz PRF and result in an estimated mean reduction in MMP13 expression of 67% compared to the IL-1α treatment group. The optimal setting for maximizing

COL1 expression was predicted to include 1200 mW peak intensity and result in an estimated

mean increase in COL1 expression of 30% compared to the IL-1α treatment group. The optimal

settings for maximizing desirably for all gene expression responses was predicted to be 300 mW

peak intensity, 1 kHz PRF, and 5 min treatment duration.

Table 4.5 Predicted optimal factor settings for individual gene expression response
Predicted optimal settings were determined individually for each response using desirability
functions. Predicted mean fold-change values and 95% confidence intervals (CI) were determined
for each response at the corresponding predicted optimal setting.

Gene	Peak Intensity (mW)	PRF (kHz)	Duration (min)	Fold Change	Lower CI	Upper CI
MMP1	300	1	5	0.143	0.068	0.218
MMP13	-	1	-	0.327	0.271	0.383
IL6	300	1	5	0.520	0.457	0.583
COL1	1200	-	-	1.298	0.975	1.620

Table 4.6 Predicted optimal factor settings for overall gene expression responses
Predicted overall optimal setting for maximizing desirability for all responses. Corresponding
predicted mean fold-change values and 95% confidence intervals were determined for each
response at the predicted optimal setting.

Gene	Peak Intensity (mW)	PRF (kHz)	Duration (min)	Fold Change	Lower CI	Upper CI
MMP1				0.117	0.035	0.199
MMP13	300	1	5	0.238	0.159	0.316
IL6				0.526	0.443	0.608
COL1				0.850	0.300	1.400

4.4   Discussion

In this study, we investigated the effects of LIPUS peak intensity, PRF, and treatment

duration, simultaneously, on ECM gene expression in AF cells using DOE. We exposed AF cells

under inflammatory conditions to LIPUS at settings defined by a 2^k full-factorial DOE matrix. FC

gene expression responses were assessed by qPCR, significant factors and interactions for each

gene expression response were identified by effect screening DOE, and significant factors and

interactions were included in a least-squares regression model of each response. The resulting

models were used to further explore main effects and interactions, and to predict LIPUS settings for optimizing each response. We found that LIPUS exposure significantly downregulated MMP1, MMP13, and IL6 gene expression in AF cells cultured in inflammatory media but did not significantly affect COL1 gene expression. The main effect of PRF was the most significant factor for modulating MMP1, MMP13, and IL6 expression, while peak intensity was most significant for modulating COL1 expression. Additionally, we found that treatment duration interacted with both peak intensity and PRF to regulate MMP1 and with peak intensity to regulate IL6 expression. Finally, validation experiments demonstrated that DOE-predicted responses were 12 - 86% different from actual responses.

PRF was a significant factor for MMP1, MMP13, and IL6 expression and was the only significant main effect observed. When PRF level was adjusted from its high value to its low value, the burst count was increased proportionally such that the duty cycle remained at 20%. Nonetheless, applying LIPUS with a low PRF was less effective on average at reducing catabolic and pro-inflammatory gene expression compared to high PRF, across the levels of all other factors **(Figure 4.2)**. These results suggest ECM gene expression may be sensitive to pulsed waveform characteristics. Similar effects have been shown in previous studies by Marvel et al. (2010), which demonstrated increased calcium accretion in stem cells with increasing PRF [93]. Miller et al. (2017) demonstrated that adherent chondrocytes exposed to an ultrasound field experienced strain at the adhesion points, with membrane displacements on the order of 10-100 nm [178]. This mechanical deformation is sensed by localized cellular mechanoreceptors such as integrins and mechanosensitive ion channels and are transduced into biochemical outputs including downstream changes in gene expression. Zhang et al. (2016) showed that in degenerative human IVD cells, mechanical stimulation from LIPUS was detected by integrins, leading to focal adhesion formation

and ultimately enhanced ECM synthesis [121]. Mechanosensitive ion channels such as Piezo1 and Piezo2 may also play a crucial role in the transduction of repetitive mechanical stimuli. Piezo channels are thought to function as bandpass filters, preferentially transmitting stimuli in only a narrow frequency range. Lewis et al. (2017) found that transduction efficiencies varied by stimulus frequency, waveform, and duration [179]. In this context, the long pulse intervals of the low PRF groups may be less efficiently transduced by AF-cell piezo channels, resulting in a damped response.

LIPUS has been shown to modulate IVD-cell proteoglycan synthesis and collagen gene expression in an intensity-dependent manner [85, 123, 180]. Additionally, proteoglycan and collagen synthesis were increased in stem cells treated from longer durations [100]. This does not align with our finding that peak intensity and treatment duration were not significant factors for modulating ECM gene expression. However, by utilizing a DOE approach for effect screening, we found interactions between peak intensity and duration that influenced MMP1 and IL6 gene expression, as well as an interaction between PRF and duration that influenced MMP1 expression **(Figure 4.5)**. These interactions represent important findings that were quickly established using DOE but would not have been observed by utilizing the traditional OFAT approach.

Most of the previous literature investigating LIPUS bioeffects use waveform parameters originally established for bone fracture healing including 30 mW/cm^2 spatial and temporal averaged intensity, 1 kHz PRF, and 20 min treatment durations. While LIPUS exposure at these settings has been shown to induce ECM synthesis and anti-catabolic activity in degenerative IVD cells, it is unclear whether these are the optimal parameter settings for stimulating this activity in AF cells. Here, we used a regression model and desirability functions for MMP1, MMP13, IL6, and COL1 gene expression to predict the optimal LIPUS settings for maximizing desirable

expression of each gene individually. We found 300 mW peak intensity, 1 kHz PRF, and 5 min duration to be the optimal settings for minimizing MMP1 and IL6 gene expression, and 1 kHz PRF to minimize MMP13 expression at any peak intensity or treatment duration. We also found 1200 mW peak intensity to maximize COL1 gene expression at any PRF or treatment duration. We then sought to identify the overall optimal LIPUS parameter settings for maximizing desirable expression of all 4 genes. However, when optimizing for several responses together there were competing criteria. Since the importance, or weight, of each response was set to be equal, the overall optimal peak intensity favored the 3 genes which were minimized at 300 mW peak intensity, while resulting in a damped effect on COL1 expression **(Table 4.6)**. These findings highlight the potential benefit of identifying a LIPUS dose for each desired disease-modifying activity as choosing a single dose may result in dampening of some responses.

When constructing a DOE matrix, it is important to select a factor range that encompasses the entire applicable range for each factor, as this defines the design space for factor optimization. The factor ranges used in this study were selected based on previous literature and excluded higher intensities and treatment durations found to induce significant temperature elevations in our preliminary work. It is possible that the factor ranges chosen may not have included the actual optimum settings. However, results from this screening DOE inform the direction in which the current design space can be moved to approach the space where the optimal conditions can be found. We found that the model of COL1 expression was not significant, potentially due to a restricted design space. Future studies of COL1 modulation by LIPUS should include an expanded intensity range with consideration of potentially confounding thermal effects [145]. Expanding the peak intensity range may in turn broaden the effect range, improve the model fit, and ultimately increase the reliability of response predictions.

Validation experiments demonstrated variation in the accuracy of DOE predictions. While DOE predictions for IL6 and COL1 expression were within 17% of the actual values, predictions for MMP1 and MMP13 were 86% and 66% different, respectively, from actual values. This variation in accuracy suggests that our screening design may not have captured the complexity of the MMP1 and MMP13 gene expression response to LIPUS exposure. All 2^k factorial DOEs, including the screening design utilized in this study, rely on the assumption that the effects of the factors on the response are linear within the design space. This assumes there is no curvature and may cause the model to miss the effect and incorrectly screen out a factor. It is possible that the effect of peak intensity, PRF, or duration reached a peak or plateau between the high and low levels. Therefore, in future studies, center points should be included in the factorial DOE to test the assumption of linearity and improve the accuracy of response predictions and factor optimization.

While transducer operating frequency, number of treatments, and duty cycle were fixed in this study, their potential impact on AF-cell ECM gene expression warrant future study. Lower frequencies (0.5-1.0 MHz) are of interest as they are thought to be more relevant for penetrating to deep tissues such as the IVD. Moreover, cellular deformation and associated responses are thought to be frequency-dependent [178, 181]. Additionally, the number of LIPUS treatments has been consistently shown to influence ECM gene and protein expression in multiple cell types [85, 156, 182, 183]. Finally, exploring the effect of duty cycle may allow the decoupling of pulse duration from PRF, which may have been a confounded variable in this study.

We sought to investigate the effects of LIPUS parameters on ECM gene expression in inflammatory AF cells and hypothesized that ECM gene expression can be regulated by varying LIPUS exposure parameters. To test this hypothesis, a screening DOE was implemented. Overall,

the results suggest that the desired LIPUS modifying activity (i.e. anti-catabolism, anti-inflammation, or ECM synthesis) can be specified by adjusting LIPUS parameter settings. Additionally, we identified PRF as the most influential main effect, and that duration interacted with PRF and peak intensity to influence MMP1 and IL6 gene expression, a finding which can be attributed to the use of DOE as an alternative to traditional OFAT methods. DOE is a powerful tool for factor exploration and optimization in the area of process development and manufacturing; however, to our knowledge, DOE has not previously been applied to study the effects of LIPUS parameters on IVD cells. This paper illustrates the capability and benefits of implementing DOE in the context of therapeutic ultrasound optimization. The results of this study may translate in the future to clinically relevant effects in human IVDs and could inform the application of patient- and condition-specific dosing to directly correct the metabolic imbalance that is often the driver of progressive IVD degeneration.

5   Magnetic nanoparticles synergize with pulsed magnetic fields to stimulate osteogenesis in-vitro

The content of this chapter has been submitted as a research article to *Tissue Engineering: Part A* and is currently in review. The authors are as follows: Mohamed Habib*, Devante Horne*, Khalid Hussein, Dezba Coughlin,   Erik Waldorff, Nianli Zhang, James Ryaby, Jeffrey Lotz (*Equal Contribution)

5.1   Impact Statement

Novel approaches for stimulating new bone growth are necessary to overcome the challenge of delayed bone healing. In this study, we cultured mesenchymal stem cells with an iron-ion doped tri-calcium phosphate bone substitute (Fe-TCP) and exposed them to a pulsed electromagnetic field (PEMF) signal to investigate their effects on osteogenesis. We revealed the synergistic effects of Fe-TCP and PEMF and demonstrated that the combination of these technologies could provide a promising method for accelerating bone healing in a clinical setting.

5.2   Introduction

Delayed bone healing is a major challenge in orthopedic clinical practice, especially when treating patients with critical-size bone defects. For such indications, there is a need for technologies to overcome ineffective cell growth and osteogenic differentiation at the defect site [184, 185]. Recent strategies for enhanced bone healing include the development and application of new biomaterials [48, 153, 186, 187]. A novel aspect of new biomaterials is to utilize nanotechnology to incorporate trace elements within the construct [186]. Additionally, successful use of biomaterials for bone healing typically requires other technologies for construct stabilization and mechanical stimulation for optimal results [48, 153, 187, 188]. One such technical augmentation is the use of external magnetic fields [189, 190]. Beneficial synergism between

magnetic fields and biomaterials can occur by incorporating magnetic nanoparticles so as to modify the local stress environment, and thereby influence cellular activities, including proliferation and differentiation, by attaching to specific ion channels present on cellular membrane. Cells can thus be mechanically conditioned by remote magnetic actuation [190-192].

The most commonly used magnetic particles for biological applications are iron-ion based [193]. Iron oxide (Fe_3O_4) particles are known to be non-toxic and are eventually degraded *in-vivo* and incorporated into hemoglobin [194]. The mechanism of clinical effect is considered to be bone-cell adhesion, proliferation, and activation of mechano-transduction pathways [185, 190, 191]. There have been several attempts to incorporate magnetic properties and evaluate their effect on bone regeneration under external static magnetic field stimulation **(Table 5.1)**. In most of these studies, magnetite was used with hydroxyapatite (HA) [189, 190, 195, 196]. Alternative strategies include ion-doping of osteoconductive bioceramics [193, 197, 198], to develop magnetic nano-bone substitutes (MNBS) that are intrinsically magnetic. Among different MNBS, hydroxyapatite (HA) is most frequently ion-doped with iron [193, 195], which has been shown to be non-toxic while enhancing cellular proliferation when combined with static external magnetic fields [199].

Table 5.1 Summary of studies combining MNBS with external magnetic fields

Ref. Composition	Form	Production Method	Intrinsicality	Ms (emu/g)	External Mag. Field
[195] Magnetite/HA	Scaffold	Infiltration	No	0.94-0.24	Helmholtz coil 10 Oe / 50 Hz
[199] Magnetite/HA	Scaffold	Ball mixing/Foaming	No	34-53	MagnetoFACTOR-24 plate 320 mT
[196] Fe-HA	Powder	Ion doped	Yes	4.0-4.2	MagnetoFACTOR-24 plate 320 mT
[190] Magnetite/Collagen/HA	Scaffold	Infiltration/Nucleation	No	15-23	NdFeB magnet 1.2T
[189] Magnetite/HA/PLA	Scaffold	Electrospinning	No	0.049	NdFeB magnet 5-10T

While this combination of MNBS with external magnetic fields may be useful for bone regeneration, there are challenges with the translation of this strategy into routine clinical practice. These include determining the optimal combination of a controllable external magnetic field with the properly designed MNBS. Most of the previous studies have used static magnetic fields *in-vitro* [199, 200]. However, a dynamic, pulsed magnetic field has been shown to be superior for bone healing [187]. Consequently, we sought to investigate the synergistic effects of an FDA-approved Pulsed Electromagnetic Field (PEMF) signal with an Fe-ion doped tri-calcium phosphate bone substitute (Fe-TCP). We hypothesized that the osteogenic activity of standalone PEMF or MNBS will be significantly enhanced through their combined use.

5.3   Methods

5.3.1   Synthesis of Magnetic Nano Bone Substitute (MNBS)

Intrinsically magnetic Fe-ion doped tri-calcium phosphate (MNBS) were obtained by substituting Ca^{2+} with Fe^{3+} cations, while maintaining the Ca + Fe / P molar ratio equal to 1.5 via the wet chemical process. Calcium nitrate tetrahydrate $[Ca(NO_3)_2 \cdot 4H_2O]$ (Sigma Aldrich,

Germany), Di-ammonium hydrogen orthophosphate [$(NH_4)_2HPO_4$] (Sigma Aldrich, India) and

Iron (III)-chloride [$FeCl_3$] (Sigma Aldrich, India) were used as a source of calcium, phosphorus,

and iron ions, respectively. The pH of the solution was maintained at 9.5-10 by adding Ammonium

hydroxide [NH_4OH, ≤ 33% w/w] (EDWIC, Egypt) during the stirring of the reactant's mixture.

After the precipitation process, the solution was filtered, aged overnight, dried at 60°C for 24

hours, and finally calcined at 800°C for 2 hours. The MNBS were sterilized with 25kGy gamma

irradiation.

5.3.2 Characterization of MNBS

Phase composition of the MNBS were determined by X-ray diffraction (XRD) using AXS-

D8 Advance system (Bruker, Germany) equipped with a metal ceramic tube (Cu K-alpha

wavelength = 1.5405981 Å at 1600 W, 40 kV, 40 mA). The samples were scanned at diffraction

angles (2θ) between 20º and 60º with a step size of 0.02º 2θ per second.

Functional groups of the MNBS were identified by Fourier transform infrared (FTIR)

spectroscopy (FT-IR spectrometer 6100, JASCO, Japan), using KBr pellet technique in the range

4000–400 cm^{-1}, with a resolution of 8 cm^{-1}). The powder sample was mixed with KBr salt at a

concentration from 0.2% to 1%. The mixture was ground and then pressed into a small IR

transparent pellet.

The morphology of MNBS was studied by transmission electron microscopy (TEM)

(JEOL 1010, Japan) operated at 80 kV accelerating voltage. Powder samples were suspended in

ethanol at a concentration of 0.1 g/mL and ultrasonicated for 30 minutes to yield a homogeneous

suspension. Carbon coated grids were dipped in the suspension and dried prior to their placement

in a single tilt holder for TEM imaging.

Magnetic properties were evaluated using a vibrating sample magnetometer (VSM7410, Lakeshore, USA) with field from 0 to 25000 G (0 to 2.5 T) at room temperature to estimate the magnetic parameters of the material including remanent magnetization, coercitive force, and saturation magnetization.

5.3.3 Cell Culture

Human mesenchymal stem cells (hMSCs) (MSC-003, RoosterBio, Frederick, MD) were obtained from a single donor and expanded up to passage 2 using RoosterNourish™-MSC bioprocess media (KT-001, RoosterBio, Frederick, MD), which included RoosterBasal™-MSC media supplemented with 2% RoosterBooster™-MSC. Following expansion, hMSCs were cultured in MSC growth media (low-glucose, phenol-free DMEM with 10% FBS and 100U/mL Penicillin/Streptomycin). Medium was changed 3 times per week. Cells in all experimental groups were plated in monolayer at a seeding density of 2×10^4 cells/cm^2 in standard 12-well cell culture plates and cultured in a cell culture incubator (37°C, 5% CO_2). Cells were incubated for 24 hours to allow attachment before adding MNBS to respective wells. A MNBS solution was prepared by mixing MNBS with MSC growth media at a concentration of 0.2 mg/mL and sonicating to disaggregate particles before adding 2 mL of the solution to each well with adherent cells. Samples were then incubated for 24 hours to allow cells to interact with MNBS before PEMF treatment.

5.3.4 Cell-MNBS Interaction

Attachment and internalization of MNBS by hMSCs was assessed by both scanning electron microscopy (SEM) and transmission electron microscopy (TEM). For SEM, cells were seeded at a density of 2×10^4 cells/cm^2 on silicon wafer substrates (16008, TED Pella, Inc., Redding, CA, USA) placed in a 6-well cell culture plate well. For TEM, cells were seeded at a density of 2×10^4 cells/cm^2 on 35 mm glass-bottom dishes (P35G-1.5-14-C, MatTek Corp.,

Ashland, MA, USA). Cells were incubated for 24 hours to allow attachment before adding the MNBS solution as described above. Cell-MNBS samples were fixed on day 4 of culture. All samples were rinsed with media, then fixed in 2.5% glutaraldehyde/2.5% PFA in 0.1 M sodium cacodylate buffer at pH 7.4 (15949, EMS, Hatfield, PA, USA) and incubated at room temp for at least 30 minutes. Samples prepared for SEM were imaged using the Hitachi S-5000 Scanning Electron Microscope System. Samples prepared for TEM were imaged using the Tecnai 12 Transmission Electron Microscope.

5.3.5 PEMF Treatment

The PhysioStim® PEMF signal (Orthofix Medical Inc., Lewisville, TX) was used in this study. The signal consisted of a square wave with a 25% duty cycle, 3.85kHz pulse frequency, 15Hz burst frequency, and a slew rate of 10 T/s. The *in-vitro* PEMF exposure system was powered by a 16V direct current power source and consists of a coil surrounding a multi-level stage that was placed inside an incubator. Cell culture plates were placed on this stage and exposed to PEMF waveform for 4 hours daily. Non-treated control samples were also placed on the PEMF stage with the power turned off.

5.3.6 Cell Viability

Cell viability was evaluated using the LIVE/DEAD® Viability/Cytotoxicity Kit (L3224, Molecular Probes, Eugene, OR, USA) and was qualitatively assessed by manufacturer's instructions. Briefly, adherent cells were cultured with or without MNBS or PEMF treatment for up to 7 days. Cells were gently washed with PBS then stained with LIVE/DEAD reagent solution consisting of 2 μM Calcein-AM and 4μM EthD-1 in PBS. Samples were wrapped in aluminum foil and incubated at room temperature for 30 minutes. Following incubation, the glass slide with stained, adherent cells, was inverted and mounted on a microscope slide with 10 μL of

LIVE/DEAD reagent and sealed with fingernail polish. Labeled cells were imaged under a fluorescent microscope (DMi8, Leica, Germany). For quantitative analysis, fluorescence of control and experimental samples was measured using a microplate reader (Spectramax M5, Molecular Devices, Sunnyvale, CA, USA). The percentage of dead cells was calculated from the fluorescence readings as: $\frac{F(645)sample - F(645)min}{F(645)max - f(645)min}\ x\ 100\%$, where $F(645)_{sample}$ is the fluorescence reading at 645 nm in each experimental sample, $F(645)_{min}$ is the fluorescence reading at 645 nm in a sample where all the cells are dead and labeled with Calcein only, and $F(645)_{max}$ is the fluorescence reading at 645 nm in a sample where all the cells are dead and labeled with EthD-1 only.

5.3.7   DNA and Alkaline Phosphatase Quantification

Total ALP, including intracellular (cell lysate) and extracellular ALP (medium supernatant) was measured daily for 10 consecutive days with three biological replicates. Medium supernatant samples of 1 mL volume were collected at the time of harvest and with each medium change. Cells were harvested by incubating with 0.5% trypsin and subsequent scraping as needed to remove adhered cells from the culture plate. Cell samples were resuspended in FBS-containing medium and divided in half for either DNA or ALP-activity quantification. Alkaline phosphatase (ALP) activity was quantified using the ALP assay kit (ab83369, Abcam, Burlingame, CA, USA) according to the manufacturer's protocol. Briefly, cells were washed with PBS, resuspended in 50µL of assay buffer, then homogenized for one minute at 2.4 m/s using a Bead Ruptor 24 Bead Mill Homogenizer (19040E, Omni International, Kennesaw, GA, USA). Media and cell samples were plated in a clear, 96-well microwell plate and absorbance was measured on a microplate reader (Spectramax M5) at OD 405 nm. ALP activity was quantified by referencing a standard curve and normalized by DNA content. DNA content was quantified using the Quant-iT PicoGreen

dsDNA Assay Kit (P11496, Thermo Fisher, Waltham, MA, USA) and measured on a microplate reader (Spectramax M5) with 480 nm absorption and 520 nm excitation.

5.3.8 Alizarin Red Staining and Quantification

Medium was aspirated and the cells were fixed with 10% formalin for 10 minutes followed by washing with D-PBS twice. Calcium deposit was stained using 2% Alizarin Red S Staining Kit (0223, ScienCell Research Lab., Carlsbad, CA, USA). Dye was added to each sample and incubated at room temperature for 30 minutes before washing with D-PBS. Stained samples were visualized via brightfield microscope (Nikon Eclipse E800).

For quantification of Alizarin Red S (ARS) dye incorporation, the dye was extracted from the stained monolayer using cetylpyridinium the chloride (CPC) extraction method [201]. Briefly, 350 mg of CPC (6004-24-66, Sigma) were dissolved in 10 mL of ddH$_2$O to obtain a working solution, and 1 mL of the working solution was added to each well and incubated for 2 hours at 37°C before aspiration. The aspirated samples were transferred to a 96-well plate and absorbance was measured on a microplate reader at OD 405 nm. ARS content was calculated using an ARS standard curve.

5.3.9 Gene Expression Analysis

Gene expression levels of osteogenic markers were assessed on days 1, 4, and 7. To extract total RNA, cells were digested in TRIzol (15596018, Life Technologies, South San Francisco, USA) and homogenized using the Bead Ruptor as described above. RNA was isolated with two steps of chloroform extraction and purified with a RNeasy Mini Kit (74104, Qiagen, Redwood City, USA). cDNA was transcribed using the iScript cDNA Synthesis Kit (1708890, Bio-Rad, USA). RT-qPCR was performed using TaqMan Universal PCR Master Mix (4444557, Applied Biosystems, Foster City, CA, USA) and TaqMan primers and probe sets for osteopontin (SPP1),

bone morphogenetic protein-2 (BMP2), Alkaline Phosphatase (ALP), and osteocalcin (BGLAP). The B2M mRNA gene was co-amplified as an internal standard. Relative expression levels were calculated using the $\Delta\Delta$Ct method [202], normalizing first to B2M then to the expression level measured in the MSC - PEMF group at day 1.

5.3.10 Statistical Analysis

Statistical differences in ALP activity, ARS concentration, and relative gene expression were compared using one-way analysis of variance (ANOVA) among treatment groups, followed by Tukey HSD test for multiple comparisons. All analyses were performed using JMP® Pro, Version 13 (SAS Institute Inc, Cary, NC, USA). Data are depicted as mean ± standard deviation. *P*-values less than 0.05 were considered significant.

5.4 Results

5.4.1 MNBS Characteristics

The synthesized MNBS has the crystal structure of the calcium iron hydro-phosphate $Ca_9FeH(PO_4)_7$ with 85 nm average crystal size which exhibits good coherence with its respective JCPDS card no 89-0513 and small content of magnetite Fe_3O_4 **(Figure 5.1 A)**. The FTIR spectra demonstrates that the vibrational modes of iron-doped MNBS, are similar to the characteristic vibrations of pure β-TCP and are apparently determined at 553, 602, 625, 940, 996, 1041, 1091 and 1142 cm^{-1}, with the obvious iron-doping effect by generating a new band at 871 cm^{-1} **(Figure 5.1 B)**. MNBS are predominantly agglomerated, with some isolated particles showing spheroidal and elongated shapes (nanoworms) and ranging in size from 100 to 150 nm **(Figure 5.1 C)**. Magnetic properties of the MNBS were evaluated using VSM. The hysteresis curve displays ferromagnetic behavior with saturation magnetization (Ms) of 0.42515 emu/g and remanent magnetization (Mr) of 0.012805 emu/g **(Figure 5.1 D)**.
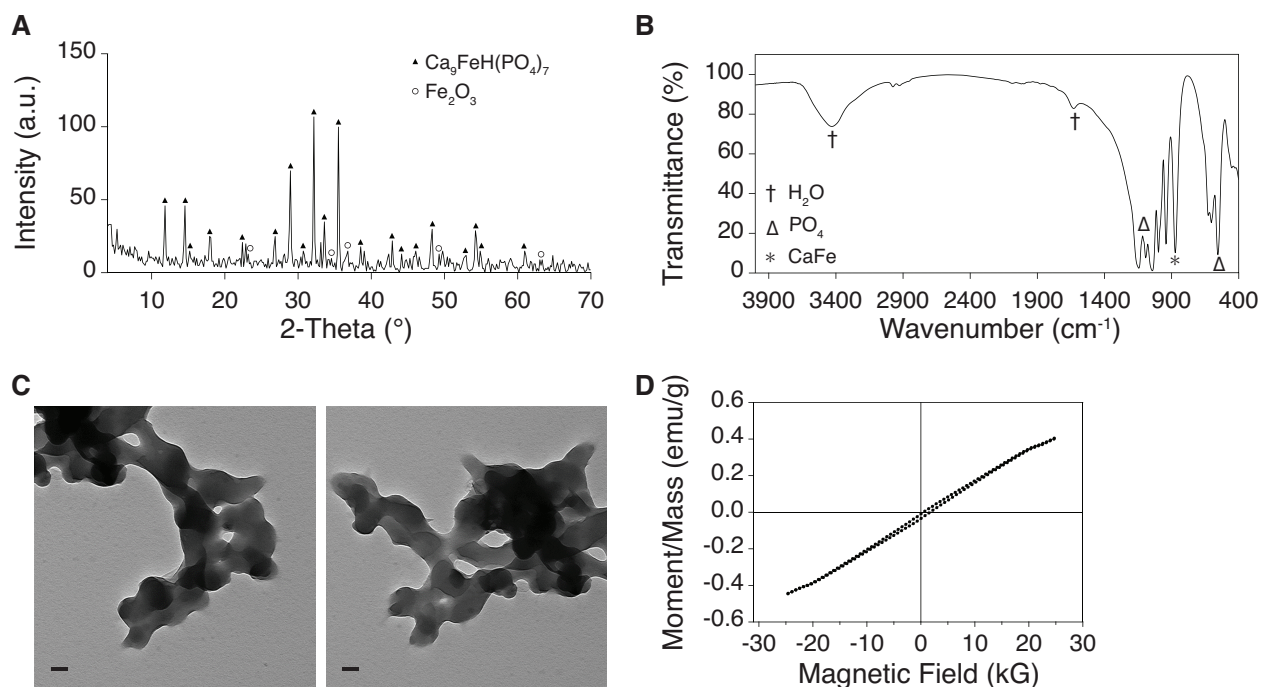
Figure 5.1 Characterization of MNBS

XRD pattern of the MNBS indicates the presence of Ca₉FeH(PO₄) primary phase (A), which is confirmed by FTIR spectra with the obvious iron-doping effect by generating a band at 871 cm-1 (B). TEM image that shows the morphology of the MNBS; scale bar = 100 nm (C) and the magnetization curve in a function of the applied magnetic field up to 25 KG (D).

5.4.2   MNBS - MSC Interaction

MNBS appeared to preferentially attach to and become internalized by the MSCs after two days of culture **(Figure 5.2).** Additionally, various morphologies of MNBS can be seen in high magnification SEM images, including particles ranging from 100 nm to 1 µm as well as single nanoparticles, nanoworms, and larger aggregates on the order of several µm.
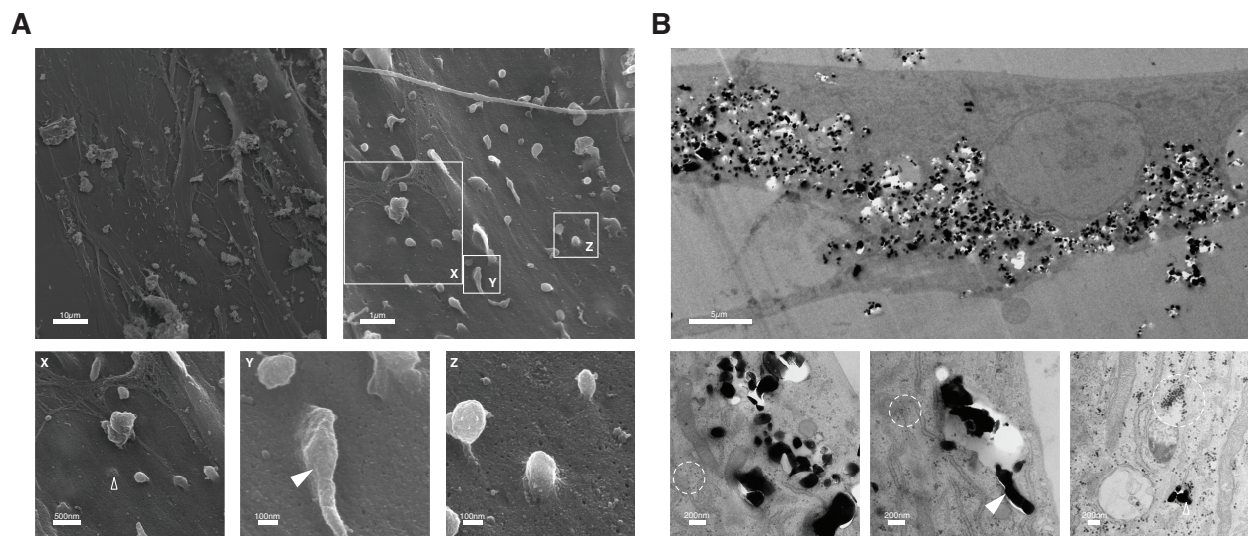
Figure 5.2 Cell-MNBS interaction

Representative images demonstrate the interaction between MSCs and MNBS. SEM images (A) highlight MNBS cell-surface attachment and internalization just below the cell surface (empty arrowhead) as single nanoparticles or nanoworms (solid arrowhead). TEM images (B) confirm MNBS internalization as both single nanoparticles (empty arrow) and nanoworm morphologies (solid arrow). While single MNBS are 100+ nm, smaller glycogenic particles (approx. 20 nm) are also apparent in TEM images (dashed circle).

5.4.3 Cell Viability

Viability of hMSCs was not greatly impacted by PEMF or MNBS exposure for up to 7 days **(Figure 5.3).** Quantitative assessment of cell viability indicated < 1% dead cells present in MSCs cultured with MNBS with or without PEMF treatment for 7 days. Quantification of cell viability herein only includes % dead cells, as we found that the Calcein-AM dye binds to the MNBS, creating an artifactual signal and giving greater than 100% live cells when normalized by cells-only.
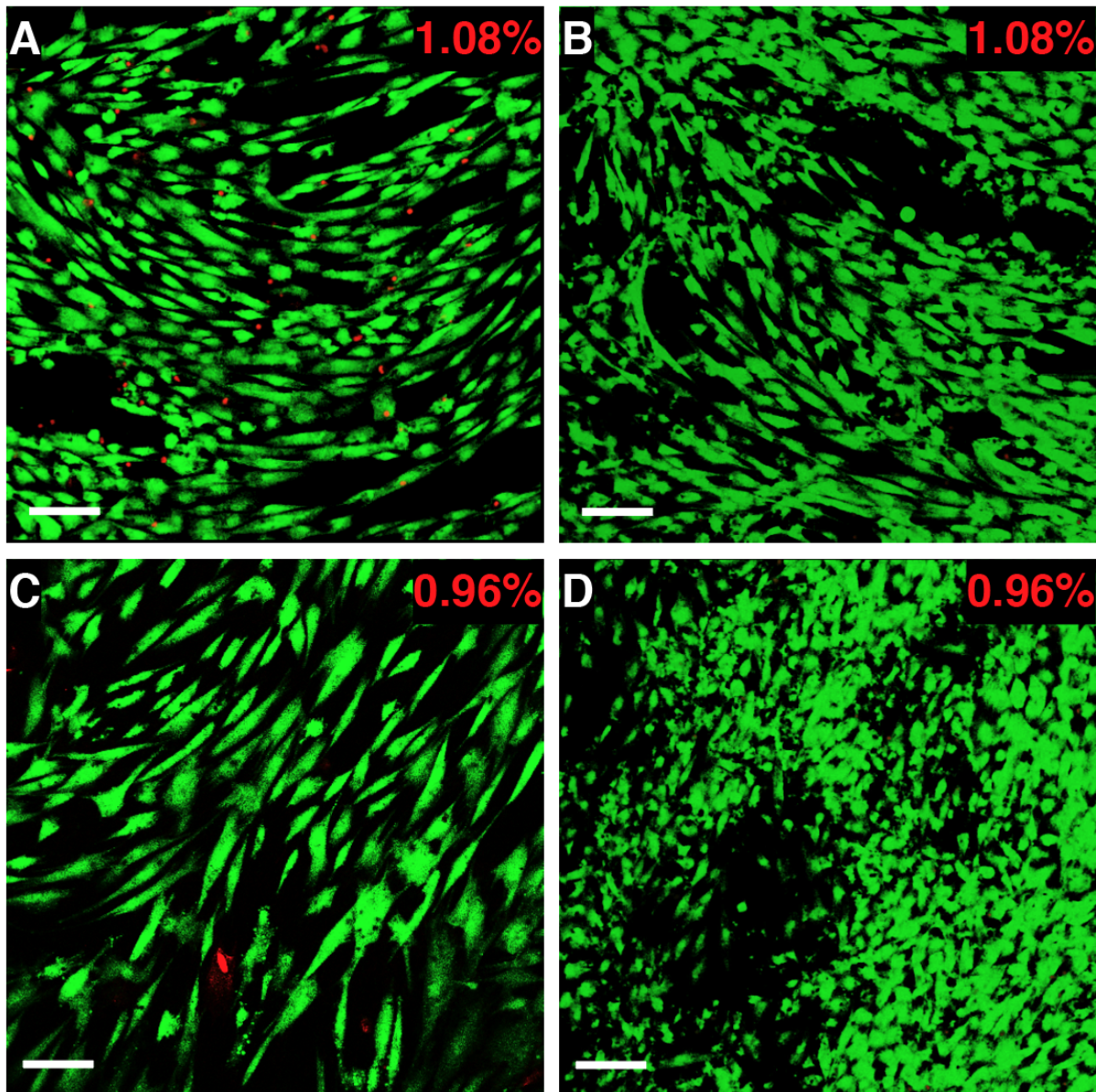
Figure 5.3 Effect of PEMF and MNBS treatment on cell viability
Representative images from LIVE/DEAD staining of hMSCs after 7 days of culture and treatment (green: live, red: dead); scale bar = 100 μm. (A) MSCs only without PEMF treatment; (B) MSCs only with PEMF treatment (C) MSCs cultured with MNBS without PEMF treatment; (D) MSCs cultured with MNBS with PEMF treatment. Cell viability was quantified by relative fluorescence readings at 645 nm. Values in red represent the percentage of dead cells. Neither PEMF nor MNBS treatment significantly affected cell viability.

5.4.4   ALP Activity

The total ALP activity of the PEMF-treated groups was significantly greater than corresponding samples that did not receive PEMF treatment at days 2, 3, 4, 5, and 9 ($p < 0.01$),

with an average increase of 2.47-fold (0.08 ± 0.04 U/ng DNA vs 0.21 ± 0.12 U/ng DNA) **(Figure 5.4)**. The increase in total ALP appears to be largely driven by an increase in extracellular ALP activity, which was increased by 3.79-fold (0.04 ± 0.02 U/ng DNA vs 0.15 ± 0.09 U/ng DNA) **(Figure 5.5)**. Note that the reduction in both the intracellular and extracellular ALP activity at days 4 and 7 **(Figure 5.4)** is likely an artifact of medium changes which occurred on these days, as medium change may disrupt normal ALP activity.

In addition to an increase in ALP activity with PEMF treatment, there is a notable shift in the day at which peak ALP activity is observed. While peak ALP activity in untreated MSCs is expected around day 14 [203], MSCs treated with PEMF demonstrated peak ALP activity at day 5 and MSCs treated with both MNBS and PEMF demonstrated a greater shift to day 3, with total ALP significantly greater than all other groups at day 3 ($p < 0.01$) **(Figures 5.4 and 5.5).**
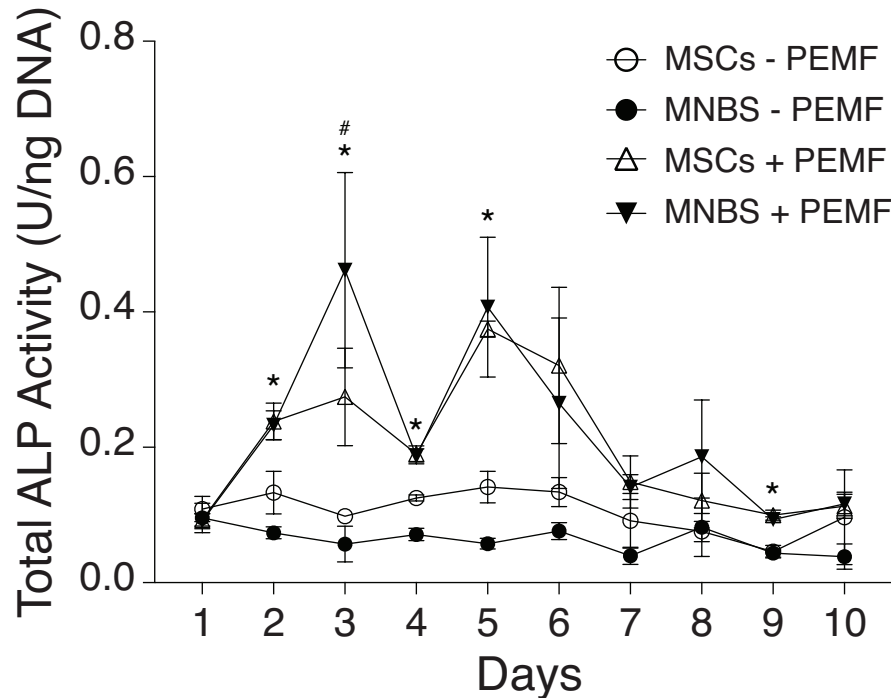
Figure 5.4 Effect of PEMF and MNBS treatment on total ALP activity
Total ALP activity remained low in samples without PEMF treatment. On day 2, 3, 4, 5, and 9, total ALP activity was increased with PEMF treatment alone, and was significantly greater than samples without PEMF treatment (* $p< 0.01$). On day 3, total ALP activity was significantly greater than all other groups (# $p< 0.01$).
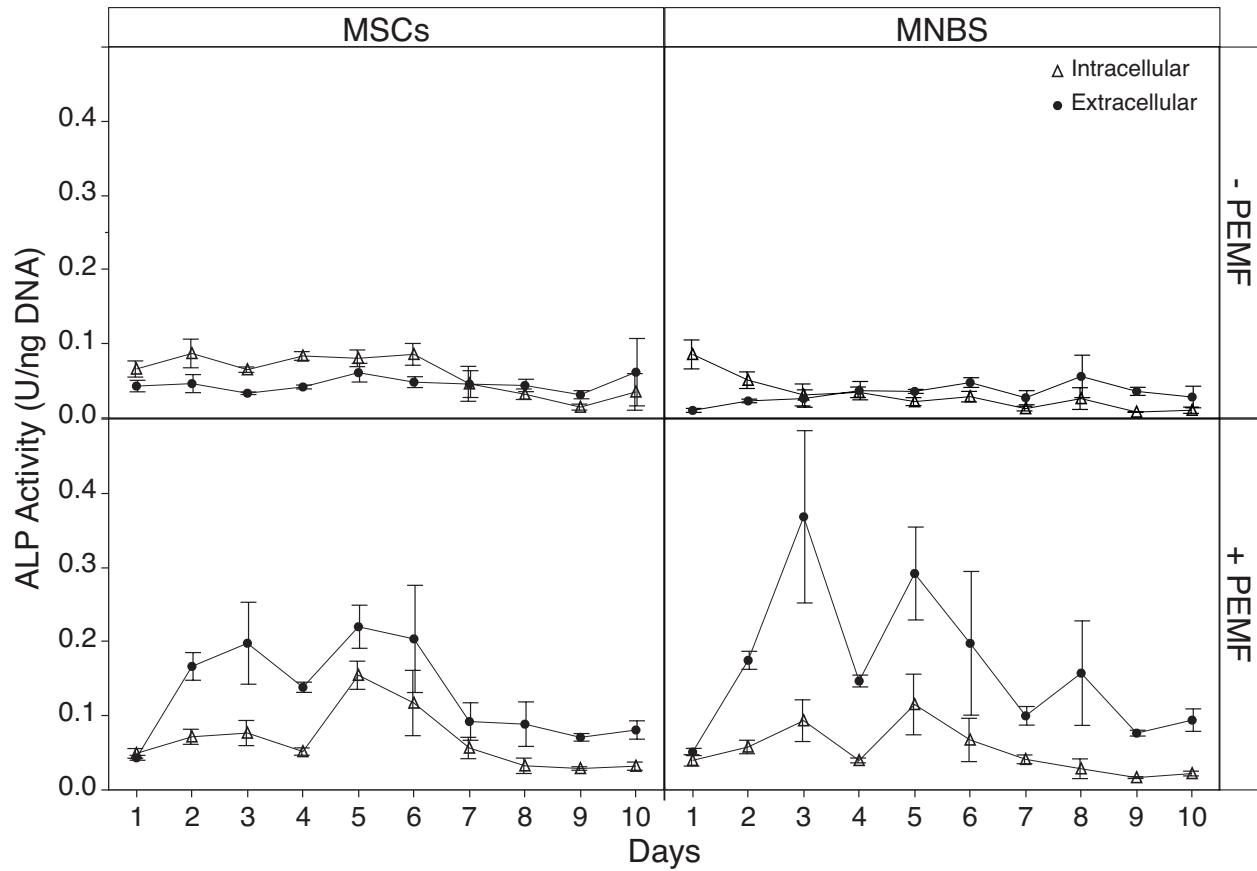
Figure 5.5 Effect of PEMF and MNBS treatment on intra- and extracellular ALP activity
Both intracellular and extracellular ALP activity remained low in samples without PEMF treatment. While intracellular ALP remained relatively low in all groups, PEMF treatment alone significantly increased extracellular ALP activity, and the combination of PEMF and MNBS further increased ALP Extracellular ALP activity and shifted peak ALP activity to day 3. Extracellular ALP activity was significantly greater in the PEMF + MNBS group at all time points starting at day 2 ($p < 0.01$).

5.4.5 Mineralization

ARS staining was present in all treatment groups, with the most staining visible in the MNBS + PEMF group on day 7 **(Figure 5.6 A)**. On day 1, ARS concentration was greatest in the MNBS - PEMF group (0.016 ± 0.003 mM), which was significantly greater than all other groups ($p < 0.01$). On day 4, ARS concentration of the MNBS - PEMF group remained similar to day 1 and was significantly greater than all groups ($p < 0.01$) except the MNBS + PEMF group, which had increased by 1.76-fold compared to day 1 (0.05 ± 0.001 mM vs 0.028 ± 0.0006 mM). On

day 7, ARS concentration was greatest in the MNBS + PEMF group, which had increased by 1.30-fold compared to day 4 (0.05 ± 0.002 mM vs 0.06 ± 0.001 mM).

Change in ARS concentration over time was quantified as the difference in ARS concentration from day 1 **(Figure 5.6 B)** to account for potential staining of residual MNBS in each sample**.** There was a continuous increase in ARS concentration over time in both of the PEMF-treated groups through day 7, with the MNBS + PEMF group demonstrating a significantly greater change in ARS concentration at 4 and 7 days compared to all other groups ($p < 0.01$). While the ARS concentration in the MSCs - PEMF group did not change from 1 to 4 days, it increased sharply at 7 days. The ARS concentration in the MNBS - PEMF group remained stable at 1 and 4 days and decreased at 7 days, likely due to removal of residual MNBS during media changes.
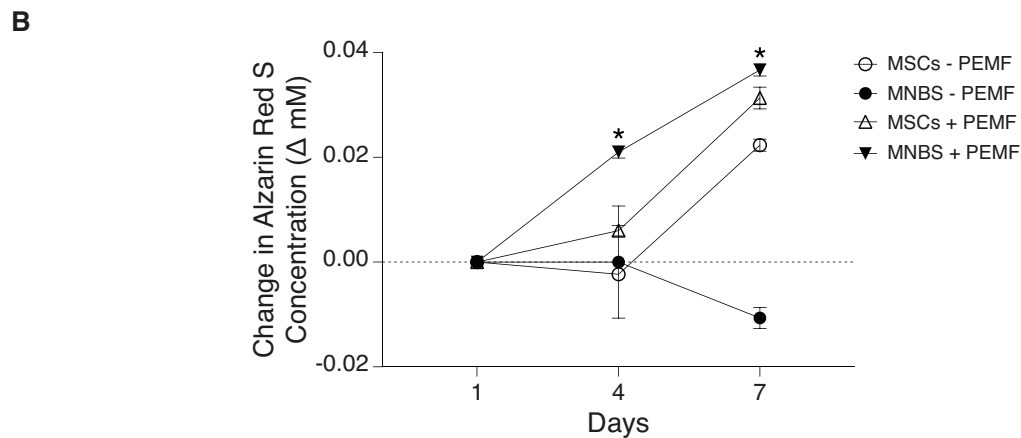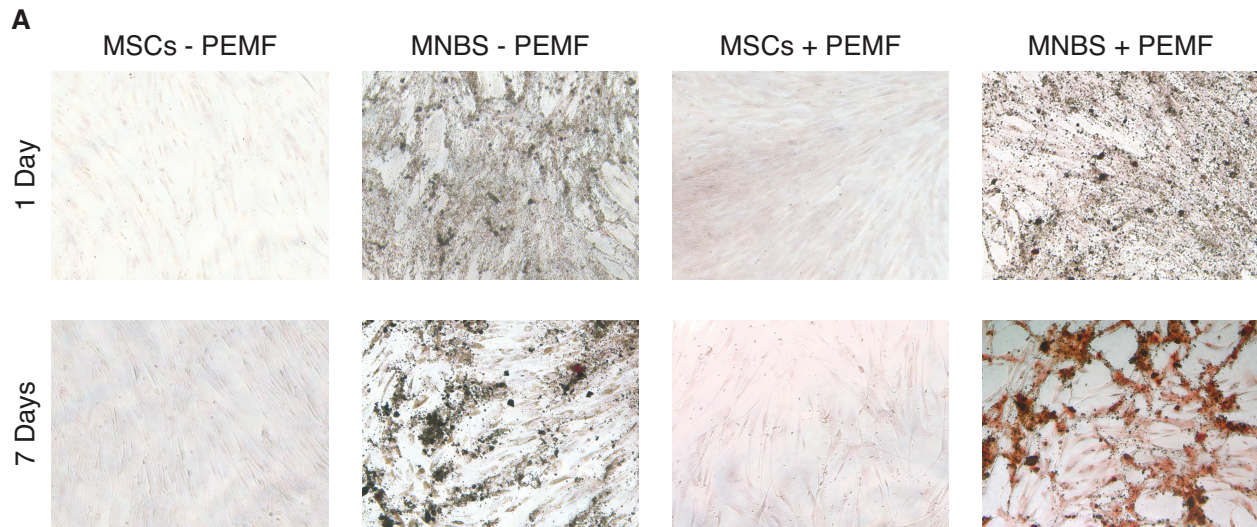
Figure 5.6 Representative images of Alizarin Red S staining for calcium deposits
Images at 1 and 7 days of culture and treatment demonstrate differences in calcium deposition with treatment condition and duration (A). Change in Alizarin Red S concentration was quantified as the difference from the corresponding day 1 concentration for each group (B). MNBS + PEMF samples demonstrated continuously increasing concentration over time, with significantly greater change in Alizarin Red S concentration compared to all other groups at day 4 and day 7 (* $p < 0.01$).

5.4.6   Gene Expression

Osteogenic performance was analyzed by measuring the gene expression of BMP-2 (cell growth and differentiation marker), ALP (marker of the initiation of osteogenesis), BGLAP and SPP1 (ossification and mineralization markers). The MSC - PEMF group exhibited low BMP-2 expression at 1, 4, and 7 days **(Figure 5.7)**. However, at 1 and 7 days, BMP-2 gene expression for

the MNBS + PEMF group was significantly greater than both the MSC - PEMF and MSC + PEMF groups ($p < 0.0001$), but similar to the MNBS - PEMF group.

All groups exhibited continuously decreasing ALP expression at 1, 4, and 7 days **(Figure 5.7)**. At 1 day, ALP gene expression for both of the MNBS - PEMF and MNBS + PEMF groups were significantly lower than MSC + PEMF group and the MNBS - PEMF group was significantly lower than the MSC - PEMF group ($p < 0.05$). On day 4 and 7, ALP expression in both the MNBS - PEMF and MNBS + PEMF groups were significantly lower than the MSC - PEMF and MSC + PEMF groups ($p < 0.0001$).

All groups exhibited an overall increase in BGLAP expression at each timepoint, with only the MSC - PEMF group exhibiting a decrease in expression at 4 days **(Figure 5.7)**. On day 1, BGLAP expression in the MNBS - PEMF group was significantly lower than the MSC - PEMF group ($p < 0.05$). On day 4, BGLAP expression in the MNBS + PEMF group was significantly greater than MSC - PEMF ($p < 0.05$). On day 7, BGLAP expression in the MNBS + PEMF group was significantly greater than all other groups ($p < 0.05$) and MNBS - PEMF was significantly greater than MSC + PEMF ($p < 0.001$).

Both the MSC - PEMF and MSC + PEMF groups exhibited relatively low SPP1 gene expression at 1, 4, and 7 days **(Figure 5.7)**. At 1, 4, and 7 days, SPP1 gene expression was significantly higher in both the MNBS - PEMF and MNBS + PEMF groups compared to MSC - PEMF and MSC + PEMF ($p < 0.0001$) and SPP1 expression in the MSC - PEMF group was significantly higher than MSC + PEMF on day 1 ($p < 0.05$), but not different at 4 and 7 days. Additionally, MNBS + PEMF SPP1 expression is significantly greater than all groups at 7 days ($p < 0.001$).
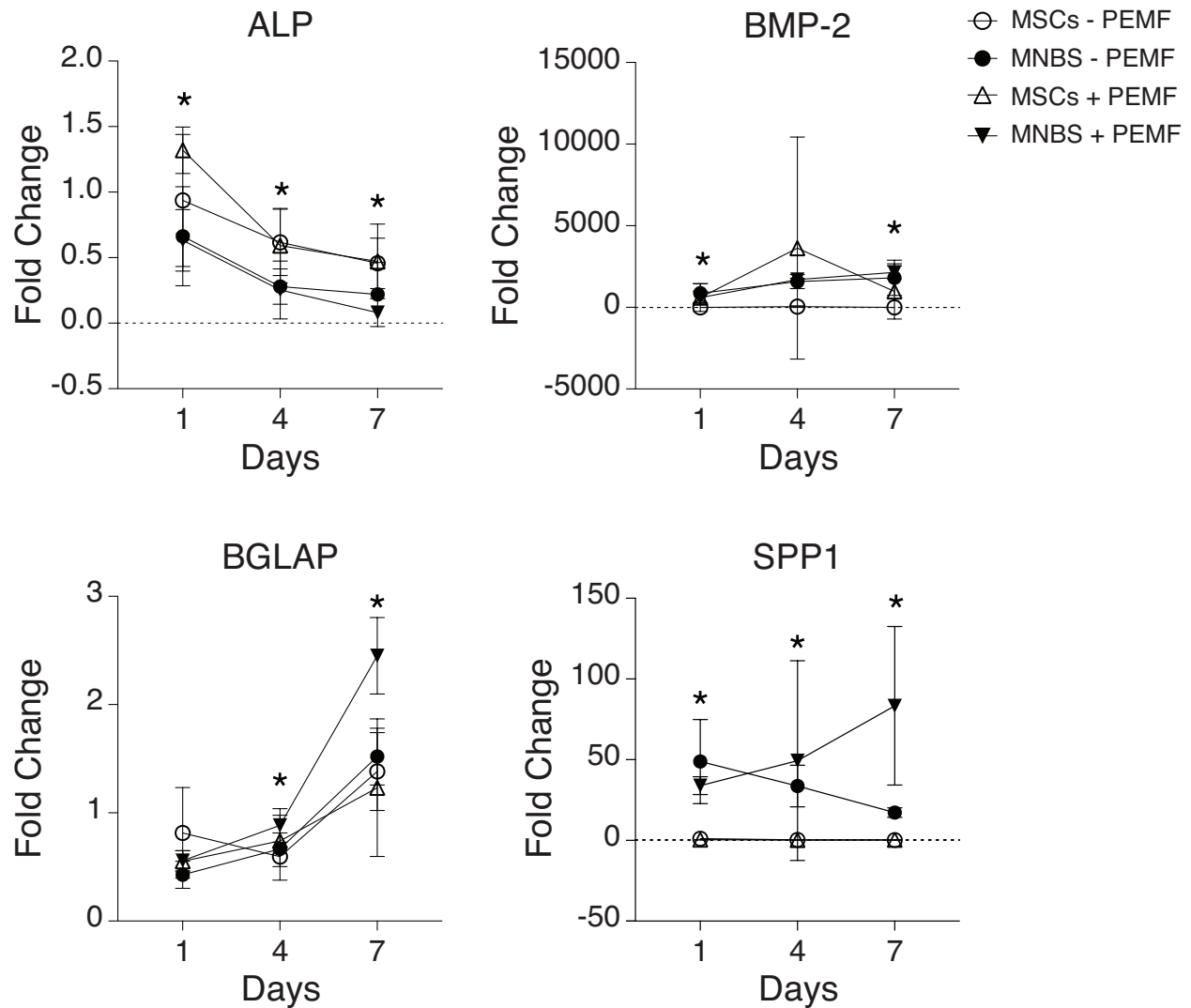
Figure 5.7 Osteogenic gene expression after 1, 4, and 7 days of treatment
ALP expression was significantly reduced with MNBS + PEMF treatment at all time points, while BMP-2 expression was significantly increased at days 1 and 7. BGLAP expression was significantly greater at days 4 and 7, and SPP1 expression was significantly increased at all time points (* $p < 0.05$).

5.5 Discussion

We hypothesized that PEMF and MNBS would synergize to enhance bone healing. To test this hypothesis, we developed an iron-doped TCP nanoparticle material and characterized its material and magnetic properties along with its interaction with cells. Utilizing our MNBS and an FDA-approved PEMF signal, we treated hMSCs and observed peak ALP activity 2 days sooner

than PEMF alone, with 2.1-fold average increase in total ALP activity and 2.3-fold average increase in mineralization compared to the untreated control group.

The main advantage of the ionic modification of β-TCP in this study is the addition of an intrinsic magnetization quality. We substituted the Ca^{2+} ions with Fe^{3+} ions to produce an intrinsic MNBS (Fe-TCP). Both the XRD and FTIR specify the accommodation of iron ions as $Ca_9FeH(PO_4)$ suggesting the substitution of two Fe^{3+} for three Ca^{2+} cations in the β-TCP lattice.

Other MNBS formulations have been used *in-vitro*, including cobalt-based MNBS which have shown to have a dramatic inhibitive effect on cell proliferation even when the administered concentration was as low as 0.02 mg/mL [204]. However, the iron-based MNBS concentration of 0.2 mg/mL in this study did not show a detrimental effect on the MSC viability **(Figure 5.3)**. Due to the potential adverse effects and cytotoxic risk, magnetic materials such as cobalt are less favorable for biological research compared to iron-based materials [193]. Moreover, iron-based MNBS exhibit excellent properties for applications in bone regeneration including increased hydrophilicity, accelerated resorption, and apatite-forming ability. It has also been demonstrated that iron-based MNBS can stimulate osteogenesis *in-vitro* and demonstrates tissue biocompatibility and bone regenerative ability *in-vivo* [200, 205, 206].

The interaction between MNBS and MSCs likely occurred in two distinct steps: First, MNBS, in either a spherical or elongated "nanoworm" form **(Figure 5.2)**, are initially attached to cell surface receptors, and second, MNBS are internalized by the cell **(Figure 5.2).** Nanoworm structures are believed to bind more cell surface receptors compared to the single, spherical NP, and facilitate their internalization [207].

Our observations of PEMF-only treatment are consistent with prior reports showing osteogenic differentiation. PEMF has been shown to affect various cellular responses, including

cell proliferation, differentiation, and maturation [48, 153, 187]. Its effects are mostly well-known among musculoskeletal research, where PEMF has been shown to induce osteogenesis and bone tissue mineralization [187].

5.5.1 PEMF + MNBS stimulates early ALP activity, an initial marker for osteogenic activity

While several groups have reported intracellular ALP activity in human mesenchymal stem cells over time [208, 209], to our knowledge we are the first group to report total ALP activity by assessing all cells, media, and media changes daily throughout 10 days of culture.

ALP is a well-known marker for osteogenic activity and bone-cell differentiation and is essential to supply phosphate for bone mineral, as lack of ALP leads to under-mineralization of bone [210]. Successful osteogenesis is commonly indicated by high ALP levels, which mineralization of the bone matrix ensues. Therefore, we assessed ALP expression enzymatically, histochemically, and at the mRNA level over time to investigate the synergistic effect of PEMF and MNBS on *in-vitro* osteogenesis.

In an earlier study, the combined treatment of BMP-2 and PEMF showed an increase in ALP gene expression during the differentiation phase of rat primary osteoblasts cells with maximum ALP activity at day 14 [211]. Our data indicates a shift in peak ALP activity to day 3 with PEMF + MNBS treatment **(Figure 5.4)**. This is notably earlier than PEMF treatment alone, which also induced earlier-than-nominal peak ALP activity at day 5. Moreover, we did not observe a significant change in ALP activity over time in the non-treated control group. This finding aligns well with findings of others, which has shown that nominal peak *in-vitro* ALP activity occurs at the end of the cell differentiation and proliferation stage from days 5 to 14 with decreasing ALP levels thereafter [203], suggesting that PEMF treatment alone may stimulate early ALP activity

that is further shifted when additional receptions for the transduction of the PEMF energy by the cell are presented by the attachment and internalization of MNBS. This shift to earlier peak ALP activity can be accounted for by an increase in extracellular ALP activity in MNBS + PEMF samples **(Figure 5.5)**. In addition, gene expression results showed high ALP expression initially, followed by decreasing expression over time for all treatment groups **(Figure 5.7)**. This trend in ALP expression was in parallel with an increase in osteocalcin (BGLAP) expression for all groups and an increase in osteopontin (SPP1) expression for the PEMF + MNBS group over time. Our results are consistent with those of others which shows a decrease in ALP activity over time as mineralization increases [208, 212].

5.5.2 PEMF + MNBS stimulates stable increase in calcium deposition, an indicator of osteogenic maturation

Our data indicate a stable increase in calcium deposition through 7 days of treatment with PEMF + MNBS at levels significantly greater than PEMF treatment alone, as demonstrated by ARS staining and quantification **(Figure 5.6)**. This contrasted with the non-treated control group, which had a low concentration of calcium deposits through day 4 followed by a peak at day 7. In addition, this trend in calcium deposition was in parallel with gene expression results indicating a gradual and significant increase in osteocalcin (BGLAP) and osteopontin (SPP1) expression over time.

Our study is limited by potential artifactual trends throughout our time course experiments due to medium changes. We observed a dip in extracellular ALP activity on the days where media were changed, which may be due to disruption of the signaling cascade driven by secreted factors in the media. However, to our knowledge, this is the first *in-vitro* study of ALP activity to include intracellular and extracellular ALP and is strengthened by the fact that all ALP activity was

evaluated through a 10-day time course, allowing us to capture this change in activity corresponding with media changes. Another limitation is the potential staining of MNBS by ARS, causing artifactual signal in the quantification of calcium deposition. While samples were thoroughly washed to remove excess MNBS, particles adhered to or internalized by MSCs remained present and may have been stained. Specifically, ARS signal was observed in samples with MNBS on day 1 of culture, before the expected initiation of osteogenesis. Fan et al., demonstrated that alizarin red can be removed from an aqueous environment by magnetic chitosan or polypyrrole nanoparticles [213], which could explain the results seen at day 1. However, after 7 days, there was a significant increase in ARS signal due to the synergistic effect of MNBS combined with PEMF treatment that is large enough to overcome the noise of the MNBS-staining artifact, while PEMF-treatment alone did not significantly increase mineralization at any time point. Moreover, our ARS results align with our gene expression results for BGLAP and SPP1, which are not susceptible to artifactual signals from the MNBS.

Despite these limitations, we demonstrate statistically significant effects *in-vitro* that may translate in the future to clinically relevant effects in humans. Potential clinical indications would include accelerated bone regeneration for large bone defects where bone healing takes several months and may also benefit patients with osteoporosis to counter decreasing bone density. Additionally, the PEMF + MNBS system may also be applied to other cell types such as cartilage, and intervertebral disc cells. There is an additional safety benefit to utilizing this combination therapy in that it allows localized treatment delivery to the injury site. Other therapies for stimulating bone growth, such as growth factor injections, cause excess bone growth [214] potentially cause aberrant effects (e.g. spinal stenosis).

In summary, we observed that PEMF treatment combined with MNBS synergistically stimulated early peak ALP expression and significantly upregulated calcium deposition over time in hMSCs. By demonstrating this synergistic effect of PEMF and MNBS on osteogenesis, these findings support that this combination therapy may provide a method for accelerated bone healing.

5.6 Acknowledgements

5.7 Author Disclosure Statement

EIW, NZ, and JTR are employed by and own stock in Orthofix, Inc. No competing financial interests exist for all other authors.

6   Conclusions and Future Work

6.1   Summary and Main Conclusions

The experiments performed in this dissertation represent significant contributions to the development of two novel energy-based therapies for painful spine conditions. This work demonstrates the design and application of pre-clinical systems for therapeutic ultrasound and magnetic-field exposure, along with the thorough assessment of responses at tissue, cellular, and molecular levels. The findings described in this dissertation are a pivotal pre-clinical step towards the advancement of energy-based therapeutics to clinical use. In Chapter 2, we demonstrate the technical feasibility of targeted, noninvasive delivery of acoustic energy to rat-tail intervertebral discs (IVD) and assessment of biological responses to Low-intensity Pulsed Ultrasound (LIPUS) exposure. We found that LIPUS exposure regulates extracellular matrix (ECM) and inflammatory gene expression in rat-tail IVDs with increased pro-inflammatory gene expression. Chapter 3 describes the design, fabrication, characterization, and validation of an *in-vitro* LIPUS exposimetry system for delivering uniform acoustic energy to distal targets with negligible heating. We found that far-field LIPUS exposure upregulates total collagen content in annulus fibrosus cells with a magnitude similar to growth factor treatment. Chapter 4 presents the use and validation of Design of Experiments (DOE) for LIPUS parameter exploration, response prediction, and optimization. The LIPUS system described in Chapter 3 was used, and we found that Pulse Repetition Frequency (PRF) was the most significant factor for modulating catabolic and pro-inflammatory gene expression while peak intensity was most significant for modulating anabolic gene expression, and that both factors interacted with treatment duration to influence ECM gene expression in inflammatory annulus fibrosus cells. Lastly, in Chapter 5 we show that magnetic nanoparticles (MNBS) synergize with pulsed electromagnetic fields (PEMF) to accelerate the

induction of osteogenesis by stimulating early peak alkaline phosphatase (ALP) activity and upregulating calcium deposition over time in mesenchymal stem cells (MSCs). Taken together, these studies support the following main conclusions:

(1) LIPUS energy can be delivered noninvasively to damaged IVDs *in-vivo* to **stimulate anabolic and anti-inflammatory gene expression;**

(2) Annulus fibrosus cells exposed to far-field LIPUS demonstrate **increased total collagen synthesis at a magnitude similar to growth factor treatment**;

(3) Metabolic activity in annulus fibrosus cells is **influenced by LIPUS pulse repetition frequency, peak intensity, and treatment duration settings**, and;

(4) Combining magnetic nanoparticles with PEMF **accelerates peak ALP activity and mineralization rate in MSCs**.

6.2 Interpretation of Key Findings

In Chapter 2 we demonstrated the technical feasibility of targeted delivery of LIPUS energy to rat-tail IVDs and assessment of tissue response via gene expression analysis. While several previously published studies have demonstrated anabolic and anti-catabolic activity in IVD cells with LIPUS exposure, to our knowledge, this was the first published *in-vivo* study of LIPUS bioeffects in IVDs with acute injury. We found that LIPUS increases type II collagen gene expression and reduces TNFα gene expression in inflammatory discs, suggesting that previously observed *in-vitro* LIPUS effects may translate *in-vivo*. These findings motivated the development of the robust *in-vitro* system that was used to the parametric studies described in Chapters 3 and 4, respectively. The findings in Chapter 2 where supported by results in Chapter 3 and 4, which also showed LIPUS-induced matrix synthesis and anti-inflammatory activity. Specifically, in Chapter 2 we observed anabolic and anti-inflammatory effects only in rats with high expression of

IL6 after injury, a finding was supported by results in Chapter 4. In Chapter 3, we fabricated, characterized, and validated a pre-clinical, *in-vitro* model for delivering uniform LIPUS energy to cell cultures which included an acoustic standoff for low frequency sources to place target samples within the uniform acoustic far-field. We show that by exposing IVD cells to far-field LIPUS energy, collagen synthesis was increased with a magnitude similar to that of growth factor treatment. While intradiscal growth factor injections have shown some promise, this technique suffers from long-term safety and efficacy concerns, likely due to the potential depressurization and reduction in mechanical integrity of the disc. However, our results indicate the potential to noninvasively stimulate the repair of damaged IVD tissues. Moreover, compared to typical near-field LIPUS systems described in literature, our far-field system is more clinically relevant for extracorporeal stimulation of deep tissues such as the IVD. We also introduced the novel use of gradient analysis to evaluate the uniformity of acoustic intensity fields and demonstrated that typical systems may be more susceptible to acoustic artifacts that my result in inaccurate or inconsistent dosing. By mitigating these acoustic artifacts, and thereby removing potentially confounding factors, we could successfully use this LIPUS system in parametric studies. In Chapter 4, we evaluated LIPUS dosing parameters using DOE and found PRF to be the most influential factor for stimulating anti-catabolic and anti-inflammatory activity in inflammatory annulus fibrosus cells. When PRF was varied, total energy was held constant, suggesting that the cells may be sensing and responding to pulsing characteristics such as pulse duration and frequency. One possibility is that the long pulse intervals of the low PRF group are less efficiently transduced by mechanosensitive cell receptors, resulting in a damped response. While type I collagen gene expression was not increased with LIPUS exposure, there was a significant reduction in the expression of matrix metalloproteinase 1 and 13, which are the primary enzymes

capable of cleaving interstitial collagen molecules. The reduction in catabolic gene expression observed in Chapter 4 may explain the increase in collagen content observed in Chapter 3. Chapter 4 illustrates the capability and benefits of implementing DOE for exploring dose-response relationships in energy-based therapeutics and motivates expanding the use of DOE to other modalities such as PEMF. Chapter 5, we evaluated interactions between MNBS and PEMF and found synergistic effects on ALP activity and mineralization in MSCs. By demonstrating an acceleration of the onset of osteogenesis as well as an increase in mineralization over time, these findings support the use of PEMF and MNBS as a combination therapy for accelerating bone healing. These results also suggest that by introducing MNBS to enhancing the effects of PEMF alone, it may be possible to reduce the overall dose of PEMF without sacrificing efficacy, and in turn reduce the potential for off target effects.

This dissertation presents novel contributions to the development of two energy-based therapeutics that could potentially translate to improved patient outcomes in the clinical management of low back pain. Overall, we found dose-response relationships between LIPUS and annulus fibrosus cells, which may inform patient-specific dosing, and we identified synergistic effects from the combination of PEMF and MNBS, which may be used to improve success rates in spinal fusion cases. Notably, our results demonstrate consistent anabolic and anti-inflammatory activity in inflammatory disc cells exposed to LIPUS both *in-vitro* and *in-vivo* and show that these effects may be influenced by LIPUS parameter settings. Taken together, this suggest that future clinical use could benefit from patient-specific dosing. However, LIPUS may not be effective in cases of severe IVD degeneration which may ultimately require spinal fusion. The synergistic effects observed in our study of PEMF and MNBS motivates its potential in rescuing unsuccessful fusions by accelerating the onset of osteogenesis and increasing mineralization rates.

6.3 Future Work

In Chapter 4 we demonstrated the successful use of screening DOE to identify factors and interactions that influence ECM gene expression and to predict gene expression responses with reasonable accuracy. These will inform expanded parameter ranges to be used in more complex (i.e. non-linear) modeling of responses via Response Surface Methodology. Data from this study may expand effect ranges, improve model fit, and ultimately increase the reliability of response predictions. The *in-vitro* experiments presented in Chapter 5 could be expanded upon in future studies to investigate whether our findings translate to an *in-vivo* model of spinal fusion. These studies will require the development of an *in-vivo* nanoparticle carrier and delivery method which could include the injection or implantation of a hydrogel or 3D-printed scaffold.

Collectively, the work presented in this dissertation is of great importance for the advancement of energy-based therapeutics for IVD injuries. These findings will motivate the novel use of noninvasive, energy-based therapeutics to improve clinical outcomes for patients experiencing low back pain.

7   Bibliography

1.   Vallfors B (1985) Acute, subacute and chronic low back pain: clinical symptoms, absenteeism and working environment. Scand J Rehabil Med Suppl 11:1–98.

2.   DePalma MJ, Ketchum JM, Saullo T (2011) What Is the Source of Chronic Low Back Pain and Does Age Play a Role? Pain Med 12:224–233. doi: 10.1111/j.1526-4637.2010.01045.x

3.   Peng B-G (2013) Pathophysiology, diagnosis, and treatment of discogenic low back pain. World J Orthop 4:42. doi: 10.5312/wjo.v4.i2.42

4.   Guterl CC, See EY, Blanquer S (2013) Challenges and strategies in the repair of ruptured annulus fibrosus. European Cells and Materials 25:1–21. doi: 10.22203/ecm.v025a01

5.   DePalma MJ, Ketchum JM, Saullo TR, Laplante BL (2012) Is the History of a Surgical Discectomy Related to the Source of Chronic Low Back Pain? Pain Physician 15:E53–E58.

6.   Likhitpanichkul M, Dreischarf M (2014) Fibrin-genipin adhesive hydrogel for annulus fibrosus repair: performance evaluation with large animal organ culture, in situ biomechanics, and in vivo …. European Cells and Materials 28:25–38. doi: 10.22203/ecm.v028a03

7.   Handa T, Ishihara H, Ohshima H, et al (1997) Effects of hydrostatic pressure on matrix synthesis and matrix metalloproteinase production in the human lumbar intervertebral disc. SPINE 22:1085–1091. doi: 10.1097/00007632-199705150-00006

8. Matsumoto T, Kawakami M, Kuribayashi K, et al (1999) Cyclic mechanical stretch stress increases the growth rate and collagen synthesis of nucleus pulposus cells in vitro. SPINE 24:315–319. doi: 10.1097/00007632-199902150-00002

9. Reza AT, Nicoll SB (2007) Hydrostatic Pressure Differentially Regulates Outer and Inner Annulus Fibrosus Cell Matrix Production in 3D Scaffolds. Ann Biomed Eng 36:204–213. doi: 10.1007/s10439-007-9407-6

10. Lee CR, Sakai D, Nakai T, et al (2007) A phenotypic comparison of intervertebral disc and articular cartilage cells in the rat. Eur Spine J 16:2174–2185. doi: 10.1007/s00586-007-0475-y

11. Lotz JC, Fields AJ, Liebenberg EC (2013) The Role of the Vertebral End Plate in Low Back Pain:. Global Spine J. doi: 10.1055/s-0033-1347298

12. Skaggs DL, Weidenbaum M, latridis JC, et al (1994) Regional Variation in Tensile Properties and Biochemical Composition of the Human Lumbar Anulus Fibrosus. SPINE 19:

13. MARCHAND F, AHMED AM (1990) Investigation of the Laminate Structure of Lumbar Disc Anulus Fibrosus. SPINE 15:

14. Cloyd JM, Malhotra NR, Weng L, et al (2007) Material properties in unconfined compression of human nucleus pulposus, injectable hyaluronic acid-based hydrogels and tissue engineering scaffolds. Eur Spine J 16:1892–1898. doi: 10.1007/s00586-007-0443-6

15. Wong J, Sampson SL, Bell-Briones H, et al (2019) Nutrient supply and nucleus pulposus cell function: effects of the transport properties of the cartilage endplate and

potential implications for intradiscal biologic therapy. Osteoarthritis and Cartilage 27:956–964. doi: 10.1016/j.joca.2019.01.013

16. Dolor A, Sampson SL, Lazar AA, et al (2019) Matrix modification for enhancing the transport properties of the human cartilage endplate to improve disc nutrition. PLoS ONE 14:e0215218–18. doi: 10.1371/journal.pone.0215218

17. Roberts S, Evans H, TRIVEDI J, MENAGE J (2006) HISTOLOGY AND PATHOLOGY OF THE HUMAN INTERVERTEBRAL DISC. The Journal of Bone and Joint Surgery-American Volume 88:10–14. doi: 10.2106/00004623-200604002-00003

18. Pattappa G, Li Z, Peroglio M, et al (2012) Diversity of intervertebral disc cells: phenotype and function. Journal of Anatomy 221:480–496. doi: 10.1111/j.1469-7580.2012.01521.x

19. Hastreiter D, Ozuna RM, Spector M (2001) Regional variations in certain cellular characteristics in human lumbar intervertebral discs, including the presence of α-smooth muscle actin. J Orthop Res 19:597–604. doi: 10.1016/S0736-0266(00)00069-3

20. Bron JL, Helder MN, Meisel H-J, et al (2008) Repair, regenerative and supportive therapies of the annulus fibrosus: achievements and challenges. Eur Spine J 18:301–313. doi: 10.1007/s00586-008-0856-x

21. Smith LJ, Nerurkar NL, Choi K-S, et al (2011) Degeneration and regeneration of the intervertebral disc: lessons from development. Dis Model Mech 4:31–41. doi: 10.1242/dmm.006403

22.   Roberts S, Evans H, TRIVEDI J, MENAGE J (2006) Histology and Pathology of the Human Intervertebral Disc. J Bone Joint Surg Am 88:10. doi: 10.2106/JBJS.F.00019

23.   Yoon ST, Patel NM (2006) Molecular therapy of the intervertebral disc. Eur Spine J 15:379–388. doi: 10.1007/s00586-006-0155-3

24.   Roberts S (2002) Disc morphology in health and disease. Biochem Soc Trans 30:864–869. doi: 10.1042/bst0300864

25.   Freemont AJ (2009) The cellular pathobiology of the degenerate intervertebral disc and discogenic back pain. Rheumatology (Oxford) 48:5–10. doi: 10.1093/rheumatology/ken396

26.   Dowdell J, Erwin M, Choma T, et al (2017) Intervertebral Disk Degeneration and Repair. Neurosurgery 80:S46–S54. doi: 10.1093/neuros/nyw078

27.   Boos N, Weissbach S, Rohrbach H, et al (2002) Classification of age-related changes in lumbar intervertebral discs: 2002 Volvo Award in basic science. SPINE 27:2631–2644. doi: 10.1097/00007632-200212010-00002

28.   Schroeder GD, Guyre CA, Vaccaro AR (2016) The epidemiology and pathophysiology of lumbar disc herniations. Seminars in Spine Surgery 28:2–7. doi: 10.1053/j.semss.2015.08.003

29.   Berg-Johansen B, Fields AJ, Liebenberg EC, et al (2017) Structure-function relationships at the human spinal disc-vertebra interface. J Orthop Res 38:1491–10. doi: 10.1002/jor.23627

30.   Ghannam M, Jumah F, Mansour S, et al (2017) Surgical anatomy, radiological features, and molecular biology of the lumbar intervertebral discs. Clin Anat 30:251–266. doi: 10.1002/ca.22822

31. Auerbach JD, Johannessen W, Borthakur A, et al (2006) In vivo quantification of human lumbar disc degeneration using T(1rho)-weighted magnetic resonance imaging. Eur Spine J 15 Suppl 3:S338–44. doi: 10.1007/s00586-006-0083-2

32. Fields AJ, Battié MC, Herzog RJ, et al (2019) Measuring and reporting of vertebral endplate bone marrow lesions as seen on MRI (Modic changes): recommendations from the ISSLS Degenerative Spinal Phenotypes Group. Eur Spine J 28:2266–2274. doi: 10.1007/s00586-019-06119-6

33. Carragee EJ, Don AS, Hurwitz EL, et al (2009) 2009 ISSLS Prize Winner: Does Discography Cause Accelerated Progression of Degeneration Changes in the Lumbar Disc: A Ten-Year Matched Cohort Study. SPINE 34:2338–2345. doi: 10.1097/BRS.0b013e3181ab5432

34. OSTI OL, VERNONROBERTS B, MOORE R, FRASER RD (1992) Annular Tears and Disk Degeneration in the Lumbar Spine - a Postmortem Study of 135 Disks. J Bone Joint Surg Br 74:678–682.

35. Thomas Edwards W, Ordway NR, Zheng Y, et al (2001) Peak Stresses Observed in the Posterior Lateral Anulus. SPINE 26:1753.

36. Urban JP, McMullin JF (1988) Swelling pressure of the lumbar intervertebral discs: influence of age, spinal level, composition, and degeneration. 13:179–187.

37. Urban JP, McMullin JF (1988) Swelling pressure of the lumbar intervertebral discs: influence of age, spinal level, composition, and degeneration. SPINE 13:179–187. doi: 10.1097/00007632-198802000-00009

38. Urban JP, Roberts S (2003) Degeneration of the intervertebral disc. Arthritis Res Ther 2003 5:3 5:1. doi: 10.1186/ar629

39.   Vergroesen PPA, Kingma I, Emanuel KS, et al (2015) Mechanics and biology in intervertebral disc degeneration: a vicious circle. Osteoarthritis and Cartilage 23:1057–1070. doi: 10.1016/j.joca.2015.03.028

40.   Chen M-H, Sun J-S, Liao S-Y, et al (2015) Low-intensity pulsed ultrasound stimulates matrix metabolism of human annulus fibrosus cells mediated by transforming growth factor β1 and extracellular signal-regulated kinase pathway. Connective Tissue Research 56:219–227. doi: 10.3109/03008207.2015.1016609

41.   Hukins DWL, Meakin JR (2015) Relationship Between Structure and Mechanical Function of the Tissues of the Intervertebral Joint. Am Zool 40:42–052.

42.   Guiot BH, Fessler RG (2000) Molecular biology of degenerative disc disease. Neurosurgery 47:1034–1040. doi: 10.1097/00006123-200011000-00003

43.   Naqvi SM, Buckley CT (2016) Bone Marrow Stem Cells in Response to Intervertebral Disc-Like Matrix Acidity and Oxygen Concentration: Implications for Cell-based Regenerative Therapy. SPINE 41:743–750. doi: 10.1097/BRS.0000000000001314

44.   Horner HA, Urban JP (2001) 2001 Volvo Award Winner in Basic Science Studies: Effect of nutrient supply on the viability of cells from the nucleus pulposus of the intervertebral disc. 26:2543–2549. doi: 10.1097/00007632-200112010-00006

45.   Gilbert HTJ, Hodson N, Baird P, et al (2016) Acidic pH promotes intervertebral disc degeneration: Acid-sensing ion channel -3 as a potential therapeutic target. Sci Rep 6:37360. doi: 10.1038/srep37360

46.	Gabr MA, Jing L, Helbling AR, et al (2011) Interleukin-17 synergizes with IFNγ or TNFα to promote inflammatory mediator release and intercellular adhesion molecule-1 (ICAM-1) expression in human intervertebral disc cells. J Orthop Res 29:1–7. doi: 10.1002/jor.21206

47.	Burke JG, Watson RWG, McCormack D, et al (2002) Intervertebral discs which cause low back pain secrete high levels of proinflammatory mediators. J Bone Joint Surg Br 84:196–201. doi: 10.1302/0301-620x.84b2.12511

48.	Miller SL, Coughlin DG, Waldorff EI, et al (2016) Pulsed electromagnetic field (PEMF) treatment reduces expression of genes associated with disc degeneration in human intervertebral disc cells. Spine J 16:770–776. doi: 10.1016/j.spinee.2016.01.003

49.	Le Maitre CL, Freemont AJ, Hoyland JA (2005) The role of interleukin-1 in the pathogenesis of human Intervertebral disc degeneration. Arthritis Res Ther 2003 5:3 7:1–14. doi: 10.1186/ar1732

50.	Rajasekaran S, Bajaj N, Tubaki V, et al (2013) ISSLS Prize winner: The anatomy of failure in lumbar disc herniation: an in vivo, multimodal, prospective study of 181 subjects. SPINE 38:1491–1500. doi: 10.1097/BRS.0b013e31829a6fa6

51.	Hegewald AA, Medved F, Feng D, et al (2013) Enhancing tissue repair in annulus fibrosus defects of the intervertebral disc: analysis of a bio-integrative annulus implant in an in-vivoovine model. J Tissue Eng Regen Med 9:405–414. doi: 10.1002/term.1831

52.	SMITH JW, WALMSLEY R (1951) Experimental incision of the intervertebral disc. J Bone Joint Surg Br 33-B:612–625.

53.   Hampton D, Laros G, McCarron R, Franks D (1989) Healing potential of the anulus fibrosus. SPINE 14:398–401.

54.   OSTI OL, Vernon-Roberts B, FRASER RD (1990) 1990 Volvo Award in Experimental Studies: Anulus Tears and Intervertebral Disc Degeneration: An Experimental Study Using an Animal Model. SPINE 15:762–767. doi: 10.1097/00007632-199008010-00005

55.   Ahlgren BD, Vasavada A, Brower RS, et al (1994) Anular incision technique on the strength and multidirectional flexibility of the healing intervertebral disc. SPINE 19:948–954.

56.   Phillips FM, Slosar PJ, Youssef JA, et al (2013) Lumbar spine fusion for chronic low back pain due to degenerative disc disease: a systematic review. SPINE 38:E409–22. doi: 10.1097/BRS.0b013e3182877f11

57.   Omidi-Kashani F, Hasankhani EG, Ashjazadeh A (2014) Lumbar Spinal Stenosis: Who Should Be Fused? An Updated Review. Asian Spine Journal 8:521–530. doi: 10.4184/asj.2014.8.4.521

58.   Hedlund R, Johansson C, Hägg O, et al (2016) The long-term outcome of lumbar fusion in the Swedish lumbar spine study. The Spine Journal 16:579–587. doi: 10.1016/j.spinee.2015.08.065

59.   Yoshihara H, Yoneoka D (2015) National trends in the surgical treatment for lumbar degenerative disc disease: United States, 2000 to 2009. The Spine Journal 15:265–271. doi: 10.1016/j.spinee.2014.09.026

60. Xu X-M, Zhang G, Wang F, et al (2016) Bone Graft Options for Spine Fusion in Adolescent Patients with Idiopathic Scoliosis. Chinese Medical Journal 129:105–107. doi: 10.4103/0366-6999.172605

61. Reid PC, Morr S, Kaiser MG (2019) State of the union: a review of lumbar fusion indications and techniques for degenerative spine disease. Journal of Neurosurgery: Spine 31:1–14. doi: 10.3171/2019.4.SPINE18915

62. Cottrill E, Pennington Z, Ahmed AK, et al (2019) The effect of electrical stimulation therapies on spinal fusion: a cross-disciplinary systematic review and meta-analysis of the preclinical and clinical data. Journal of Neurosurgery: Spine 32:106–126. doi: 10.3171/2019.5.SPINE19465

63. Knaub MA, Won DS, McGuire R, Herkowitz HN (2005) Lumbar spinal stenosis: indications for arthrodesis and spinal instrumentation. Instr Course Lect 54:313–319.

64. Schek RM, Orthopaedics LAPWMDO, Medicine MSSO, et al (2011) Genipin-crosslinked fibrin hydrogels as a potential adhesive to augment intervertebral disc annulus repair. European Cells and Materials 21:373–383. doi: 10.22203/ecm.v021a28

65. Chan S, Gantenbein-Ritter B (2012) Intervertebral disc regeneration or repair with biomaterials and stem cell therapy - feasible or fiction? Swiss Med Wkly 1–12. doi: 10.4414/smw.2012.13598

66. Kennon JC, Awad ME, Chutkan N, et al (2018) Current insights on use of growth factors as therapy for Intervertebral Disc Degeneration. Biomol Concepts 9:43–52. doi: 10.1515/bmc-2018-0003

67. Miyamoto K, An HS, Sah RL, et al (2005) Exposure to pulsed low intensity ultrasound stimulates extracellular matrix metabolism of bovine intervertebral disc cells cultured in alginate beads. SPINE 30:2398–2405. doi: 10.1097/01.brs.0000184558.44874.c0

68. Huang Y-C, Urban JPG, Luk KDK (2014) Intervertebral disc regeneration: do nutrients lead the way? Nature Publishing Group 10:561–566. doi: 10.1038/nrrheum.2014.91

69. Vasiliadis ES, Pneumaticos SG, Evangelopoulos DS, Papavassiliou AG (2014) Biologic treatment of mild and moderate intervertebral disc degeneration. Mol Med 20:400–409.

70. Masuda K, Imai Y, Okuma M, et al (2006) Osteogenic Protein-1 Injection Into a Degenerated Disc Induces the Restoration of Disc Height and Structural Changes in the Rabbit Anular Puncture Model. SPINE 31:

71. Gilbertson L, Ahn S-H, Teng P-N, et al (2008) The effects of recombinant human bone morphogenetic protein-2, recombinant human bone morphogenetic protein-12, and adenoviral bone morphogenetic protein-12 on matrix synthesis in human annulus fibrosis and nucleus pulposus cells. The Spine Journal 8:449–456. doi: 10.1016/j.spinee.2006.11.006

72. Chujo T, An HS, Akeda K, et al (2006) Effects of growth differentiation factor-5 on the intervertebral disc--in vitro bovine study and in vivo rabbit disc degeneration model study. SPINE 31:2909–2917. doi: 10.1097/01.brs.0000248428.22823.86

73. O'Connell GD, Malhotra NR, Vresilovic EJ, et al (2011) The effect of discectomy and the dependence on degeneration of human intervertebral disc strain in axial compression. ncbinlmnihgov 36:1765–1771. doi: 10.1097/BRS.0b013e318216752f

74.   Illing RO, Kennedy JE, Wu F, et al (2005) The safety and feasibility of extracorporeal high-intensity focused ultrasound (HIFU) for the treatment of liver and kidney tumours in a Western population. British Journal of Cancer 93:890–895.

75.   Zhu L, Altman MB, Laszlo A, et al (2019) Ultrasound Hyperthermia Technology for Radiosensitization. Ultrasound in Medicine & Biology 45:1025–1043.

76.   Mizrahi N, Zhou EH, Lenormand G, et al (2012) Low intensity ultrasound perturbs cytoskeleton dynamics. Soft Matter 8:2438–2443.

77.   Escoffre JM, Bouakaz A (2016) Therapeutic Ultrasound. doi: 10.1007/978-3-319-22536-4

78.   Kristiansen TK, Ryaby JP, McCabe J, et al (1997) Accelerated healing of distal radial fractures with the use of specific, low-intensity ultrasound - A multicenter, prospective, randomized, double-blind, placebo-controlled study. J Bone Joint Surg Am 79A:961–973.

79.   Hayton MJ, Dillon JP, Glynn D, et al (2005) Involvement of adenosine 5′-triphosphate in ultrasound-induced fracture repair. Ultrasound in Medicine & Biology 31:1131–1138. doi: 10.1016/j.ultrasmedbio.2005.04.017

80.   Erdogan Ö, Esen E (2009) Biological Aspects and Clinical Importance of Ultrasound Therapy in Bone Healing. J Ultrasound Med 28:765–776. doi: 10.7863/jum.2009.28.6.765

81.   Harrison A, Lin S, Pounder N, Mikuni-Takagaki Y (2016) Mode & mechanism of low intensity pulsed ultrasound (LIPUS) in fracture repair. Ultrasonics 70:45–52. doi: 10.1016/j.ultras.2016.03.016

82.   Naruse K, Sekiya H, Harada Y, et al (2010) Prolonged endochondral bone healing in senescence is shortened by low-intensity pulsed ultrasound in a manner dependent on COX-2. Ultrasound in Medicine & Biology 36:1098–1108. doi: 10.1016/j.ultrasmedbio.2010.04.011

83.   Katano M, Naruse K, Uchida K, et al (2011) Low Intensity Pulsed Ultrasound Accelerates Delayed Healing Process by Reducing the Time Required for the Completion of Endochondral Ossification in the Aged Mouse Femur Fracture Model. Exp Anim 60:385–395.

84.   Haar Ter G, Dyson M, Oakley EM (1987) The use of ultrasound by physiotherapists in Britain, 1985. Ultrasound in Medicine & Biology 13:659–663. doi: 10.1016/0301-5629(87)90064-0

85.   Iwashina T, Mochida J, Miyazaki T, et al (2006) Low-intensity pulsed ultrasound stimulates cell proliferation and proteoglycan production in rabbit intervertebral disc cells cultured in alginate. Biomaterials 27:354–361. doi: 10.1016/j.biomaterials.2005.06.031

86.   Enwemeka CS (1989) The Effects of Therapeutic Ultrasound on Tendon Healing: A Biomechanical Study. American Journal of Physical Medicine & Rehabilitation 68:283.

87.   Demir H, Menku P, Kirnap M, et al (2004) Comparison of the effects of laser, ultrasound, and combined laser + ultrasound treatments in experimental tendon healing. Lasers Surg Med 35:84–89. doi: 10.1002/lsm.20046

88.   Yeung CK, Guo X, Ng YF (2006) Pulsed ultrasound treatment accelerates the repair of Achilles tendon rupture in rats. J Orthop Res 24:193–201. doi: 10.1002/jor.20020

89.   Fu SC, Shum WT, Hung LK, et al (2008) Low-Intensity Pulsed Ultrasound on Tendon Healing: A Study of the Effect of Treatment Duration and Treatment Initiation. Am J Sports Med 36:1742–1749. doi: 10.1177/0363546508318193

90.   Lu H, Liu F, Chen H, et al (2016) The effect of low-intensity pulsed ultrasound on bone-tendon junction healing: Initiating after inflammation stage. J Orthop Res 34:1697–1706. doi: 10.1002/jor.23180

91.   Iwabuchi S, Ito M, Hata J, et al (2005) In vitro evaluation of low-intensity pulsed ultrasound in herniated disc resorption. Biomaterials 26:7104–7114. doi: 10.1016/j.biomaterials.2005.05.004

92.   Iwabuchi S, Ito M, Chikanishi T, et al (2008) Role of the tumor necrosis factor-α, cyclooxygenase-2, prostaglandin E2, and effect of low-intensity pulsed ultrasound in an in vitro herniated disc resorption model. J Orthop Res 26:1274–1278. doi: 10.1002/jor.20525

93.   Marvel S, Okrasinski S, Bernacki SH, et al (2010) The development and validation of a lipus system with preliminary observations of ultrasonic effects on human adult stem cells. IEEE Transactions on Ultrasonics, Ferroelectrics, and Frequency Control 57:1977–1984. doi: 10.1109/TUFFC.2010.1645

94.   Hensel K, Mienkina MP, Schmitz G (2011) Analysis of Ultrasound Fields in Cell Culture Wells for In Vitro Ultrasound Therapy Experiments. Ultrasound in Medicine & Biology 37:2105–2115. doi: 10.1016/j.ultrasmedbio.2011.09.007

95.   Padilla FDR, Puts R, Vico L, Raum K (2014) Stimulation of bone repair with ultrasound: A review of the possible mechanic effects. Ultrasonics 54:1125–1145. doi: 10.1016/j.ultras.2014.01.004

96.   Puts R, Ruschke K, Ambrosi TH (2016) A Focused Low-Intensity Pulsed Ultrasound (FLIPUS) System for Cell Stimulation: Physical and Biological Proof of Principle. IEEE Transactions on Ultrasonics, Ferroelectrics, and Frequency Control 63:91–100. doi: 10.1109/tuffc.2015.2498042

97.   Duan X, Yu ACH, Wan JMF (2019) Cellular Bioeffect Investigations on Low-Intensity Pulsed Ultrasound and Sonoporation: Platform Design and Flow Cytometry Protocol. IEEE Transactions on Ultrasonics, Ferroelectrics, and Frequency Control 66:1422–1434. doi: 10.1109/TUFFC.2019.2923443

98.   Leskinen JJ, Hynynen K (2012) Study of factors affecting the magnitude and nature of ultrasound exposure with in vitro set-ups. Ultrasound in Medicine & Biology 38:777–794. doi: 10.1016/j.ultrasmedbio.2012.01.019

99.   Berber R, Aziz S, Simkins J, et al (2020) Low Intensity Pulsed Ultrasound Therapy (LIPUS): A review of evidence and potential applications in diabetics. Journal of Clinical Orthopaedics and Trauma

100.   Schumann D, Kujat R, Zellner J, et al (2006) Treatment of human mesenchymal stem cells with pulsed low intensity ultrasound enhances the chondrogenic phenotype in vitro. Biorheology 43:431–443.

101.   Loi F, Córdova LA, Pajarinen J, et al (2016) Inflammation, fracture and bone repair. Bone 86:119–130. doi: 10.1016/j.bone.2016.02.020

102.   Kraiwattanapong C, Boden SD, Louis-Ugbo J, et al (2005) Comparison of Healos/Bone Marrow to INFUSE(rhBMP-2/ACS) With a Collagen-Ceramic Sponge Bulking Agent as Graft Substitutes for Lumbar Spine Fusion. SPINE 30:1001–1007. doi: 10.1097/01.brs.0000160997.91502.3b

103.   Erbe E, Marx J, Clineff T, Bellincampi L (2001) Potential of an ultraporous β-tricalcium phosphate synthetic cancellous bone void filler and bone marrow aspirate composite graft. Eur Spine J 10:S141–S146. doi: 10.1007/s005860100287

104.   Muschler GF, Nitto H, Matsukura Y, et al (2003) Spine fusion using cell matrix composites enriched in bone marrow-derived cells. Clinical Orthopaedics and Related Research® 407:102–118. doi: 10.1097/00003086-200302000-00018

105.   Li H, Zou X, Xue Q, et al (2004) Anterior lumbar interbody fusion with carbon fiber cage loaded with bioceramics and platelet-rich plasma. An experimental study on pigs. Eur Spine J 13:354–358. doi: 10.1007/s00586-003-0647-3

106.   Gupta A, Kukkar N, Sharif K, et al (2015) Bone graft substitutes for spine fusion: A brief review. World J Orthop 6:449–456. doi: 10.5312/wjo.v6.i6.449

107.   Cahill KS, Chi JH, Day A, Claus EB (2009) Prevalence, Complications, and Hospital Charges Associated With Use of Bone-Morphogenetic Proteins in Spinal Fusion Procedures. JAMA 302:58–66. doi: 10.1001/jama.2009.956

108.   Shi H-F, Xiong J, Chen Y-X, et al (2013) Early application of pulsed electromagnetic field in the treatment of postoperative delayed union of long-bone fractures: a prospective randomized controlled study. BMC Musculoskelet Disord 14:35. doi: 10.1186/1471-2474-14-35

109.   Garland DE, Moses B, Salyer W (1991) Long-term follow-up of fracture nonunions treated with PEMFs. Contemp Orthop 22:295–302.

110.   Mooney V (1993) Pulsed electromagnetic fields: an adjunct to interbody spinal fusion surgery in the high risk patient. Surg Technol Int 2:405–410.

111.   MS SLM, PhD DGC, PhD EIW, et al (2016) Pulsed electromagnetic field (PEMF) treatment reduces expression of genes associated with disc degeneration in human intervertebral disc cells. The Spine Journal 16:770–776. doi: 10.1016/j.spinee.2016.01.003

112.   Simmons JWJ, Mooney V, Thacker I (2004) Pseudarthrosis after lumbar spine fusion: nonoperative salvage with pulsed electromagnetic fields. Am J Orthop (Belle Mead NJ) 33:27–30.

113.   Singh RK, Srivastava M, Prasad NK, et al (2017) Iron doped Î²-Tricalcium phosphate: Synthesis, characterization, hyperthermia effect, biocompatibility and mechanical evaluation. Materials Science & Engineering C 78:715–726. doi: 10.1016/j.msec.2017.04.130

114.   Zhang X, Jiang F, Groth T, Vecchio KS (2008) Preparation, characterization and mechanical performance of dense β-TCP ceramics with/without magnesium substitution. J Mater Sci: Mater Med 19:3063–3070. doi: 10.1007/s10856-008-3442-1

115.   Cuneyt Tas A, Bhaduri SB, Jalota S (2007) Preparation of Zn-doped β-tricalcium phosphate (β-Ca3(PO4)2) bioceramics. Materials Science & Engineering C 27:394–401. doi: 10.1016/j.msec.2006.05.051

116.   Martin BI, Deyo RA, Mirza SK, et al (2008) Expenditures and Health Status Among Adults With Back and Neck Problems. JAMA 299:656–664. doi: 10.1001/jama.299.6.656

117.   Ricci JA, Stewart WF, Chee E, et al (2006) Back Pain Exacerbations and Lost Productive Time Costs in United States Workers. SPINE 31:3052–3060. doi: 10.1097/01.brs.0000249521.61813.aa

118.   Stewart WF (2003) Lost Productive Time and Cost Due to Common Pain Conditions in the US Workforce. JAMA 290:2443–2454. doi: 10.1001/jama.290.18.2443

119.   Risbud MV, Shapiro IM (2013) Role of cytokines in intervertebral disc degeneration: pain and disc content. Nat Rev Rheumatol 10:44–56. doi: 10.1038/nrrheum.2013.160

120.   Lerner A, Stein H, Soudry M (2004) Compound high-energy limb fractures with delayed union: our experience with adjuvant ultrasound stimulation (exogen). Ultrasonics 42:915–917. doi: 10.1016/j.ultras.2003.11.014

121.   Zhang XJ, Hu ZM, Hao J, Shen JL (2016) Low Intensity Pulsed Ultrasound Promotes the Extracellular Matrix Synthesis of Degenerative Human Nucleus Pulposus Cells Through FAK/PI3K/Akt Pathway. SPINE 41:E248–E254. doi: 10.1097/brs.0000000000001220

122.   Rousseau M, Ulrich JA, Bass EC, Rodriguez AG (2007) Stab incision for inducing intervertebral disc degeneration in the rat. SPINE 32:17–24. doi: 10.1097/01.brs.0000251013.07656.45

123.   Kobayashi Y, Sakai D, Iwashina T, et al (2009) Low-Intensity Pulsed Ultrasound Stimulates Cell Proliferation, Proteoglycan Synthesis and Expression of Growth Factor-Related Genes in Human Nucleus Pulposus Cell Line. European Cells and Materials 17:15–22. doi: 10.22203/eCM.v017a02

124. Hersh DS, Kim AJ, Winkles JA, et al (2016) Emerging Applications of Therapeutic Ultrasound in Neuro-oncology: Moving Beyond Tumor Ablation. Neurosurgery 79:643–654. doi: 10.1227/NEU.0000000000001399

125. Jiang X, Savchenko O, Li Y, et al (2018) A Review of Low-Intensity Pulsed Ultrasound for Therapeutic Applications. IEEE Transactions on Biomedical Engineering PP:1–1. doi: 10.1109/TBME.2018.2889669

126. Chen C, Zhang T, Liu F, et al (2019) Effect of Low-Intensity Pulsed Ultrasound After Autologous Adipose-Derived Stromal Cell Transplantation for Bone-Tendon Healing in a Rabbit Model. Am J Sports Med 47:942–953. doi: 10.1177/0363546518820324

127. Sheybani ND, Price RJ (2019) Perspectives on Recent Progress in Focused Ultrasound Immunotherapy. Theranostics 9:7749–7758. doi: 10.7150/thno.37131

128. Baker KG, Robertson VJ, Duck FA (2001) A review of therapeutic ultrasound: biophysical effects. Physical Therapy 81:1351–1358. doi: 10.1093/ptj/81.7.1351

129. Khanna A, Nelmes RTC, Gougoulias N, et al (2008) The effects of LIPUS on soft-tissue healing: a review of literature. British Medical Bulletin 89:169–182. doi: 10.1093/bmb/ldn040

130. Martinez de Albornoz P, Khanna A, Longo UG, et al (2011) The evidence of low-intensity pulsed ultrasound for in vitro, animal and human fracture healing. British Medical Bulletin 100:39–57. doi: 10.1093/bmb/ldr006

131. Xin Z, Lin G, Lei H, et al (2016) Clinical applications of low-intensity pulsed ultrasound and its potential role in urology. Transl Androl Urol 5:255–266. doi: 10.21037/tau.2016.02.04

132. Yang R-S, Lin W-L, Chen Y-Z, et al (2005) Regulation by ultrasound treatment on the integrin expression and differentiation of osteoblasts. Bone 36:276–283. doi: 10.1016/j.bone.2004.10.009

133. Bhandari M, Mundi R, Petis S, et al (2009) Low-intensity pulsed ultrasound: Fracture healing. Indian Journal of Orthopaedics 43:132. doi: 10.4103/0019-5413.50847

134. Pounder NM, Harrison AJ (2008) Low intensity pulsed ultrasound for fracture healing: A review of the clinical evidence and the associated biological mechanism of action. Ultrasonics 48:330–338. doi: 10.1016/j.ultras.2008.02.005

135. Cook SD, Salkeld SL, Popich-Patron LS, et al (2001) Improved cartilage repair after treatment with low-intensity pulsed ultrasound. Clinical Orthopaedics and Related Research® 391:S231–S243.

136. Lu H, Qin L, Cheung W, et al (2008) Low-Intensity Pulsed Ultrasound Accelerated Bone-Tendon Junction Healing Through Regulation of Vascular Endothelial Growth Factor Expression and Cartilage Formation. Ultrasound in Medicine & Biology 34:1248–1260. doi: 10.1016/j.ultrasmedbio.2008.01.009

137. Lu H, Qin L, Fok P, et al (2017) Low-Intensity Pulsed Ultrasound Accelerates Bone-Tendon Junction Healing: A Partial Patellectomy Model in Rabbits. Am J Sports Med 34:1287–1296. doi: 10.1177/0363546506286788

138. Qin L, Lu H, Fok P, et al (2006) Low-intensity pulsed ultrasound accelerates osteogenesis at bone-tendon healing junction. Elsevier 32:1905–1911. doi: 10.1016/j.ultrasmedbio.2006.06.028

139. Zhou X-Y, Xu X-M, Wu S-Y, et al (2017) Low-Intensity Pulsed Ultrasound-Induced Spinal Fusion is Coupled with Enhanced Calcitonin Gene-Related Peptide Expression in Rat Model. Ultrasound in Medicine & Biology 43:1486–1493. doi: 10.1016/j.ultrasmedbio.2017.03.012

140. Atherton P, Lausecker F, Harrison A, Ballestrem C (2017) Low-intensity pulsed ultrasound promotes cell motility through vinculin-controlled Rac1 GTPase activity. Journal of Cell Science 130:2277–2291. doi: 10.1242/jcs.192781

141. Xu X, Wang F, Yang Y, et al (2016) LIPUS promotes spinal fusion coupling proliferation of type H microvessels in bone. Sci Rep 6:1–10. doi: 10.1038/srep20116

142. Montalti CS, Souza NVCKL, Rodrigues NC, et al (2013) Effects of low-intensity pulsed ultrasound on injured skeletal muscle. Braz J Phys Ther 17:343–350. doi: 10.1590/S1413-35552012005000101

143. Hui CFF, Chan CW, Yeung HY, et al (2011) Low-Intensity Pulsed Ultrasound Enhances Posterior Spinal Fusion Implanted with Mesenchymal Stem Cells-Calcium Phosphate Composite Without Bone Grafting. SPINE 36:1010–1016. doi: 10.1097/BRS.0b013e318205c5f5

144. Zhou S, Schmelz A, Seufferlein T, et al (2004) Molecular mechanisms of low intensity pulsed ultrasound in human skin fibroblasts. J Biol Chem 279:54463–54469. doi: 10.1074/jbc.M404786200

145. Leskinen JJ, Olkku A, Mahonen A (2014) Nonuniform temperature rise in in vitro osteoblast ultrasound exposures with associated bioeffect. IEEE Transactions on Ultrasonics, Ferroelectrics, and Frequency Control 61:920–927. doi: 10.1109/tbme.2013.2292546

146. Fung C-H, Cheung W-H, Pounder NM, et al (2014) Osteocytes exposed to far field of therapeutic ultrasound promotes osteogenic cellular activities in pre-osteoblasts through soluble factors. Ultrasonics 54:1358–1365. doi: 10.1016/j.ultras.2014.02.003

147. Leskinen JJ, Karjalainen HM, Olkku A, et al (2008) Genome-wide microarray analysis of MG-63 osteoblastic cells exposed to ultrasound. Biorheology 45:345–354. doi: 10.3233/BIR-2008-0480

148. Kinoshita M, Hynynen K (2007) Key factors that affect sonoporation efficiency in in vitro settings: The importance of standing wave in sonoporation. Biochemical and Biophysical Research Communications 359:860–865. doi: 10.1016/j.bbrc.2007.05.153

149. OCHELTREE KB, FRIZZELL LA (1989) Sound Field Calculation for Rectangular Sources. IEEE Transactions on Ultrasonics, Ferroelectrics, and Frequency Control 36:242–248. doi: 10.1109/58.19157

150. Adams MS, Salgaonkar VA, Scott SJ, et al (2017) Integration of deployable fluid lenses and reflectors with endoluminal therapeutic ultrasound applicators: Preliminary investigations of enhanced penetration depth and focal gain. Med Phys 44:5339–5356. doi: 10.1002/mp.12458

151. Ophir J, McWhirt RE, Maklad NF, Jaeger PM (1985) A narrowband pulse-echo technique for in vivo ultrasonic attenuation estimation. IEEE Trans Biomed Eng 32:205–212. doi: 10.1109/TBME.1985.325530

152. Parvizi J, Wu CC, Lewallen DG, et al (1999) Low-intensity ultrasound stimulates proteoglycan synthesis in rat chondrocytes by increasing aggrecan gene expression. J Orthop Res 17:488–494. doi: 10.1002/jor.1100170405

153.   Tang X, Coughlin D, Ballatori A, et al (2019) Pulsed Electromagnetic Fields Reduce Interleukin-6 Expression in Intervertebral Disc Cells Via Nuclear Factor-κβ and Mitogen-Activated Protein Kinase p38 Pathways. SPINE 44:E1290–E1297. doi: 10.1097/BRS.0000000000003136

154.   Subramanian A, Budhiraja G, Sahu N (2017) Chondrocyte primary cilium is mechanosensitive and responds to low-intensity-ultrasound by altering its length and orientation. The International Journal of Biochemistry & Cell Biology 91:1–5. doi: 10.1016/j.biocel.2017.08.018

155.   Lee H-P, Gu L, Mooney DJ, et al (2017) Mechanical confinement regulates cartilage matrix formation by chondrocytes. Nat Mater 16:1243–1251. doi: 10.1038/nmat4993

156.   Bohari SP, Grover LM, Hukins DW (2012) Pulsed-low intensity ultrasound enhances extracellular matrix production by fibroblasts encapsulated in alginate. Journal of Tissue Engineering 3:204173141245467–7. doi: 10.1177/2041731412454672

157.   Ouyang A, Cerchiari AE, Tang X, et al (2016) Effects of cell type and configuration on anabolic and catabolic activity in 3D co-culture of mesenchymal stem cells and nucleus pulposus cells. J Orthop Res 1–13. doi: 10.1002/jor.23452

158.   Wang Z, Hutton WC, Yoon ST (2013) ISSLS Prize winner: Effect of link protein peptide on human intervertebral disc cells. SPINE 38:1501–1507. doi: 10.1097/BRS.0b013e31828976c1

159.   Masuda K, Takegami K, An H, et al (2003) Recombinant osteogenic protein-1 upregulates extracellular matrix metabolism by rabbit annulus fibrosus and nucleus pulposus cells cultured in alginate beads. J Orthop Res 21:922–930. doi: 10.1016/S0736-0266(03)00037-8

160. Thonar E, An H, Masuda K (2002) Compartmentalization of the matrix formed by nucleus pulposus and annulus fibrosus cells in alginate gel. Biochem Soc Trans 30:874–878.

161. Augst AD, Kong HJ, Mooney DJ (2006) Alginate hydrogels as biomaterials. Macromol Biosci 6:623–633. doi: 10.1002/mabi.200600069

162. Enobakhare BO, Bader DL, Lee DA (1996) Quantification of sulfated glycosaminoglycans in chondrocyte/alginate cultures, by use of 1,9-dimethylmethylene blue. Anal Biochem 243:189–191. doi: 10.1006/abio.1996.0502

163. la Cour MF, Stuart MB, Laursen MB, et al (2014) Investigation of PDMS as coating on CMUTs for imaging. In: 2014 IEEE International Ultrasonics Symposium. IEEE, pp 2584–2587

164. Karshafian R, Bevan PD, Williams R, et al (2009) Sonoporation by Ultrasound-Activated Microbubble Contrast Agents: Effect of Acoustic Exposure Parameters on Cell Membrane Permeability and Cell Viability. Ultrasound in Medicine & Biology 35:847–860. doi: 10.1016/j.ultrasmedbio.2008.10.013

165. Han SI, Oh SY, Jeon WJ, et al (2002) Mild heat shock induces cyclin D1 synthesis through multiple Ras signal pathways. FEBS Letters 515:141–145. doi: 10.1016/S0014-5793(02)02459-6

166. Sena K, Leven RM, Mazhar K, et al (2005) Early gene response to low-intensity pulsed ultrasound in rat osteoblastic cells. Ultrasound in Medicine & Biology 31:703–708. doi: 10.1016/j.ultrasmedbio.2005.01.013

167. Kim J-S, Ellman MB, An HS, et al (2010) Insulin-like growth factor 1 synergizes with bone morphogenetic protein 7-mediated anabolism in bovine intervertebral disc cells. Arthritis & Rheumatism 62:3706–3715. doi: 10.1002/art.27733

168. Edwards WT, Ordway NR, Zheng Y, et al (2001) Peak stresses observed in the posterior lateral anulus. SPINE 26:1753–1759. doi: 10.1097/00007632-200108150-00005

169. Jiang X, Savchenko O, Li Y, et al (2019) A Review of Low-Intensity Pulsed Ultrasound for Therapeutic ApplicationsA Review of Low-Intensity Pulsed Ultrasound for Therapeutic Applications. IEEE Transactions on Biomedical Engineering 66:2704–2718. doi: 10.1109/TBME.2018.2889669

170. Horne DA, Jones PD, Adams MS, et al (2020) LIPUS far-field exposimetry system for uniform stimulation of tissues in-vitro: development and validation with bovine intervertebral disc cells. Biomed Phys Eng Express 6:035033–13. doi: 10.1088/2057-1976/ab8b26

171. Zhang N, Chow SK-H, Leung KS, Cheung W-H (2017) Ultrasound as a stimulus for musculoskeletal disorders. Journal of Orthopaedic Translation 9:52–59. doi: 10.1016/j.jot.2017.03.004

172. Sittampalam GS, Grossman A, Brimacombe K, et al (2004) GTPγS Binding Assays.

173. Ray CA, Patel V, Shih J, et al (2009) Application of multi-factorial design of experiments to successfully optimize immunoassays for robust measurements of therapeutic proteins. Journal of Pharmaceutical and Biomedical Analysis 49:311–318. doi: 10.1016/j.jpba.2008.11.039

174.   Uhoraningoga A, Kinsella G, Henehan G, Ryan B (2018) The Goldilocks Approach: A Review of Employing Design of Experiments in Prokaryotic Recombinant Protein Production. Bioengineering 5:89–27. doi: 10.3390/bioengineering5040089

175.   Blakney AK, McKay PF, Yus BI, et al (2019) The Skin You Are In: Design-of-Experiments Optimization of Lipid Nanoparticle Self- Amplifying RNA Formulations in Human Skin Explants. ACS Nano 13:5920–5930. doi: 10.1021/acsnano.9b01774

176.   Pfaffl MW (2001) A new mathematical model for relative quantification in real-time RT-PCR. Nucleic Acids Res 29:e45–45. doi: 10.1093/nar/29.9.e45

177.   Derringer G, Suich R (1980) Simultaneous Optimization of Several Response Variables. Journal of Quality Technology 12:214–219. doi: 10.1080/00224065.1980.11980968

178.   Miller AD, Chama A, Louw TM, et al (2017) Frequency sensitive mechanism in low-intensity ultrasound enhanced bioeffects. PLoS ONE 12:e0181717. doi: 10.1371/journal.pone.0181717

179.   Lewis AH, Cui AF, McDonald MF, Grandl J (2017) Transduction of Repetitive Mechanical Stimuli by Piezo1 and Piezo2 Ion Channels. Cell Rep 19:2572–2585. doi: 10.1016/j.celrep.2017.05.079

180.   Ding W, Du D, Chen S (2020) LIPUS promotes synthesis and secretion of extracellular matrix and reduces cell apoptosis in human osteoarthritis through upregulation of SOX9 expression. Int J Clin Exp Pathol 13:810–817.

181.   Miller AD, Subramanian A, Viljoen HJ (2017) Theoretically proposed optimal frequency for ultrasound induced cartilage restoration. Theor Biol Med Model 14:1–14. doi: 10.1186/s12976-017-0067-4

182.   Angle SR, Sena K, Sumner DR, Virdi AS (2011) Osteogenic differentiation of rat bone marrow stromal cells by various intensities of low-intensity pulsed ultrasound. Ultrasonics 51:281–288. doi: 10.1016/j.ultras.2010.09.004

183.   Sekino J, Nagao M, Kato S, et al (2018) Low-intensity pulsed ultrasound induces cartilage matrix synthesis and reduced MMP13 expression in chondrocytes. Biochemical and Biophysical Research Communications 506:290–297. doi: 10.1016/j.bbrc.2018.10.063

184.   Kim K, Fisher JP (2008) Nanoparticle technology in bone tissue engineering. Journal of Drug Targeting 15:241–252. doi: 10.1080/10611860701289818

185.   Ortolani A, Bianchi M, Mosca M, et al (2016) The prospective opportunities offered by magnetic scaffolds for bone tissue engineering: a review. Joints 4:228–235. doi: 10.11138/jts/2016.4.4.228

186.   Uskoković V, Wu V (2016) Calcium Phosphate as a Key Material for Socially Responsible Tissue Engineering. Materials 9:434–27. doi: 10.3390/ma9060434

187.   Waldorff EI, Zhang N, Ryaby JT (2017) Pulsed electromagnetic field applications: A corporate perspective. Journal of Orthopaedic Translation 9:60–68. doi: 10.1016/j.jot.2017.02.006

188.   Dimitriou R, Jones E, McGonagle D, Giannoudis PV (2011) Bone regeneration: current concepts and future directions. BMC Med 9:66–10. doi: 10.1186/1741-7015-9-66

189.   Meng J, Xiao B, Zhang Y, et al (2013) Super-paramagnetic responsive nanofibrous scaffolds under static magnetic field enhance osteogenesis for bone repair in vivo. Sci Rep 3:393–7. doi: 10.1038/srep02655

190.   Russo A, Bianchi M, Sartori M, et al (2016) Magnetic forces and magnetized biomaterials provide dynamic flux information during bone regeneration. J Mater Sci: Mater Med 27:175–13. doi: 10.1007/s10856-015-5659-0

191.   Gil S, Mano JF (2014) Magnetic composite biomaterials for tissue engineering. Biomater Sci 2:812–818. doi: 10.1039/C4BM00041B

192.   Pesqueira T, Costa-Almeida R, Gomes ME (2017) Uncovering the effect of low-frequency static magnetic field on tendon-derived cells: from mechanosensing to tenogenesis. Sci Rep 7:1–12. doi: 10.1038/s41598-017-11253-6

193.   Mondal S, Manivasagan P, Bharathiraja S, et al (2017) Magnetic hydroxyapatite: a promising multifunctional platform for nanomedicine application. IJN Volume 12:8389–8410. doi: 10.2147/IJN.S147355

194.   Pareta RA, Taylor E, Webster TJ (2008) Increased osteoblast density in the presence of novel calcium phosphate coated magnetic nanoparticles. Nanotechnology 19:265101–8. doi: 10.1088/0957-4484/19/26/265101

195.   Zeng X, Zeng X, Hu, et al (2012) Magnetic responsive hydroxyapatite composite scaffolds construction for bone defect reparation. IJN 3365–14. doi: 10.2147/IJN.S32264

196.   Panseri S, Cunha C, D'Alessandro T, et al (2012) Intrinsically superparamagnetic Fe-hydroxyapatite nanoparticles positively influence osteoblast-like cell behaviour. Journal of Nanobiotechnology 10:32–10. doi: 10.1186/1477-3155-10-32

197.   Tampieri A, D'Alessandro T, Sandri M, et al (2012) Intrinsic magnetism and hyperthermia in bioactive Fe-doped hydroxyapatite. Acta Biomaterialia 8:843–851. doi: 10.1016/j.actbio.2011.09.032

198.   Zhao Z, Espanol M, Guillem-Marti J, et al (2016) Ion-doping as a strategy to modulate hydroxyapatite nanoparticle internalization. Nanoscale 8:1595–1607. doi: 10.1039/C5NR05262A

199.   Panseri S, Cunha C, D'Alessandro T, et al (2012) Magnetic Hydroxyapatite Bone Substitutes to Enhance Tissue Regeneration: Evaluation In Vitro Using Osteoblast-Like Cells and In Vivo in a Bone Defect. PLoS ONE 7:e38710–8. doi: 10.1371/journal.pone.0038710

200.   Singh RK, Patel KD, Lee JH, et al (2014) Potential of Magnetic Nanofiber Scaffolds with Mechanical and Biological Properties Applicable for Bone Regeneration. PLoS ONE 9:e91584–16. doi: 10.1371/journal.pone.0091584

201.   Gregory CA, Grady Gunn W, Peister A, Prockop DJ (2004) An Alizarin red-based assay of mineralization by adherent cells in culture: comparison with cetylpyridinium chloride extraction. Anal Biochem 329:77–84. doi: 10.1016/j.ab.2004.02.002

202.   Livak KJ, Schmittgen TD (2001) Analysis of relative gene expression data using real-time quantitative PCR and the 2(-Delta Delta C(T)) Method. Methods 25:402–408. doi: 10.1006/meth.2001.1262

203.   Birmingham E, Niebur GL, McHugh PE, et al (2012) Osteogenic differentiation of mesenchymal stem cells is regulated by osteocyte and osteoblast cells in a simplified bone niche. European Cells and Materials 23:13–27. doi: 10.22203/ecm.v023a02

204.   Kramer E, Conklin M, Zilm M (2016) A Comparative Study of the Sintering and Cell Behavior of Pure and Cobalt Substituted Hydroxyapatite. Bioceram Dev Appl 04:1–8. doi: 10.4172/2090-5025.1000077

205.   Zilm ME, Le Yu, Hines WA, Wei M (2018) Magnetic properties and cytocompatibility of transition-metal-incorporated hydroxyapatite. Materials Science & Engineering C 87:112–119. doi: 10.1016/j.msec.2018.02.018

206.   Rau JV, Cacciotti I, De Bonis A, et al (2014) Fe-doped hydroxyapatite coatings for orthopedic and dental implant applications. Applied Surface Science 307:301–305. doi: 10.1016/j.apsusc.2014.04.030

207.   Veiseh O, Gunn JW, Zhang M (2010) Design and fabrication of magnetic nanoparticles for targeted drug delivery and imaging. Advanced Drug Delivery Reviews 62:284–304. doi: 10.1016/j.addr.2009.11.002

208.   Wu S, Xiao Z, Song J, et al (2018) Evaluation of BMP-2 Enhances the Osteoblast Differentiation of Human Amnion Mesenchymal Stem Cells Seeded on Nano-Hydroxyapatite/Collagen/Poly(l-Lactide). IJMS 19:2171–16. doi: 10.3390/ijms19082171

209.   Neacsu P, Staras A, Voicu S, et al (2017) Characterization and In Vitro and In Vivo Assessment of a Novel Cellulose Acetate-Coated Mg-Based Alloy for Orthopedic Applications. Materials 10:686–20. doi: 10.3390/ma10070686

210.   Blair HC, Larrouture QC, Li Y, et al (2017) Osteoblast Differentiation and Bone Matrix Formation In Vivo and In Vitro. Tissue Engineering Part B: Reviews 23:268–280. doi: 10.1089/ten.TEB.2016.0454

211.   Selvamurugan N, Kwok S, Vasilov A, et al (2007) Effects of BMP-2 and pulsed electromagnetic field (PEMF) on rat primary osteoblastic cell proliferation and gene expression. J Orthop Res 25:1213–1220. doi: 10.1002/jor.20409

212.   Calabrese G, Giuffrida R, Fabbi C, et al (2016) Collagen-Hydroxyapatite Scaffolds Induce Human Adipose Derived Stem Cells Osteogenic Differentiation In Vitro. PLoS ONE 11:e0151181–17. doi: 10.1371/journal.pone.0151181

213.   Fan L, Zhang Y, Li X, et al (2012) Removal of alizarin red from water environment using magnetic chitosan with Alizarin Red as imprinted molecules. Colloids Surf B Biointerfaces 91:250–257. doi: 10.1016/j.colsurfb.2011.11.014

214.   Singh K, Nandyala SV, Marquez-Lara A, et al (2013) Clinical sequelae after rhBMP-2 use in a minimally invasive transforaminal lumbar interbody fusion. The Spine Journal 13:1118–1125. doi: 10.1016/j.spinee.2013.07.028

Appendix A: Annulus Fibrosus Cell Viability Time Course in Alginate Bead Culture

Introduction

Cell viability time course experiments were performed to evaluate potential cell death during multi-day annulus fibrosus (AF) cell culture. The objectives of this study were (1) to assess the viability of cells encapsulated in alginate beads at high cell concentration and (2) to determine the limit of cell culture duration (i.e. when cell numbers were significantly decreased).

Methods

Cell Culture

Bovine AF cells were encapsulated in alginate beads at a density of $4\text{x}10^6$ cells/mL and cultured in standard disc media as described previously (Section 3.2.2.1). Four alginate beads (one sample) were cultured for 1, 3, 5, 8, 10, 14, or 16 days in triplicate (n = 21). Media was changed every other day.

DNA Quantification

After the designated culture duration, alginate beads were dissolved in 55 mM sodium citrate and frozen at -20°C. After day 16 samples were harvested, samples were thawed and digested in 10 µL papain (P3125, Sigma-Aldrich, St. Louis, MO, USA) at 60°C overnight, then frozen at -20°C again before DNA quantification assay. DNA content was assayed with the Quant-iT PicoGreen dsDNA Assay Kit (P11496, Thermo Fisher, Waltham, MA, USA) and measured on a microplate reader (Spectramax M5, Molecular Devices, Sunnyvale, CA, USA) with 488 nm excitation and 525 nm absorption.

Statistical Analysis

Statistical differences in DNA concentration were compared using one-way analysis of variance (ANOVA) among treatment groups, followed by Tukey HSD test for multiple

comparisons. Data are depicted as mean ± standard deviation. *P*-values less than 0.05 were considered significant.

Results and Discussion

DNA concentration did not significantly decrease until 8 days of culture. Compared to samples cultured for 1 day, DNA concentration in day 8, day 14, and day 16 samples was decreased by 28%, 32%, and 38%, respectively. After 8 days of culture, the decrease in DNA concentration appears to reach a baseline. These results suggest that in future studies of cellular stimuli, such as low-intensity pulsed ultrasound (LIPUS) exposure or growth factor treatment, cells cultured in alginate beads should undergo a longer pre-culture duration to allow cells to acclimate to alginate environment. This aligns with several other groups studying LIPUS bioeffects who have reported applying pre-cultures from 3-14 days [1-3]. In this experiment, change in dsDNA concentration was used to approximate cell number and extrapolated to estimate changes in cell viability. We assume that DNA from dead cells will degrade and not be detected by PicoGreen Assay, however it is possible that we have quantified dead cells before DNA fragmentation and therefore have overestimated the cell numbers. It may take several days for DNA to fully degrade, which may explain why DNA concentration doesn't approach equilibrium until day 8.
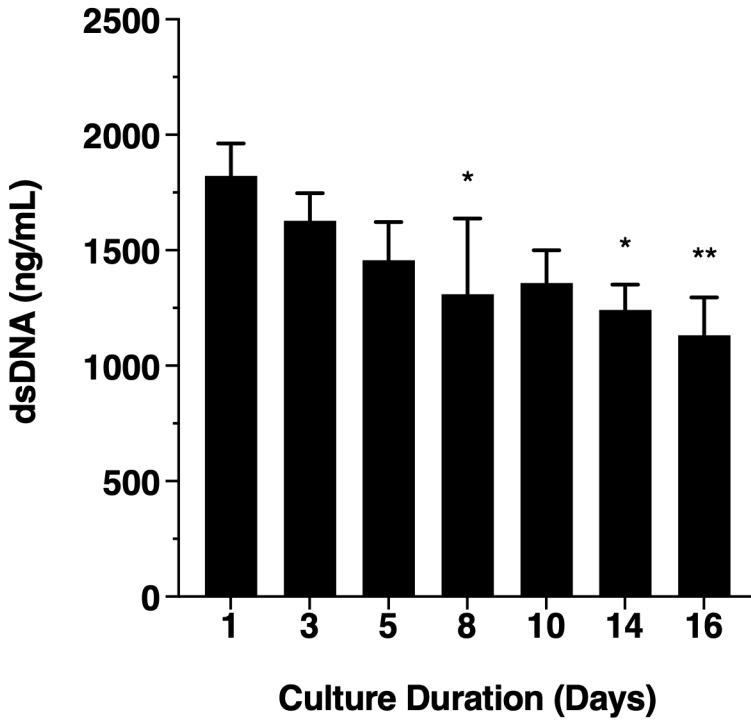
Figure A.1 DNA concentration decreases with duration of culture in alginate beads
Double stranded DNA concentration was significantly lower after 8, 14, and 16 days of culture compared to 1 day of culture. * $p < 0.05$, ** $p < 0.01$

References

1. Parvizi J, Wu CC, Lewallen DG, et al (1999) Low-intensity ultrasound stimulates proteoglycan synthesis in rat chondrocytes by increasing aggrecan gene expression. J Orthop Res 17:488–494. doi: 10.1002/jor.1100170405

2. Kobayashi Y, Sakai D, Iwashina T, et al (2009) Low-Intensity Pulsed Ultrasound Stimulates Cell Proliferation, Proteoglycan Synthesis and Expression of Growth Factor-Related Genes in Human Nucleus Pulposus Cell Line. European Cells and Materials 17:15–22. doi: 10.22203/eCM.v017a02

3. Sekino J, Nagao M, Kato S, et al (2018) Low-intensity pulsed ultrasound induces cartilage matrix synthesis and reduced MMP13 expression in chondrocytes. Biochemical and Biophysical Research Communications 506:290–297. doi: 10.1016/j.bbrc.2018.10.063

Appendix B: LIVE/DEAD Cell Imaging in Alginate Beads

Introduction

Experiments were performed to assess the effect of low-intensity pulsed ultrasound (LIPUS) exposure on the viability of annulus fibrosus (AF) cells cultured in alginate beads. Moreover, these experiments aimed to develop an effective method for imaging whole sections of stained beads. This would allow visualization of local variations in cell viability potentially related to diffusion limitations [1]. Specifically, we were interested in whether dead cells were disproportionately located in the center of the bead.

Methods

Cell Culture and Treatment

Bovine AF cells were encapsulated in alginate beads at a density of $2x10^6$ cells/mL and cultured in standard disc media, as described previously (Section 3.2.2.1), with daily media changes. Single beads were divided into 4 treatment groups: (1) untreated control, (2) BMP-7 growth factor treatment (200 ng/mL in standard disc media), (3) LIPUS-Low (600 mW peak Intensity, 20% duty), and (4) LIPUS-High (1000 mW peak intensity, 12% duty). All groups were placed in the LIPUS exposimetry system for 20 minutes per day for 7 consecutive days. LIPUS was turned off for samples in the untreated control and BMP-7 treatment groups.

Protocol for LIVE/DEAD Cell Staining and Imaging in Alginate Beads

Sample Preparation

- Place bead into 1.5 mL tube

- Wash 3x with 1 mL D-PBS without calcium or magnesium

- Place a glass microscope slide inside a petri dish

- Carefully remove bead from 1.5 mL tube and onto the glass slide **(Figure B.1)**

- Using a sharp scalpel blade, cut the bead in half (approximately 1.5 mm thickness)

  - Take care to create surfaces that are as flat as possible

- Position bead sections on the glass slide such that a flat surface is facing up
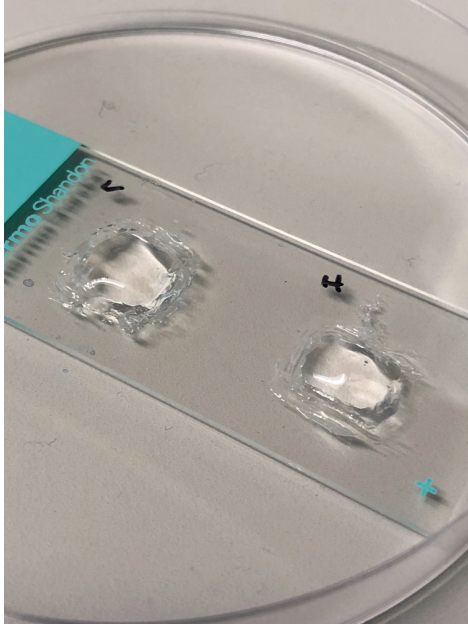
Figure B.1 Positioning sectioned alginate beads
The sectioned alginate beads were placed on the glass slide with the flat surface facing up. Petroleum jelly was placed on the glass slide to create a square chamber to confine the bead and liquid reagent. LIVE/DEAD reagent was applied, filling the chamber and covering the bead-section. L indicates the LIPUS-Low sample; H indicates the LIPUS-High sample.
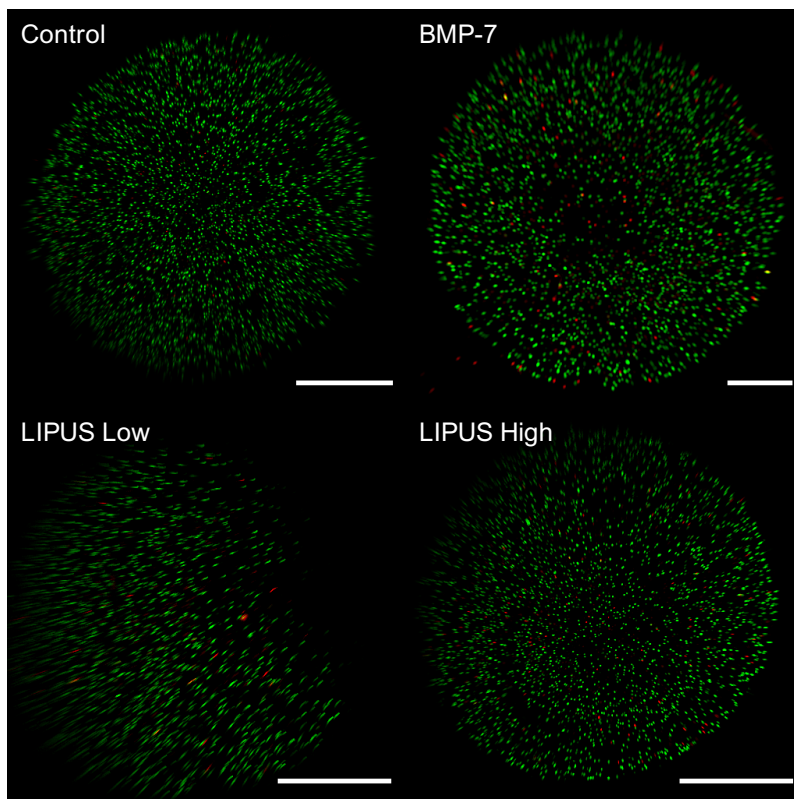
LIVE/DEAD Staining

- Prepare LIVE/DEAD reagent solution in 15 mL tube

  - 2 mL D-PBS + 2 µL Calcein-AM + 8 µL ethidium homodimer-1

- Cover the bead sections with LIVE/DEAD reagent solution (approximately 100 µL)

- Incubate for 20 minutes at 37°C

Imaging

- Imaging was performed using a Nikon AZ100M "Macro Confocal" with a 5x objective and Z stack range of 500 µm.

Results and Discussion

The purpose of this experiment was to assess the effect of LIPUS exposure on cell viability when varying peak intensity, with total energy held constant by adjusting the duty factor. LIVE/DEAD imaging visually demonstrated that the majority of cells were live (green) with dead cells evenly disbursed throughout the samples (red) **(Figure B.2)**. The ability to image across the whole sample allows the identification of regional differences. In this experiment, there were no apparent regional differences in cell viability. These staining and imaging methods can be expanded in the future for use in immunostaining for extracellular matrix proteins or pro-inflammatory factors and give insight into whether LIPUS induced effects vary with distance from the surface of the alginate bead.

Figure B.2 Effect of LIPUS exposure on cell viability in alginate beads
Cell viability assessed by LIVE/DEAD stain demonstrates no apparent reduction in cell viability with 7 days of growth factor or LIPUS treatment compared to nontreated controls. Green: live, Red: dead. Scale bars = 1 mm.

References

1. Dolor A, Sampson SL, Lazar AA, et al (2019) Matrix modification for enhancing the transport properties of the human cartilage endplate to improve disc nutrition. PLoS ONE 14:e0215218–18. doi: 10.1371/journal.pone.0215218

Appendix C: LIPUS upregulates sGAG but not Collagen Content in Annulus Fibrosus Cells

    Cultured in Hyaluronic Acid Beads

Introduction

LIPUS-induced cellular deformation and response are thought to be dependent on the mechanical properties of the surrounding medium [1]. Moreover, cells feel and respond to the stiffness of their substrate [2]. To investigate the effect of scaffold stiffness on LIPUS-induced extracellular matrix (ECM) synthesis in annulus fibrosus (AF) cells, we identified a hyaluronic acid (HyA) hydrogel with tunable stiffness and containing an Arg-Gly-Asp (AGD) amino acid sequence for cell adhesion [3]. The aims of this proof-of-concept study were: (1) to develop a method for forming HyA hydrogels with a bead geometry, and (2) evaluate changes in collagen and sulfated glycosaminoglycan (sGAG) content in AF cells cultured in HyA beads with LIPUS exposure.

Methods

Hydrogel Formation

Bovine AF cells were encapsulated in HyA gels at a density of $4\text{x}10^6$ cells/mL as described previously [3] with the following adaptations. AF-cells were suspended in the HyA macromer solution (acHyA and bsp-RGD/acHyA), then this HyA-cell solution was mixed with an MMP-cleavable crosslinker [3]. Immediately following their mixture, the solution was dispensed dropwise through a 22-gauge needle onto a glass slide coated with a hydrophobic material (12-50, Tekdon, Inc., Myakka City, FL, USA) and then incubated for 45 minutes at 37°C to allow gelation to occur. After gelation, standard disc media (Section 3.2.2.1) was added and exchanged every other day.

LIPUS Exposure

HyA beads were divided into 3 groups and treated as described previously (Section 3.2.2.2) with the following adaptations. Each sample (9 HyA beads) was cultured for 10 total days and treated for 5 consecutive days starting on the 6th day of culture.

**Quantification of Collagen and sGAG Concentration**

After 10 days of culture, HyA beads were dissolved by adding 100 U/mL hyaluronidase (H3631-15KU, Sigma) and incubating on a rocker at 37°C for 6 hours. Supernatants were collected and assayed of total collagen, sGAG, and dsDNA content as described previously (Sections 3.2.2.3 and 3.2.2.4). Collagen and sGAG concentrations were determined by normalizing total collagen and sGAG content by the dsDNA concentration of each sample.

Statistical Analysis

Statistical differences in collagen and sGAG concentrations were compared using one-way analysis of variance (ANOVA) among treatment groups, followed by Tukey HSD test for multiple comparisons. Data are depicted as mean ± standard deviation. *P*-values less than 0.05 were considered significant.

Results and Discussion

HyA beads were successfully formed by dispensing the HyA solution through a needle onto a slide with a hydrophobic coating **(Figure C.1)**. These beads resemble the alginate beads used in previous studies (Chapter 3) in shape and size.
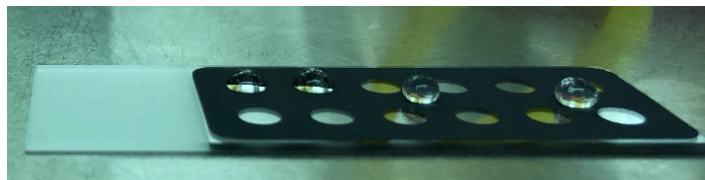
Figure C.1 Hyaluronic acid beads after gelation on glass slide with hydrophobic coating
Beads with high contact angles were formed by dispensing the HyA-cell solution onto coated microscope slides.

While neither BMP-7 nor LIPUS treatment affected collagen synthesis when cells were cultured in HyA beads, sGAG concentration was significantly greater than controls with both BMP-7 (2.3-fold) and LIPUS (3.8-fold) treatment, with LIPUS significantly outperforming BMP-7 treatment **(Figure C.2).** The opposite matrix synthesis effect was observed in AF-cells cultured in alginate beads (Chapter 3), indicating that cellular scaffold material properties may be an important factor affecting cell response to LIPUS stimulus, suggesting that tissue properties may be important considerations in future *in-vivo* application. Future work will evaluate the effect of varying scaffold stiffness on AF-cell matrix synthesis response.
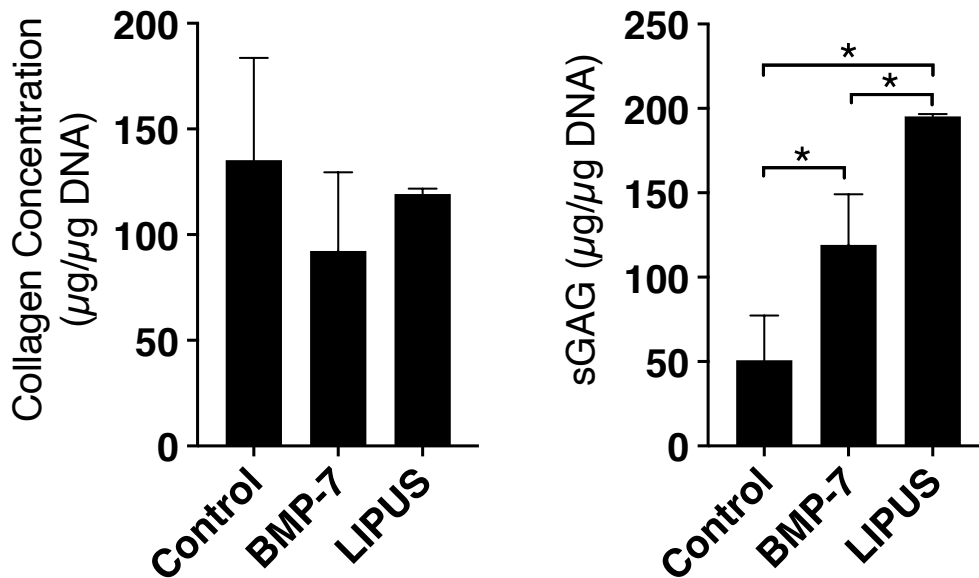
Figure C.2 LIPUS-induced matrix synthesis in hyaluronic acid beads
Collagen concentration was not affected by BMP-7 nor LIPUS treatment. Both BMP-7 and LIPUS treatment groups demonstrated significantly greater sGAG concentration compared to the control group, with LIPUS significantly outperforming BMP-7. * $p < 0.05$

References

1. Miller AD, Chama A, Louw TM, et al (2017) Frequency sensitive mechanism in low-intensity ultrasound enhanced bioeffects. PLoS ONE 12:e0181717. doi: 10.1371/journal.pone.0181717

2. Discher DE, Janmey P, Wang Y-L (2005) Tissue cells feel and respond to the stiffness of their substrate. Science 310:1139–1143. doi: 10.1126/science.1116995

3. Jha AK, Tharp KM, Browne S, et al (2016) Matrix metalloproteinase-13 mediated degradation of hyaluronic acid-based matrices orchestrates stem cell engraftment through vascular integration. Biomaterials 89:136–147. doi: 10.1016/j.biomaterials.2016.02.023

Appendix D: Effects of LIPUS Pulse Repetition Frequency on Matrix Gene Expression in AF cells Cultured in Alginate Beads

Introduction

Preliminary experiments were performed to demonstrate the technical feasibility of evaluating the effects of *in-vitro* LIPUS exposure on gene expression using qPCR. Specifically, we aimed to explore the effects of LIPUS pulse repletion frequency (PRF) and number of treatments on extracellular matrix gene expression in AF cells cultured in alginate beads. A secondary aim was to determine whether cells were responsive to BMP-7 treatment by evaluating ID-1 gene expression [1], to validate its use as a positive control.

Methods

Cell Culture and Treatment

Bovine AF cells were encapsulated in alginate beads at a density of $4x10^6$ cells/mL and cultured in standard disc media, as described previously (Section 3.2.2.1), with daily media changes. Samples of up to 10 beads were divided into 12 treatment groups with 4 replicates each (n = 48) **(Table D.1)**. Samples were cultured for up to 4 total days, including 1 day of pre-culture to allow cells to acclimate to alginate-bead culture. All groups were placed in the LIPUS exposimetry system for 20 minutes per day for 3 consecutive days. LIPUS was turned off for samples in the untreated control and BMP-7 treatment groups.

Table D.1 Sample grouping in preliminary LIPUS PRF study
Samples were divided into 12 treatment groups including LIPUS High, LIPUS Low, BMP-7, and Control repeated for 1, 2, or 3 treatments.

Treatment	PRF (Hz)	Burst Count	Peak Intensity (mW)
LIPUS High	1000	300	600
LIPUS Low	100	3000	600
BMP-7 (200 ng/mL)	-	-	-
Control	-	-	-

Gene Expression Analysis

Twenty-four hours following the last treatment, alginate beads were dissolved in 55 mM sodium citrate, and cell pellets were isolated by centrifugation. AF cells were lysed using PicoPure RNA extraction buffer, according to manufacturer's instructions, and stored at -80°C until all samples were collected. Total RNA was isolated and purified, cDNA was synthesized, and qPCR was performed as described previously (Section 4.2.4).

Statistical Analysis

Statistical differences in relative gene expression among treatment groups were compared using one-way analysis of variance (ANOVA), followed by Tukey HSD test for multiple comparisons. Data are depicted as mean ± standard deviation. *P*-values less than 0.05 were considered significant.

Results and Discussion

When cells were exposed to a LIPUS waveform at 100Hz PRF for 20 minutes a day for 3 consecutive days, MMP1 – a gene which encodes proteases involved in the breakdown of extracellular matrix proteins including collagens type I and II – expression was significantly downregulated compared to nontreated controls (0.71-fold decrease) and was significantly reduced compared to identical LIPUS exposure at 1000 Hz PRF. Additionally, we observed significant increases in COL1A1, COL2A1, TIMP1, and MMP1 expression with 3 LIPUS High treatments compared to the same amount of LIPUS low treatments. During this preliminary study, we found that the expression of various matrix-related genes was dependent on PRF, a LIPUS waveform parameter. Overall, we found that several matrix-related genes were regulated by LIPUS PRF including COL1A1, COL2A1, TIMP1, and MMP1.

Our results do not align with previous studies demonstrating that BMP-7 growth factor treatment stimulates matrix synthesis in intervertebral disc cells [2-4]. Moreover, BMP-7 did not upregulate ID1, which mediates many of the downstream effects of BMP signaling [1]. This suggests that BMP signaling is being inhibited.

In this study, we confirmed the ability to use qPCR to evaluate changes in matrix gene expression in response to LIPUS exposure and found that PRF was a significant factor for modulating matrix gene expression. We also found that BMP-7 does not regulate matrix gene expression in AF cells cultured in alginate and does not upregulate ID1 signaling.
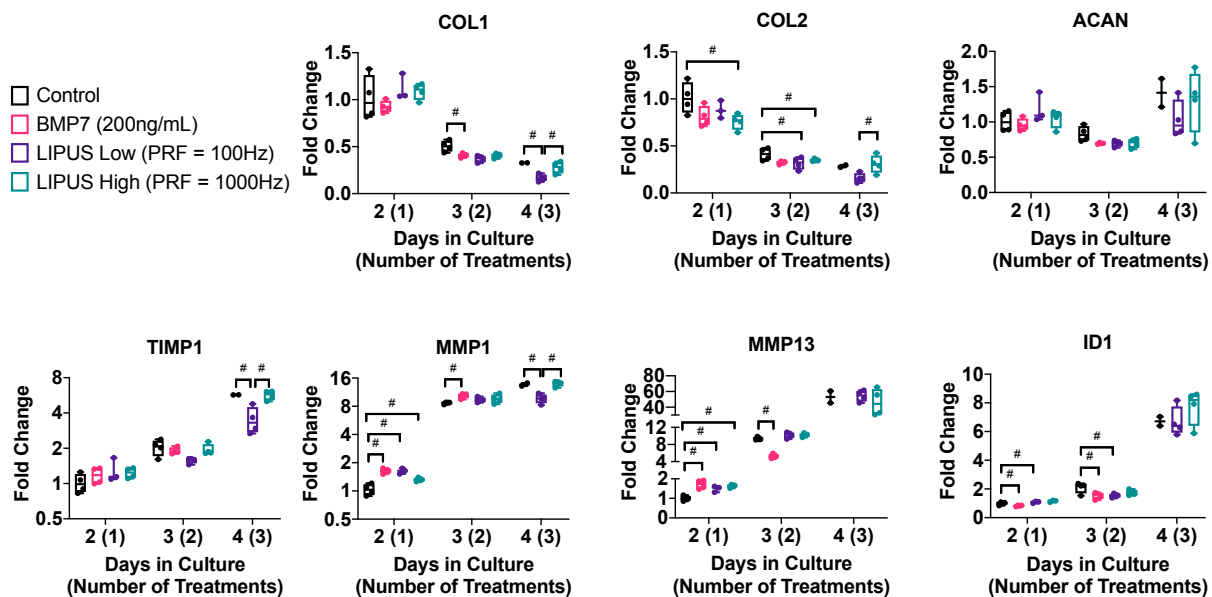
Figure D.1 Relative gene expression for select genes relevant to matrix metabolism
Relative gene expression was calculated as fold-change relative to control expression in samples cultured for 2 days. n = 4 per group. # $p < 0.05$

References

1. Brazil DP, Church RH, Surae S, et al (2015) BMP signalling: agony and antagony in the family. Trends in Cell Biology 25:249–264.

2. Masuda K, Takegami K, An H, et al (2003) Recombinant osteogenic protein-1 upregulates extracellular matrix metabolism by rabbit annulus fibrosus and nucleus pulposus cells cultured in alginate beads. J Orthop Res 21:922–930. doi: 10.1016/S0736-0266(03)00037-8

3. Masuda K, Imai Y, Okuma M, et al (2006) Osteogenic Protein-1 Injection Into a Degenerated Disc Induces the Restoration of Disc Height and Structural Changes in the Rabbit Anular Puncture Model. SPINE 31:

4. Imai Y, Okuma M, An HS, et al (2007) Restoration of Disc Height Loss by Recombinant Human Osteogenic Protein-1 Injection Into Intervertebral Discs Undergoing Degeneration Induced by an Intradiscal Injection of Chondroitinase ABC. SPINE 32:1197–1205. doi: 10.1097/BRS.0b013e3180574d26

Appendix E: BMP-7 Upregulates Type I Collagen Gene Expression in Annulus Fibrosus Cells Cultured in Monolayer

Introduction

Preliminary experiments were performed to establish BMP-7 growth factor as a positive control for stimulating extracellular matrix (ECM) metabolism in annulus fibrosus (AF) cells. Although BMP-7 is known to stimulate ECM metabolism in intervertebral disc cells [1], this was not observed in previous studies of AF cells cultured in alginate beads (Appendix D). This could be related to insufficient diffusion of BMP-7-supplemented media into the alginate matrix [2]. The objective of this study was to evaluate whether BMP-7 upregulates matrix synthesis in AF cells cultured in monolayer and whether there is a dose-response relationship with ID1, a mediator of downstream effects of BMP signaling, and type I collagen.

Methods

Cell Culture and Treatment

Bovine AF cells were seeded in monolayer at 2×10^5 cells/well in a 24-well cell culture plate. Samples were divided into groups including 1, 2, or 3 treatments with BMP-7 at 0, 50, 100, or 200 ng/mL. All samples were cultured for 4 total days, including 1 day for acclimation before initial treatment, and treated for 1, 2, or 3 of those days. To determine whether BMP-7 has an effect with a short culture duration, two additional treatment groups included a single BMP-7 treatment (200 ng/mL) and harvesting after one day.

Gene Expression Analysis

After 4 days of culture, samples were processed for qPCR, and gene expression was analyzed as described previously (Section 4.2.4), including the analysis of ID1 and type I collagen gene

expression. Relative expression was calculated as fold-change relative to the respective untreated control group for the groups cultured for 4 days and 1 day.

Statistical Analysis

Statistical differences in relative gene expression among treatment groups were compared using one-way analysis of variance (ANOVA), followed by Tukey HSD test for multiple comparisons. Data are depicted as mean ± standard deviation. *P*-values less than 0.05 were considered significant.

Results and Discussion

BMP-7 treatment upregulated ID1 expression in all groups compared to the untreated control **(Figure E.1)**. Notably, this effect was demonstrated with the lowest dose: 1 treatment at 50 ng/mL. ID1 expression appeared to have a positive correlation with BMP-7 concentration, indicating a dose-response relationship. BMP-7 also upregulated type I collagen expression; however, with a weaker positive correlation. Again, 50 ng/mL BMP-7 appears to be sufficient for stimulating matrix metabolism, with a 2.9-fold increase in type 1 collagen expression compared to the control.
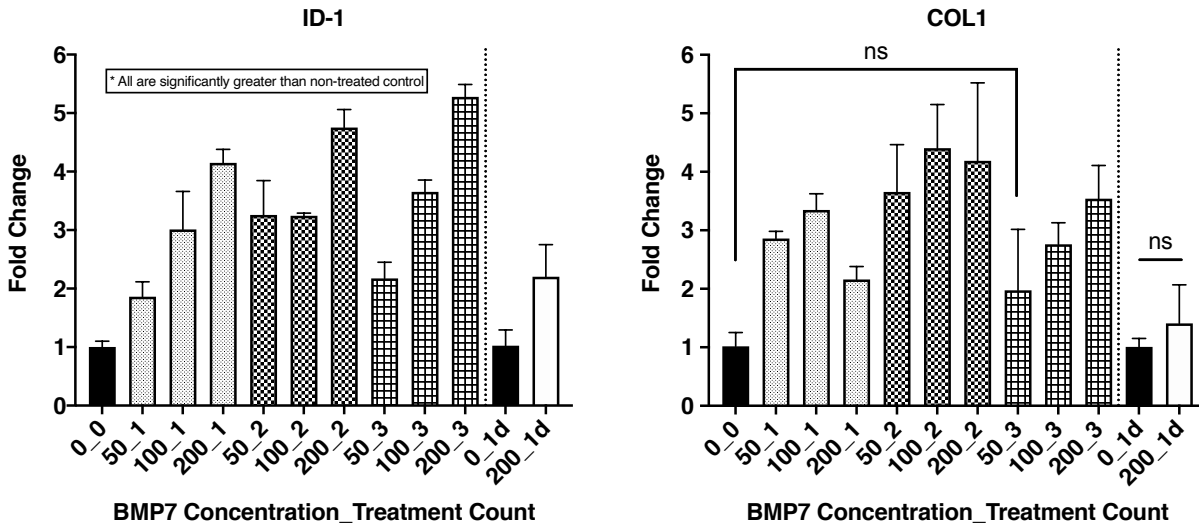
Figure E.1 BMP-7 stimulates ID1 and COL1 gene expression in AF cell monolayers
All BMP-7 treatment conditions demonstrated significantly upregulated ID1 and type I collagen
gene expression ($p < 0.05$) except where indicated (ns).

Overall, these results indicate that AF cells cultured in monolayer are stimulated by BMP-7

treatment to upregulate matrix anabolism. Results also demonstrate a dose-response relationship

between BMP-7 and expression of ID1 and type I collagen, suggesting that there may be an optimal

dose. Previous experiments have utilized a dose of 200 ng/mL BMP-7 (Chapter 3, Appendix C

and D); however, these results also indicate that a lower dose (1 treatment at 50 ng/mL) may be

sufficient for stimulating type I collagen gene expression.

References

1. Masuda K, Takegami K, An H, et al (2003) Recombinant osteogenic protein-1 upregulates extracellular matrix metabolism by rabbit annulus fibrosus and nucleus pulposus cells cultured in alginate beads. J Orthop Res 21:922–930. doi: 10.1016/S0736-0266(03)00037-8

2. Dolor A, Sampson SL, Lazar AA, et al (2019) Matrix modification for enhancing the transport properties of the human cartilage endplate to improve disc nutrition. PLoS ONE 14:e0215218–18. doi: 10.1371/journal.pone.0215218

3. Brazil DP, Church RH, Surae S, et al (2015) BMP signalling: agony and antagony in the family. Trends in Cell Biology 25:249–264.

Appendix F: Preliminary Study of LIPUS Effects on Annulus Fibrosus Cells Cultured in Inflammatory Media

Introduction

LIPUS has been shown to stimulate matrix metabolism in degenerative intervertebral disc (IVD) cells [1], and IL-1α is known to induce an inflammatory response in IVD cells [2]. The objective of this study was to investigate the effects of LIPUS exposure on AF-cell gene expression in a simulated pro-inflammatory *in-vitro* environment.

Methods

Cell Culture and Treatment

Bovine AF cells were seeded in monolayer at 5×10^5 cells/well in the center of two opposing corner wells of 6-well cell culture plates and cultured in standard disc media, as described previously (Section 3.2.2.1), with daily media changes. Samples were divided into 6 treatment groups to be treated 1, 3, or 5 times with 50 ng/mL BMP-7, 10 ng/mL IL-1a, or 20 min of LIPUS (with parameters described in Section 3.2.2.2) individually or in combination **(Table F.1)**. IL-1α treatment occurred at least two hours before LIPUS exposure or BMP-7 to stimulate an inflammatory environment. All groups were placed in the LIPUS exposimetry system for 20 minutes per day for 1, 3, or 5 consecutive days. LIPUS was turned off for samples in the untreated control, IL-1α, and BMP-7 treatment groups.

Table F.1 Parameters for BMP-7, Il-1α, and LIPUS treatment
Samples were treated with the with BMP-7, Il-1α, or LIPUS individually or in combination.

Description	Treatment Parameters
Control	No Treatment
BMP-7	50 ng/mL BMP-7
IL-1α	10 ng/mL IL-1α
IL-1α + BMP-7	10 ng/mL IL-1α + 50 ng/mL BMP-7
IL-1α + LIPUS	10 ng/mL IL-1α + 20 min LIPUS
LIPUS	20 min LIPUS

Gene Expression Analysis

After 1, 3, or 5 days of culture, samples were processed for qPCR, and matrix and inflammatory gene expression was analyzed as described previously (Section 4.2.4). Relative expression was calculated as fold-change relative to the untreated control group on day 1.

Statistical Analysis

Statistical differences in relative gene expression among treatment groups were compared using one-way analysis of variance (ANOVA), followed by Tukey HSD test for multiple comparisons. Data are depicted as mean ± standard deviation. *P*-values less than 0.05 were considered significant.

Results and Discussion

Samples treated 1, 3, or 5 times with IL-1α demonstrated significantly increased MMP1, MMP13, and IL6 gene expression compared to the untreated control. IL-1α treatment had no effect on COL1 expression. One BMP-7 treatment significantly reduced expression of MMP1 and MMP13, but not IL6 in inflammatory cells. Three BMP-7 treatments reduced, but not significantly, MMP1 and MMP13 expression in inflammatory cells. Five BMP-7 treatments reduced, but not significantly, MMP1 and MMP13 expression while increasing, but not significantly, COL1 expression in inflammatory cells. One LIPUS treatment reduced, but not significantly, MMP1, MMP13, and IL6 expression in inflammatory cells. Three LIPUS treatments did not affect MMP1, MMP13, or IL6 expression but demonstrated an insignificant increase in COL1 expression in inflammatory cells. Five LIPUS treatments reduced, but not significantly, MMP1, MMP13, and IL6 expression while increasing, but not significantly, COL1 expression in inflammatory cells.

Overall, we demonstrate that IL-1α treatment consistently induces catabolic and pro-inflammatory gene expression in AF cells, but does not significantly affect type I collagen gene

158

expression. LIPUS appears to have an anti-catabolic effect on inflammatory AF cells that is most prominent with one treatment. Although there were not significant differences with LIPUS treatment in normal or pro-inflammatory conditions, there were trends that are promising and motivate dose optimization.
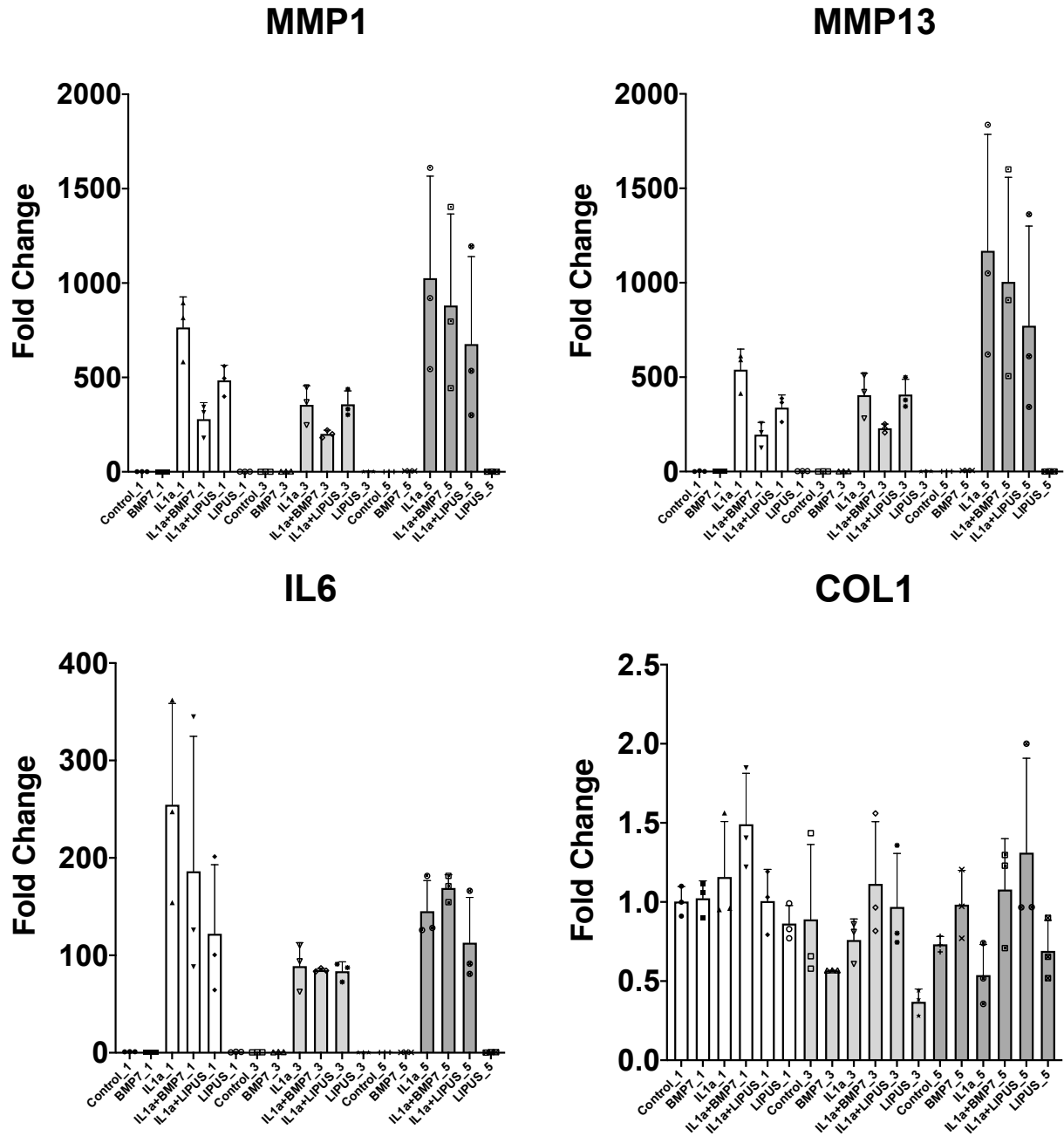
Figure F.1 Relative gene expression for select genes relevant to matrix metabolism Relative gene expression was calculated as fold-change relative the control sample of the in 1-treatment group. n = 3 per group.

References

1. Chen M-H, Sun J-S, Liao S-Y, et al (2015) Low-intensity pulsed ultrasound stimulates matrix metabolism of human annulus fibrosus cells mediated by transforming growth factor β1 and extracellular signal-regulated kinase pathway. Connective Tissue Research 56:219–227. doi: 10.3109/03008207.2015.1016609

2. Miller SL, Coughlin DG, Waldorff EI, et al (2016) Pulsed electromagnetic field (PEMF) treatment reduces expression of genes associated with disc degeneration in human intervertebral disc cells. Spine J 16:770–776. doi: 10.1016/j.spinee.2016.01.003

Appendix G: Additional Contributions

This appendix includes the abstract of a manuscript that did not directly relate to my dissertation for which I was a co-author and contributed intellectually. My specific contributions are described below.

A Mouse Model of Delayed Rotator Cuff Repair Results in Persistent Muscle Atrophy and Fatty Infiltration

Zili Wang, Xuhui Liu, Michael R. Davies, Devante Horne, Hubert Kim, Brian Feeley

Abstract

Background: Rotator cuff (RC) tears are common tendon injuries seen in orthopaedic patients. Successful repair of large and massive RC tears remains a challenge due to our limited understanding of the pathophysiological features of this injury. Clinically relevant small animal models that can be used to study the pathophysiological response to repair are limited by the lack of chronic repair models.

Purpose: To develop a highly clinically relevant mouse model of delayed RC repair.

Study Design: Controlled laboratory study.

Methods: Three-month-old C57BL/6J mice underwent unilateral supraspinatus (SS) and infraspinatus (IS) tendon tear with immediate, 2-week delayed, or 6-week delayed tendon repair. Animals with no repair or sham surgery served as controls. Gait analysis was conducted to measure shoulder function at 2 weeks and 6 weeks after surgery. Animals were sacrificed 6 weeks after the

last surgery. Shoulder joint, SS, and IS muscles were harvested and analyzed histologically. Ex vivo mechanical testing of intact and repaired SS and IS tendons was conducted. Reverse-transcriptase polymerase chain reaction was performed on SS and IS muscles to quantify atrophy, fibrosis, and fatty infiltration–related gene expression.

Results: Histological and tendon mechanical testing showed that torn tendons could be successfully repaired as late as 6 weeks after transection. However, significant atrophy and fatty infiltration of muscle, with impaired shoulder function, were persistent in the 6-week delayed repair group. Shoulder function correlated with the severity of RC muscle weight loss and fatty infiltration.

Conclusion: We successfully developed a clinically relevant mouse model of delayed RC repair. Six-week delayed RC repair resulted in persistent muscle atrophy and fatty infiltration with inferior shoulder function compared with acute repair.

Clinical Relevance: Our novel mouse model could serve as a powerful tool to understand the pathophysiological and cellular/ molecular mechanisms of RC muscle and tendon degeneration, eventually improving our strategies for treating and repairing RC tears.

My contributions to this study included the design of custom fixtures for biomechanical testing, development of mechanical testing protocol, conducting all biomechanical tests, helping with data analysis for mechanical tests, and writing a portion of the manuscript.

Publishing Agreement

It is the policy of the University to encourage open access and broad distribution of all theses, dissertations, and manuscripts. The Graduate Division will facilitate the distribution of UCSF theses, dissertations, and manuscripts to the UCSF Library for open access and distribution. UCSF will make such theses, dissertations, and manuscripts accessible to the public and will take reasonable steps to preserve these works in perpetuity.

I hereby grant the non-exclusive, perpetual right to The Regents of the University of California to reproduce, publicly display, distribute, preserve, and publish copies of my thesis, dissertation, or manuscript in any form or media, now existing or later derived, including access online for teaching, research, and public service purposes.

DocuSigned by:

_____   5/27/2020
F472E86288F3440...   Author Signature   _____
                                                                               Date